PATRYK KRZYSTECZKO

MEMRISTIVE TUNNEL JUNCTIONS

BIELEFELD UNIVERSITY

Memristive Tunnel Junctions

Thesis by Patryk Krzysteczko

BIELEFELD UNIVERSITY
DEPARTMENT OF PHYSICS

Thesis to obtain the academic degree of doctor rerum naturalium

Referees:
PD Andy Thomas
Prof. Jürgen Schnack

Declaration:
I hereby declare that the work in this thesis is my own original work, except where indicated in the text.

The chapter *The Memristor* is based on the paper: P. Krzysteczko, G. Reiss, and A. Thomas, 'Memristive switching of MgO based magnetic tunnel junctions,' Appl. Phys. Lett. **95**, 112508 (2009)

In the chapter *Resistive switching* the section *Positive stress* is based on the paper: P. Krzysteczko, X. Kou, K. Rott, A. Thomas, and G. Reiss, 'Current induced resistance change of magnetic tunnel junctions with ultra-thin MgO tunnel barriers,' J. Magn. Magn. Mater. **321**, 144 (2009)

August 2010

Acknowledgments

I would like to express my gratitude to my supervisors PD Andy Thomas and Prof. Günter Reiss for giving me the opportunity to work in their research groups and their excellent advice throughout this study. Particularly, I would like to thank PD Andy Thomas who encouraged me on the way to this 'exotic' topic.

My sincere thanks to Dr. Karsten Rott who was the first to observe 'anomalies' that led to the discovery of memristive magnetic tunnel junctions, and to Dr. Xinli Kou for her support at the early stage of this project.

I am grateful for the maintenance of all the machines in our laboratory, especially to Dr. Karsten Rott, Daniel Ebke, Oliver Schebaum, and Markus Schäfers.

Special thanks to Dr. Camelia Albon for sharing the e-beam expertise as well as the proof-reading of the manuscript.

To all colleagues on d2 I am appreciative for the pleasant work environment, especially to Zoë Kugler, Markus Schäfers, Volker Drewello, and Oliver Schebaum.

I also benefited from the outstanding quality of the samples provided by Berthold Ocker, Dr. Jürgen Langer, and Dr. Wolfram Maass from Singulus Inc.

The fruitful collaboration with Dr. Vladislav Demidov and Prof. Sergej Demokritov is highly acknowledged.

Contents

List of publications

First-author publications

1. P. Krzysteczko, X. Kou, K. Rott, A. Thomas, and G. Reiss, 'Current induced resistance change of magnetic tunnel junctions with ultra-thin MgO tunnel barriers,' J. Magn. Magn. Mater. **321**, 144 (2009).

2. P. Krzysteczko, G. Reiss, and A. Thomas, 'Memristive switching of MgO based magnetic tunnel junctions,' Appl. Phys. Lett. **95**, 112508 (2009).[1]

[1] Also selected for the Virtual Journal of Nanoscale Science & Technology

Coauthor publications

3. V. E. Demidov, S. O. Demokritov, K. Rott, P. Krzysteczko, and G. Reiss, 'Self-focusing of spin waves in permalloy microstripes,' Appl. Phys. Lett. **91**, 252504 (2007)

4. V. E. Demidov, S. O. Demokritov, K. Rott, P. Krzysteczko, and G. Reiss, 'Linear and nonlinear spin-wave dynamics in macro- and microscopic magnetic confined structures,' J. Phys. D: Appl. Phys., **41**, 164012 (2008)

5. V. E. Demidov, S. O. Demokritov, K. Rott, P. Krzysteczko, and G. Reiss, 'Nano-optics with spin waves at microwave frequencies,' Appl. Phys. Lett. **92**, 232503 (2008)[2]

[2] Also selected for the Virtual Journal of Nanoscale Science & Technology

6. V. E. Demidov, S. O. Demokritov, K. Rott, P. Krzysteczko, and G. Reiss, 'Mode interference and periodic self-focusing of spin waves in permalloy microstripes' Phys. Rev B **77**, 064406 (2008)

7. V. E. Demidov, M. P. Kostylev, K. Rott, P. Krzysteczko, G. Reiss, and S. O. Demokritov, 'Excitation of microwaveguide modes by a stripe antenna,' Appl. Phys. Lett. **95**, 112509 (2009)

[3] Also selected for the Virtual Journal of Nanoscale Science & Technology

8. V. E. Demidov, J. Jersch, K. Rott, P. Krzysteczko, G. Reiss, and S. O. Demokritov, 'Nonlinear propagation of spin waves in microscopic magnetic stripes,' Phys. Rev. Lett. **102**, 177207 (2009)[3]

9. V. E. Demidov, J. Jersch, S. O. Demokritov, K. Rott, P. Krzysteczko, and G. Reiss, 'Transformation of propagating spin-wave modes in microscopic waveguides with variable width,' Phys. Rev. B **79**, 054417 (2009)

[4] Also selected for the Virtual Journal of Nanoscale Science & Technology

10. V. E. Demidov, M. Buchmeier, K. Rott, P. Krzysteczko, J. Münchenberger, G. Reiss, and S. O. Demokritov, 'Nonlinear hybridization of the fundamental eigenmodes of microscopic ferromagnetic ellipses,' Phys. Rev. Lett. **104**, 217203 (2010)[4]

Conferences

Dreikönigstreffen Magnetismus *New concepts in spin dynamics* 2008 Bad Honnef, Germany, 'Self-focusing of spin waves in permalloy micro-stripes' (poster)

Final colloquium SPP 1133 *Ultrafast magnetization processes* 2008 Irsee, Germany, 'Current induced diffusion in magnetic tunnel junctions with ultra-thin tunnel barriers' (poster)

DPG Früjahrstagung 2008 Berlin, Germany, 'Current induced diffusion in magnetic tunnel junctions with ultra-thin MgO tunnel barriers' (poster)

DPG Früjahrstagung 2009 Dresden, Germany, 'Current induced resistance change of magnetic tunnel junctions' (oral)

MMM 2009, Austin, TX, USA 'Current induced resistance change of magnetic tunnel junctions' (oral)

Joint MMM & Intermag 2010, Washington, D.C., USA 'Memristive switching of MgO based magnetic tunnel junctions' (oral)

Preface

Every invention consists of a new combination of old elements. Probably you will comment on this statement differently, depending on whether your approach is more philosophical or that of a patent attorney. However, physics was always about a combination of two or more research fields (today we call it interdisciplinarity). Kepler's laws of planetary motion, for instance, were the result of a combination of careful observation of Mars (astronomy) and knowledge of conic sections (mathematics). Today mathematics became an inherent part of physics. But there are still invisible walls between different disciplines, sometimes even within specific fields such as solid state physics.

During the discussion of the present thesis, the focus will move from spintronics to nanoionics and will finally enter the domain of (artificial) neural networks. Based on measurements on magnetic tunnel junctions, we will reveal how promising applications and analytical methods emerge from the interplay of those scientific fields.

The thesis is divided in three chapters arranged according to the scheme: *first example - general model - second example*. Each chapter is again composed of three sections, organized according to the more classic order: *introduction - experimental results - discussion*. In the first chapter, the title of the thesis is elucidated. Following our recent publication,[5] we reveal that magnetic tunnel junctions fit in the recently emerged field of memristors and memristive systems. We describe how this 'hot topic' emerged from the combination of two research fields and take a step further by including magnetic systems. The somewhat illustrative data presented in this chapter has been chosen to demonstrate the most striking features of memristive magnetic tunnel junctions. Not only the smooth switching between two well defined resistive states is presented, but also—and this is the novelty introduced by magnetic electrodes—additional states due to spin-dependent

[5] P. Krzysteczko et al., Appl. Phys. Lett. **95**, 112508 (2009)

tunneling. At the end of the first chapter, the limits of the applicability of the memristor theory are discussed.

In the second chapter, the resistive switching is identified as the physical mechanism responsible for the memristivity of magnetic tunnel junctions. First, the main models and theories proposed in the literature are summarized. The data presented thereafter has been chosen to give a complete phenomenological picture of the memristivity of magnetic tunnel junctions. Some of these results were already published elsewhere.[6] Based on this experimental evidence, a model is developed particularly suited to describe the physical mechanisms responsible for the memristivity of magnetic tunnel junctions.

[6] P. Krzysteczko et al., J. Magn. Magn. Mater. **321**, 144 (2009)

The third chapter deals with neural networks and synapses in particular. In the beginning, a brief introduction to biological neural networks is given. The experimental results needed for a comparison of memristive magnetic tunnel junctions with biological synapses are provided in the middle part of this chapter. Finally, the astonishing equivalency of both systems is revealed by a discussion of the measurements on memristive magnetic tunnel junctions and by comparison with recent results from the neuroscientific literature.

Abstract of the thesis

In this section, a comprehensive outline of the present work is given. The structure of the outline is identical with the structure of the thesis. Occasionally, comments on the scientific relevance of the topic are included.

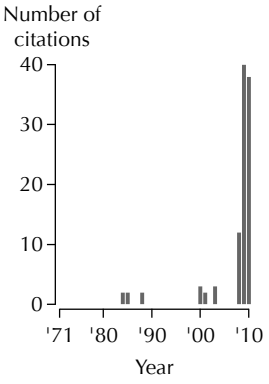

Figure 1: Citation of the pioneering paper 'Memristor—The Missing Circuit Element' by Leon O. Chua. Data provided by the Institute for Scientific Information, 7/28/10.

The Memristor

A brief history of the memristor The memristor was postulated, from an axiomatic point of view, by Leon Chua in 1971. From the symmetry of the equations associated with the basic circuit elements, he concluded that one circuit element was missing.[7] This element, named memristor, would connect the magnetic flux ϕ with the charge q in the same way as the resistor connects the voltage v with the current i. It would further exhibit an adjustable internal state.

[7] L. Chua, IEEE Trans. Circuit Theory **18**, 507 (1971)

The voltage across a (charge controlled) memristor is given by $v = R(q)i$. The internal state of the memristor is determined by the charge q, thus, the element 'remembers' the history of the applied current i since its resistivity depends on $q = \int i(t)\mathrm{d}t$.

The memristor can be understood as a potentiometer-like device which is self-driven according to the current flowing through it. Positive currents increase the resistance, for instance, and negative currents decrease it. Without current flow the latest resistance value is stored.

This idea of a 'pure' memristor was extended to a more general concept in 1976. For an nth order memristive system,[8] the internal state of the device is described by a set of n variables $\vec{w} = (w_1, w_2, \ldots, w_n)$ and the voltage across the memristive device is given by $v = R(\vec{w})i$.

[8] L. Chua et al., IEEE Proc. **64**, 209 (1976)

For more than thirty years the memristor remained elusive (see fig. 1), until Stanley Williams and fellow Hewlett-Packard researchers published their seminal paper with the dramatic title 'The missing memristor found!' The memristor was reborn by the connection of the ideas developed by Chua with the well-established field of resistive switching.[9]

[9] D. B. Strukov et al., Nature **453**, 80 (2008)

Memristive behavior of MTJs According to the ITRS, the limits of traditional memory technologies are almost reached. Concepts based on resistance change rather than charge storage, particularly the resistive RAM and the magnetic RAM, are extensively investigated as candidates for new nonvolatile memory devices.[10] We take the next step and combine both effects in one device—the memristive MTJ.

MTJ
Magnetic tunnel junction

ITRS
International technology roadmap for semiconductors

RAM
Random access memory

[10] G. I. Meijer, Science **319**, 1625 (2008)

The characteristics of memristive MTJs arise from the combination of a metal-insulator-metal system exhibiting resistive switching with the TMR effect. The first one can be driven by the voltage via electric field and the second one by the current via spin transfer torque. Or in the language of the memristor theory: $R = R(\vec{w}, t)$, where $w_1(v)$ describes the voltage driven distribution of mobile ions within the insulator and $w_2(j) \in \{\text{P}, \text{AP}\}$ gives the magnetic configuration. In this framework, we present studies on MgO-based magnetic tunnel junctions with Co-Fe-B electrodes. The samples are characterized by TMR ratios of about 100 % and an additional bipolar resistive switching of up to 12 %.

TMR
Tunnel Magnetoresistance

P
Parallel

AP
Anti-parallel

The discussion of experimental data starts with a typical i-v-curve showing the so-called pinched hysteresis—the main indication of memristive behavior—and the splitting into the P and the AP magnetic state. Then, a specific measurement procedure is introduced, developed to unmask the memristive behavior disguised by the nonlinearity associated with the tunneling process. Finally, the main characteristics of memristive MTJs are discussed

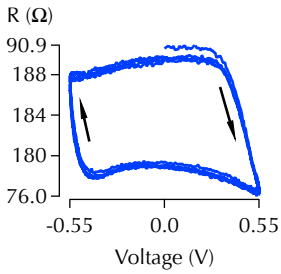

Figure 2: The resistance of a memristive MTJ (measured at 20 mV) as a function of the stress voltage. Multiple voltage sweeps are plotted on top of each other to indicate reproducibility.

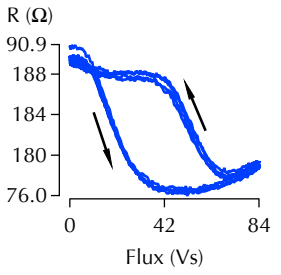

Figure 3: The same data as in fig. 2 displayed as a function of flux (stress voltage integrated over time).

based on two instructive methods to display memristive data. The bipolar resistive switching between two stable resistance states is displayed most clearly when the resistance is plotted vs. voltage (see fig. 2). One can observe how the resistance change is induced when the applied voltage exceeds a certain threshold. A bias of opposite polarity switches the resistance back to the initial state. The memristive nature of this switching process is shown with clarity when the resistance is plotted vs. flux (see fig. 3). A stable $R(\phi)$ hysteresis curve comes into view in this case.

How the presented system differs from a pure memristor The topic of this chapter is a critical view on the $R(\phi)$-curves. Surprisingly few $R(\phi)$-curves were discussed in the literature, despite the high popularity of the memristor. We begin with the case which is closest to a pure memristor and provide a phenomenological $R(\phi)$-function. Subsequently, some more complex cases are presented and the according deviations from the pure memristor are discussed.

Resistive switching

General models The concept of a memristor is not connected to any particular realization of a device. Yet, a great body of literature is dedicated to memristors based on resistive switching. In resistive RAM, electrochemical processes within the insulator layer are responsible for the resistance change. Particularly, the movement of oxygen vacancies in the applied electric field is believed to play the dominant role in the modulation of the conducting state of these devices. In this section, we give an overview of the mechanisms proposed as the origin of the resistive switching.

The phenomenology of resistive MTJs Here, the characteristic features of memristive MTJs are presented in a phenomenological manner. At the beginning, the experimental methods are outlined. Then, measurements performed on elements in the pristine state[11] are discussed for the case of constant positive bias, followed by a short discussion of pristine measurements at negative polarity. Thereafter, we return to voltage sweeps of alternating polarity and discuss the role of the electric field as the driving force for memristive functionality. Finally, a brief discussion of the temporal stability of the induced resistive states is presented.

[11] We define the pristine elements as elements never treated by a bias voltage higher than 20 mV.

THE FOCUS on pristine elements can be understood as a cautious approach to resistors with memory. The topic was not previously

investigated in our research group and there were no established experimental methods known from the literature. The question was, how to prepare reproducible measurements? Not knowing how the 'history' is affecting the internal state (just because the system is driven back to some resistance value does not mean that the internal state of the device is reestablished), we started with the pristine state as the only distinguished one. From measurements on numerous TMR elements we were able to obtain a statistical picture of the switching ratio and speed.[12]

[12] P. Krzysteczko et al., J. Magn. Magn. Mater. **321**, 144 (2009)

THE COMBINATION of resistive switching with TMR allows to investigate fundamental properties of memristors. Due to the spin-dependent transport it is possible to push different currents through the device at the same bias. All barrier properties are the same in the P and AP state and the role of the electric field as the driving force for memristive functionality can be studied. Measurements of this kind might lead to new insights into the physics behind resistive switching. First results presented in this thesis point to the preeminent role of the Joule heating and indicate that a quantitative evaluation must be based on temperature dependent measurements.

THE TUNABILITY of the resistance goes hand in hand with a tunability of the TMR ratio. This can be exploited in the preparation of FPGAs. Based on MTJs, these arrays offer a possibility for nonvolatile data storage and reconfigurable computing. For reliably working FPGAs, a vanishing variation of the TMR ratio within an array of TMR elements is of major importance.[13] Despite all efforts during the preparation process, however, a slight variation of the TMR ratio is unavoidable. This variation can be eliminated by memristive means, i.e., by well-directed application of stress voltage. This is pictured in figure 4, where the accessible TMR-ratio range is enclosed by the two curves.

FPGA
Field programmable logic gate array

[13] G. Reiss et al., Appl. Phys. Lett. **88**, 043505 (2006)

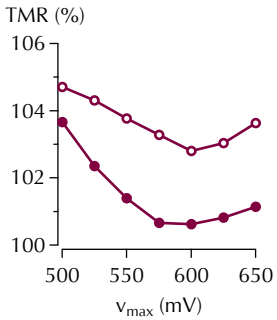

Figure 4: The variation of the TMR ratio induced by voltage sweeps with the amplitude v_{max}. The maximum TMR ratio is indicated by circles, the minimum TMR ratio by bullets.

Models for the resistive switching of MTJs To explain bipolar resistive switching, an asymmetry within the system is required. There must be a 'top' and a 'bottom' so that the current direction can be defined unambiguously. For MTJs, this symmetry break is induced by the sputter process. The bottom interface of the metal-insulator-metal system is fabricated by sputter deposition of MgO on top of Co-Fe-B. During this step of preparation, oxygen is released from the MgO target to the sputter chamber and can react

with the metals of the bottom electrode. The top interface, on the other hand, is fabricated by deposition of Co-Fe-B on top of an MgO layer. Here, the oxygen is embedded within the MgO lattice and will not react as easily with the metals of the top electrode. In this context, and based on the previously presented experimental evidence, a particular model of resistive switching of MTJs is developed in this section.

THE DISCOVERY of resistive switching of MTJs[14] encouraged investigations of *nonmagnetic* resistive cells based on MgO.[15] On the other hand, the TMR-research may profit from the models developed in the field of resistive switching. For example, the diffusion of B atoms and the formation of BO_x complexes induced during the postannealing process in ultra-thin MgO barriers is still under debate.[16] We take first steps in this direction, creating a simple model based on degeneration and regeneration of the interfaces. The model can be extended to state-of-the-art junctions, as confirmed by the similarity between our experimental results and the *R-v*-loops modeled by Rosenberg et al.[17] (see fig. 5).

[14] P. Krzysteczko et al., Appl. Phys. Lett. **95**, 112508 (2009); and J. M. Teixeira et al., J. Phys. D: Appl. Phys. **42**, 105407 (2009)

[15] H.-H. Huang et al., Appl. Phys. Lett. **96**, 193505 (2010)

[16] J. Cha et al., Appl. Phys. Lett. **91**, 062516 (2007); and J. Cha et al., Appl. Phys. Lett. **95**, 032506 (2009)

[17] M. J. Rozenberg et al., Phys. Rev. B **81**, 115101 (2010)

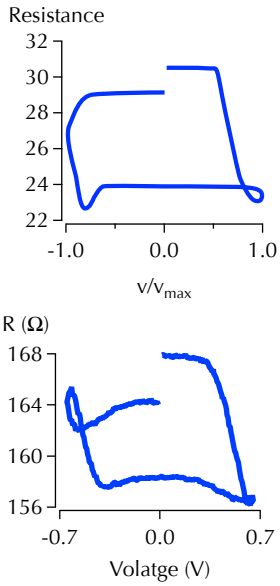

Figure 5: Qualitative similarity of calculations for a resistive system (top) and measurements on a memristive MTJ (bottom).

LTP
Long-term potentiation

LTD
Long-term depression

Artificial synapses & neurons

Neural networks Artificial neural networks are systems that permit computers to function in a manner analogous to that of the human brain. Instead of manipulation of 0s and 1s they create weighted connections (synapses) between switching elements (neurons). This allows for data to be read and stored in ways that resemble human learning and memory. Biologically inspired networks have opened up new possibilities to apply computation to areas that were previously thought to be the exclusive domain of human intelligence.

Before we discuss possible applications of memristive MTJs in artificial networks, some of the fundamental characteristics of biological neural networks are introduced. The main 'circuit elements' of the human brain are the neurons and the synapses. The neurons communicate by exchanging electrical pulses (spikes) via synapses. The strength of the synaptic connection is variable. Repetitive electrical activity at a synaptic connection can induce a persistent increase or decrease of synaptic efficacy, commonly referred to as LTP and LTD. This long lasting plasticity is believed to be the basis of learning and memory.

In the conventional (Hebbian) concept of learning, the synaptic connection is strengthened by the coincident activity of the con-

nected neurons: 'neurons that fire together, wire together.' In the past few years, a series of experiments, using techniques that allow for direct observation of temporally correlated presynaptic and postsynaptic spikes with millisecond precision, have revealed a new picture.[18] These studies suggest that, instead of mere coincidence, the precise timing of presynaptic and postsynaptic spikes (STDP) plays a decisive role in determining the type of synaptic modification.

[18] H. Markram et al., Science **275**, 213 (1997); J. Magee et al., Science **275**, 209 (1997); and C. Bell et al., Nature **387**, 278 (1997)

STDP
Sike-timing-dependent plasticity

Synaptic behavior of MTJs The topic of this section is to introduce the experimental techniques common in the field of neuroscience and apply it to memristive MTJs. A set of data is collected and used to elaborate the similarities between biological synapses and memristive MTJs. The experiments reveal that the repeated treatment with spike trains (voltage pulses) is capable of gradual resistance-changing of a memristive MTJ. The resistivity (or better the conductivity) is comparable to the strength of a synaptic connection. Due to the bipolar nature of resistance change, LTP as well as LTD is emulated. Furthermore, we show that the flux is a 'good' variable to describe spike induced resistance variation.

Memristive synapses In this section, we demonstrate that memristive MTJs intrinsically exhibit characteristics of both, synapses and neurons. The discussion is based on recent neurobiological literature, on the one hand, and measurements designed to demonstrate those features for memristive MTJs, on the other hand.

As an example, the LTP of a hippocampal synapse is shown in the top graph of figure 6 while the increase in conductivity of a memristive MTJ is presented below. From figure 6 a striking qualitative similarity between biological and artificial synapses can be observed. The LTD observed in hippocampal measurements is equally well emulated by memristive MTJs. From those qualitative agreements we conclude that memristive MTJs bear strong resemblance to biological synapses, though, on shorter timescales and with reduced modification rates.

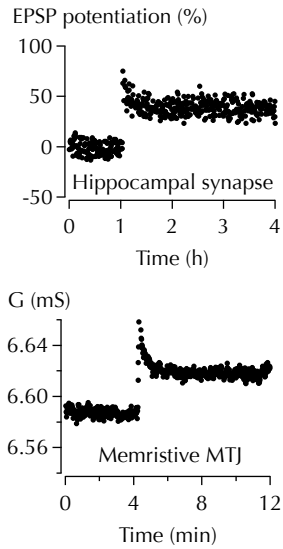

Figure 6: Similar response of biological and artificial synapses to a series of stimuli. The top graph is reproduced from Bilss et al., Nature, **361**, 31 (1993)

Since LTP and LTD were found to be a built-in feature of memristive MTJs, the next natural step is to demonstrate STDP. To do so, we use the well-defined dependence of the resistance on the flux. We follow the scheme proposed by Linares-Barranco et al.[19] and demonstrate the asymmetric spike-timing window—the most important feature of STDP—for memristive MTJs.

[19] B. Linares-Barranco et al., Nature Precedings (2009)

The potential of memristive MTJs is fully exploited when we turn the attention from synapses to neurons and from the barrier properties to the magnetic properties of MTJs. With a new sight on a phenomenon known as back-hopping,[20] we are able to demonstrate that memristive MTJs, in principle, can also emulate the neuron. The back-hopping leads to a periodic switching between the P and AP magnetic state mediated via spin transfer torque. Corresponding to the spiking of a biological neuron, this process is unipolar and characterized by a fixed amplitude.

[20] T. Min et al., J. Appl. Phys. **105**, 07D126 (2009)

The simultaneous occurrence of synaptic and neuron-like behavior in one nanoscopic TMR element represents the simplest implementation of neuromorphic hardware available to date. Since in a neural network synapses outnumber neurons by orders of magnitude, synapses and neurons would be represented by different elements. However, since both could be etched from the same wafer, memristive MTJs may become very attractive for mass fabrication of artificial neural networks.

Further work

In this section, we allude briefly to the results obtained in collaboration with Dr. Vladislav Demidov and Prof. Sergej Demokritov from the Münster University. These results are *not* part of the current thesis and shall be discussed solely at this place. All experiments were designed and carried out by the Münster group. The contribution of our group was the preparation of samples. This was done by standard nanofabrication involving sputter deposition, electron beam lithography, and ion beam etching.

The combination of microfocus Brillouin light scattering spectroscopy with nanoscale patterning techniques let to the discovery of self-focusing of spin waves in Permalloy microstripes. This effect was attributed to the nonlinearity of the spin system of metallic magnetic films[21] together with microscopic-scale confinement effects. Further use of these unique properties of spin waves enabled the manipulation of spin-wave beams, such as channelizing and splitting. This demonstrated that spin waves are superb candidates for microwave-frequency signal processing on the nanometre scale.

[21] Earlier results were obtained on macroscopic yttrium-iron-garnet films. See Bauer et al., Phys. Rev. Lett., **81**, 3769 (1998)

The Memristor

A brief history of the memristor

The Memristor was invented twice. First, as a three terminal device introduced by Bernard Widrow in 1960. It already had the most features we think of today when we say 'memristor': the name as a contraction for 'resistor with memory,' the resistance which can be changed reversibly, and the application to artificial neural networks as an analog of synapses.[22] Widrow developed the memristor as a circuit component forming the basis of an adaptive pattern classification machine called ADALINE. This machine was capable of adaptive behavior and artificial learning. During a training phase, geometric patterns were fed to the machine by setting toggle switches of an input switch array. The output was shown to the operator on a meter scale. If the output was wrong, the operator could change the weighting of each input switch to minimize the error. The system learned something from each pattern and the total experience was stored by the weight values.

In the first attempt, the weights were implemented by an according array of potentiometers. It was clear to Widrow that in order to get the ADALINE neuron ready for mass production, it was necessary to store weight values in such manner that these values could be changed electronically. To do so, he developed a variable resistor[23] working on the basis of electroplating.[24] The resistance was controlled by deposition/dissolution of copper on a graphite substrate in an electrolyte bath. For an ideal memristor, the conductance should vary linearly with total plating charge. To achieve this characteristic, the following requirements need to be met: the plating process has to be reversible, the resistance has to stay put indefinitely when the plating current is zero, the conductance should vary smoothly with plating current, and there should be no hysteresis associated with the change in plating direction.

[22] B. Widrow, Stanford Electronics Laboratories Technical Report **1553**, 1 (1960)

ADALINE
Adaptive linear

[23] Widrow called it memistor. Today, however, the spelling with 'r' became accepted and will be used in the following.

[24] In electroplating, a common system involves a chemical solution with the ionic form of a metal, an anode which may consist of the metal being plated, and a cathode. At the cathode electrons are supplied to produce a film of non-ionic metal on the anode.

All the following attempts to create a memristor—including the memristive tunnel junctions giving the title to this thesis—can be understood as the search for a nanoscopic potentiometer-like device which is self-driven according to the current flowing through it.

THE SECOND TIME THE MEMRISTOR was postulated from an axiomatic point of view. The basic circuit elements of electronics are defined in terms of a relationship between the fundamental circuit variables—the current, the voltage, the charge and the magnetic flux. Out of six possible combinations of these variables only one remains undefined, namely the relation between flux and charge. Leon Chua suggested in 1971 that for the sake of completeness an element must exist that fits into this gap. Such an element would be not less basic than the classical circuit elements—the resistor, the inductor and the capacitor.[25]

[25] L. Chua, IEEE Trans. Circuit Theory **18**, 507 (1971)

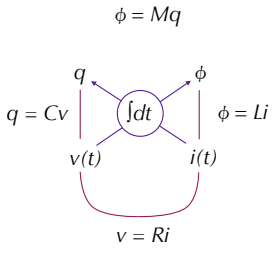

Voltage: $v(t)$
Current: $i(t)$
Charge: $q = \int i(t)dt$
Flux: $\phi = \int v(t)dt$
Capacity: $C = q \div v$
Inductance: $L = \phi \div i$
Resistivity: $R = v \div i$
Memristivity: $M = \phi \div q$

Figure 7: The relationship between the four fundamental circuit variables. A gap between the charge and the flux demands a new circuit element: the memristor.

The diagram in figure 7 illustrates Chua's reasoning. The diagonal lines represent temporal variation. The current i is defined as the time derivative of the charge q. The flux ϕ is the time integral of the voltage v; this being Faraday's law of induction. The outer lines stand for the classical circuit elements. The capacitance constitutes the relation between the charge and the voltage ($q = Cv$). The voltage and the current are connected via the resistivity ($v = Ri$); this being a consequence of Ohm's law. Finally, the inductivity forms the connection of current and flux ($\phi = Li$). Now, there is a missing link on top of figure 7 which would connect the flux ϕ with the charge q. Chua called the missing value memristance M. Why this name? We consider the general, nonlinear case where M is a function of q. The voltage across a (charge controlled) memristor is given by

$$v(t) = M(q(t))\, i(t) \tag{1}$$

$$q(t) = \int_0^t i(t')\mathrm{d}t' \,, \tag{2}$$

where equation 2 is the definition of electric current. The memristor 'remembers' the history of the applied current $i(t)$ since its resistivity depends on $\int i(t)\mathrm{d}t$. Thus its name as a short form of 'resistor with memory.' If charge is pushed through the device the memristivity will be increased or decreased according to the current polarity—this is how information is written. If the current is switched off, or at least remains below a critical threshold, the last value of M will remain unchanged. This is how information is stored.

In the more general concept of an nth order memristive system, equation 1 turns into

$$v(t) = M(\vec{w}, v, t) i(t) \quad (3)$$

$$\dot{\vec{w}} = f(\vec{w}, v, t)\,, \quad (4)$$

where the vector $\vec{w} = (w_1, w_2, \ldots, w_n)$ is a set of n variables describing the state of the device.[26] Notable special cases of a memristive system exist when $M(\vec{w}, v, t) = M(w)$ and $\mathrm{d}w/\mathrm{d}t = i(t)$. This is the case of the originally defined memristor—the so-called pure memristor—introduced by equation 1. The case $M(\vec{w}, v, t) = M(w)$ and $\mathrm{d}w/\mathrm{d}t = 0$ correspond to an ohmic resistor.

[26] L. Chua et al., IEEE Proc. **64**, 209 (1976)

For more than thirty years there was hardly any progress on the memristive field, until Stanley Williams et al. presented measurements on $Pt/TiO_2/Pt$ sandwiches[27] and connected the ideas developed by Chua with the field of *resistive switching*.[28]

Recently, the concept of memristive systems was generalized even further by introduction of memcapacitive and meminductive systems.[29] This circuit elements are characterized by a variable capacitance $C(w, t)$ and inductivity $L(w, t)$ where w is a state variable. In some sense this progress softens up the original idea of the memristor as the missing fourth elementary circuit element. It seems rather that all three 'old' elements have now their mem-counterparts, but the true missing link (and its mem-counterpart) remains elusive.

[27] D. B. Strukov et al., Nature **453**, 80 (2008)

[28] Also referred to as electroresistance, electrochemical metallization, or conductive bridging. A brief introduction to this effect will be given on page 22; a detailed discussion begins at page 30.

[29] M. D. Ventra et al., IEEE Proc. **97**, 1717 (2009)

Memristive behavior of MTJs

MTJ
Magnetic tunnel junction

RAM
Random access memory

There is no such thing as too much memory when it comes to electronic gadgets. Whether it is more Flash memory for taking high-resolution digital pictures, or more RAM to view them on the computer. Dynamic RAM which is omnipresent in today's computers, but must be powered continuously to keep its memory state. By contrast, Flash memory offers nonvolatile data storage, but this advantage comes at the price of slow write speed and a limited number of write/erase cycles. Nonvolatile data retention is desirable because it does not consume any battery power. But there is also a more weighty reason for the need of new memory concepts. Traditional memory technologies are rapidly approaching miniaturization limits as the industry moves toward memory cells with just a few nanometers in lateral size. The reason is that they are based on charge storage and it becomes increasingly

difficult to reliably retain sufficient charge (electrons) within the shrinking cells.

MIM
Metal-insulator-metal

Capacitor-like MIM structures composed of insulating materials sandwiched between metallic electrodes are envisioned to overcome the limitations associated with conventional charge storage devices.[30] This family of nonvolatile memory concepts is based on resistance change rather than charge storage. Together with phase-change memories[31] two concepts attracted extensive interest: resistive and magnetoresistive RAM.

[30] G. I. Meijer, Science **319**, 1625 (2008)

[31] S. R. Ovshinsky, Phys. Rev. Lett. **21**, 1450 (1968); and M. Wuttig et al., Nature Mater. **6**, 824 (2007)

In **resistive** RAM, electrochemical processes within the **insulator** are responsible for the resistance change. Particularly, the movement of oxygen vacancies in the applied electric field is believed to play the dominant role in the modulation of the conducting state of these devices. Electrical pulses of opposite polarity applied to these memory cells switch the resistance between an HRS and an LRS. This effect—usually called resistive switching—will be described in detail on page 30. For an excellent review article see Waser et al.[32]

HRS
High resistive state

LRS
Low resistive state

[32] R. Waser et al., Adv. Mater. **21**, 2632 (2009)

For **magnetic** RAM the TMR effect is used. Here, ferromagnetic **electrodes** are responsible for the resistance change. By changing the electrode's relative magnetization alignment, the fact that the electron current is composed of spin-up and spin-down carriers is exploited. Electrons interact differently with magnetic materials depending on their spin state. This leads to a spin-dependent transport of electrons, i.e., to a conductivity which is influenced by the magnetization of the electrodes. The insulating layer has to be thin enough so that electrons can *tunnel* from one ferromagnet into the other. Since this process is forbidden in the classical physics, the TMR is a strictly quantum-mechanical phenomenon. Numerous reviews on TMR are available.[33]

TMR
Tunnel Magnetoresistance

[33] J. Moodera et al., J. Magn. Magn. Mater. **200**, 248 (1999); S. Yuasa et al., J. Phys. D: Appl. Phys. **40**, R337 (2007); and C. Chappert et al., Nature Mater. **6**, 813 (2007)

The spin-dependent transport is exploited most effectively when the magnetization alignment is changed from parallel to anti-parallel. This bistable configuration is induced by two methods. First, the bottom magnetic layer (pinned layer) is coupled to an antiferromagnet. The magnetization direction of the pinned layer stays almost unchanged in an external magnetic field in the range of $\pm 500\,\mathrm{Oe}$. The top magnetic layer is not affected by the pinning and can rotate freely (free layer). This asymmetry is further supported by the elliptical shape of the TMR elements. Due to the shape anisotropy, the magnetization direction of the free layer is favorably oriented in the direction of the major axis of the

ellipse. Thus, the P and AP states of an elliptical element are well separated even in zero magnetic field. This is illustrated in figure 8, where a typical magnetic (minor) loop is shown. The magnetic layers are aligned in parallel if an external magnetic field of more than +88 Oe is applied. The sample stays in the P state unless the field direction is reversed and a field strength of −93 Oe is reached. Here, the magnetization direction of the free layer is reversed while the pinned layer remains unaffected—the system is switched to the AP state. The efficacy of the spin-dependent transport can be judged by the TMR ratio defined as

$$TMR = \frac{R_{AP} - R_P}{R_P}, \tag{5}$$

where R_{AP} and R_P are the resistance of the AP and P sate, respectively.

Usually the magnetization of the ferromagnetic layers is manipulated by an external magnetic field. The STT switching of magnetization by injection of a spin polarized current, however, is an important new concept in magnetism.[34] It brings great advantages to magnetic RAM, programmable magnetic logic, and sensors using the TMR effect since it makes the external magnetic field obsolete. In cutting-edge MgO-based MTJs, STT requires current densities of about 1×10^6 A/cm^2. This may lead to a melting of the TMR element due to Joule heating if the voltage drop across a 'thick' barrier is too large. A constant trend to reach lower area-resistance products forced the fabrication of MTJs with barriers as thin as 1 nm. Further reduction of the tunnel barrier thickness led in some cases to atypical resistance changes independent of the orientation of the magnetic layers and was attributed to electromigration in the insulating barrier.[35] Up to now, these first reports of resistive switching within TMR systems are followed by only few more publications.[36]

SUBSTANTIAL EFFORT was invested in *separated* studies of resistive and magnetoresistive systems. The next step appears to be a combination of both effects in one device. These devices can be treated as 2nd order memristive systems with w_1 giving the state of the barrier and w_2 describing the magnetic state of the electrodes[37] (see equation 3). The change of w_1 is voltage induced (voltage controlled memristor), whereas w_2 changes driven by the current (current controlled memristor). In this framework, we present studies on MgO-based low resistive magnetic tunnel junctions with Co-Fe-B electrodes. The samples are characterized

P
Parallel

AP
Anti-parallel

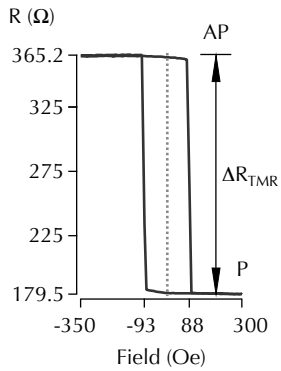

Figure 8: The magnetoresistive switching of the Co-Fe-B/MgO/Co-Fe-B MTJ is characterized by the magnetic minor loop. The dashed line indicates zero magnetic field. The lithography is regarded as successful when a separation of the P and AP states at zero field of about 100 % is obtained.

STT
Sin transfer torque

[34] J. Slonczewski, J. Magn. Magn. Mater. **159**, L1 (1996); and J. A. Katine et al., J. Magn. Magn. Mater. **320**, 1217 (2008)

[35] J. Ventura et al., Phys. Rev. B **72**, 094432 (2005); and J. Ventura et al., IEEE Trans. Nanotech. **5**, 142 (2006)

[36] D. Halley et al., Appl. Phys. Lett. **92**, 212115 (2008); C. Yoshida et al., Appl. Phys. Lett. **92**, 113508 (2008); H.-H. Huang et al., Appl. Phys. Lett. **96**, 193505 (2010); and N. Najjari et al., Phys. Rev. B **81**, 174425 (2010)

[37] X. Wang et al., IEEE Electron Device Lett. **30**, 294 (2009)

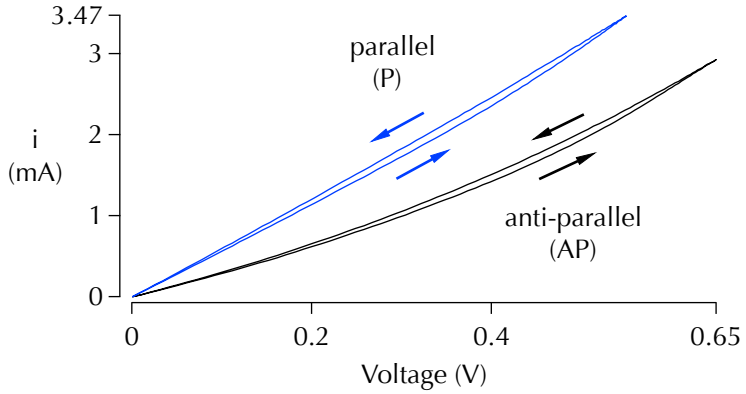

Figure 9: Simultaneous occurrence of resistive and magnetoresistive switching. The magnetic states are set by an external magnetic field of ±400 Oe. A slight splitting of the *i-v* curves can be observed for both magnetic states. This demonstrates the presence of resistive switching. Since the curves are highly symmetric with respect to the origin, only the first quadrant is shown.

by TMR ratios of about 100 % and exhibit an additional bipolar resistive switching of up to 12 %.

The concurrent resistive and magnetoresistive activity can be seen from figure 9 where the current-voltage (*i-v*) curves for the P and AP orientation of the Co-Fe-B electrodes are shown. For each curve, the current value measured for increasing voltage is slightly lower than the current measured for decreasing voltage. This splitting of the *i-v* curve—also called hysteresis—is the characteristic indication of memristive behavior.[38]

The shape of the *i-v*-curve for each magnetic state is not only determined by the vacancy drift within the barrier, but also by the voltage-dependent tunneling process.[39] In order to remove this

[38] D. B. Strukov et al., Small **5**, 1058 (2009)

[39] W. Brinkman et al., J. Appl. Phys. **41**, 1915 (1970)

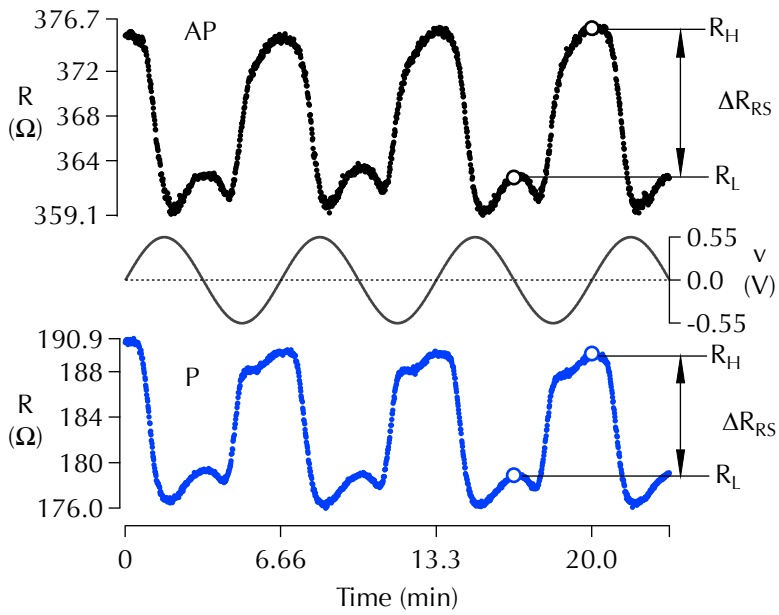

Figure 10: Resistive switching induced by a sinusoidal voltage. The resistance of both magnetic states (AP and P) is switched periodically between two resistive states (R_H and R_L). Labels are attached to the resistance curves (at $v = 0$) to clarify the definition of R_H and R_L.

nonlinear contribution a measurement procedure consisting of alternating read-out and write pulses is used. This is schematically illustrated in figure 11. The measurement begins with a 200 ms read-out pulse of 20 mV, represented by a gray stick. The next pulse is a write pulse, shown in red. The duration of this pulse is one second and the amplitude is $v(t) = v_{\max} \sin(\omega t)$, with the angular frequency ω. In the following, whenever data is presented on the ordinate (y-axis), it is is calculated from the read-out pulses. Data presented on the abscissa, on the other hand, relates to the write pulses. In a $R(v)$-graph, for example, each resistance value is the result of a measurement at 20 mV performed *after* a voltage pulse v was applied for one second. In this way, the resistance is monitored at a constant bias and the voltage is swept.

The variation of the MTJ's resistance induced by a sinusoidal voltage is shown in figure 10. A positive bias leads to resistance decrease; a negative bias leads to resistance increase. As a result the resistance of both magnetic states is periodically switched between a HRS and a LRS with the same periodicity as the applied voltage. Minor fluctuations can be observed in both states. They are mainly due to thermoresistive effects as will be discussed below. We define the values R_H and R_L (indicated by the circles) as the resistance at zero voltage to fix the rather ambiguous terms HRS and LRS, respectively.

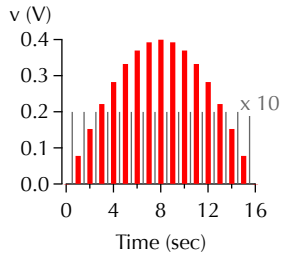

Figure 11: Measurement procedure. The applied voltage consists of alternating pulses. The read-out pulses of 20 mV are shown in grey. The write pulses, shown in red, are enveloped by a sine function.

Figure 12: Two complementary methods to display the voltage-induced resistance modification. The bipolar resistive switching between two stable resistance states is displayed most clearly when plotted vs. voltage. The hysteretic nature of resistive switching is is shown with clarity when plotted vs. flux. The AP state is shown in black, the P state in blue. In each case 2.5 loops are plotted on top of each other to demonstrate reproducibility.

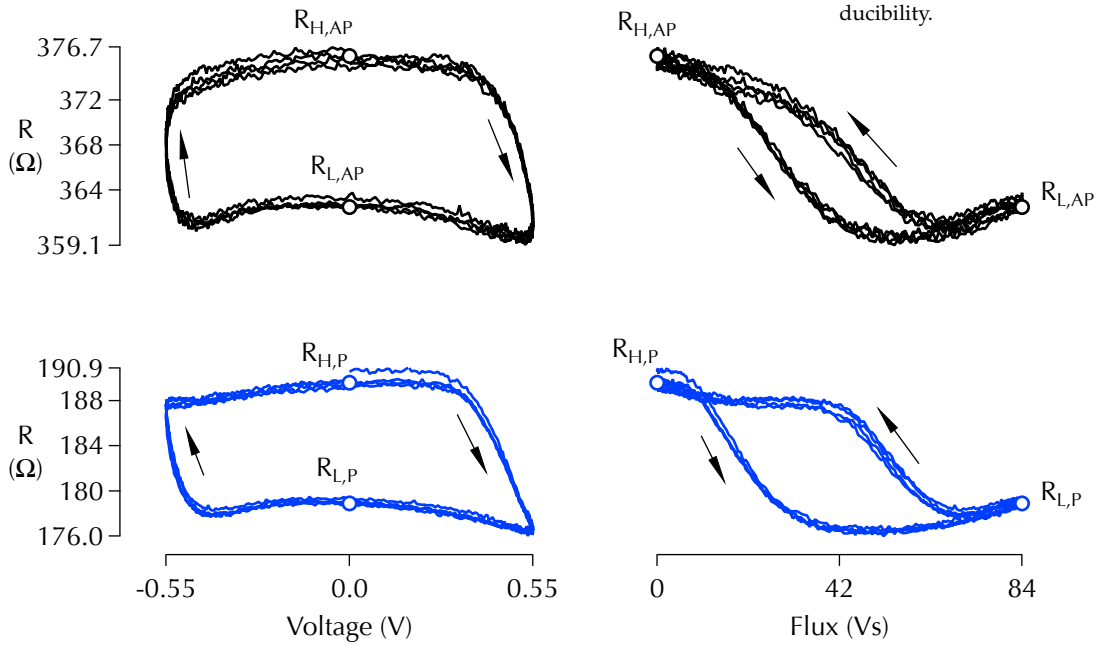

It is useful to present the resistance data furled up to resistive loops.[40] This allows to demonstrate the reproducible nature of the switching process and analyze the memristive behavior in more detail. Figure 12 shows the resistance as a function of the applied voltage and as a function of the flux for both magnetic states—the AP state shown in black and the P state shown in blue. Let us consider the R vs. v curve in the P state (bottom left). Starting at $R_{H,P}$ the resistance remains stable until a critical voltage of about 0.37 V is reached. Here, the resistance drops reaching the lowest value for maximum bias voltage. A slight increase of the resistance can be observed when the applied voltage is reduced. A similar switching process appears in opposite direction after the polarity of the applied voltage is changed and a critical voltage of −0.42 V is reached.

[40] N. Das et al., Phys. Rev. B **78**, 235418 (2008); N. Das et al., Phys. Rev. B **80**, 115411 (2009); Y. Liu et al., Appl. Phys. Lett. **82**, 2871 (2003); and Y. Nian et al., Phys. Rev. Lett. **98**, 146403 (2007)

The same data has been replotted as a function of flux ϕ (bottom right curve in figure 12). The graph shows the hysteretic nature of the resistance when plotted vs. ϕ. We omit the magnetic flux interpretation of ϕ and define its value at a time t after n voltage pulses as $\phi(t) = \sum_{i=0}^{n} v_i t_i$, with v_i and t_i the voltage and duration of the ith pulse, respectively. The flux 'applied' to the sample increases when a positive voltage is applied and decreases for negative polarity. For increasing flux the resistance decreases slightly until a flux of about 14 Vs is reached and the resistive switching begins. The minimum of the resistance is reached at about 42 Vs before the resistance increases slowly reaching $R_{L,P}$ at 84 Vs. The back-switching begins at 67 Vs leading to a pronounced resistive hysteresis.

RS
Resistive switching

We calculate the RS ratio using the same definition as for the TMR ratio

$$RS = \frac{R_H - R_L}{R_L} \tag{6}$$

and obtain rather small values (see table 1). It might be possible to increase them to a level attractive for (digital) data storage devices.[41] The true advantage of the memristive MTJs, however, lies with the continuous switching between HRS and LRS, as will be further discussed in the third chapter.

[41] D. B. Strukov et al., Appl. Phys. A **94**, 515 (2009)

Table 1: Resistive (RS) and magnetoresistive (TMR) effects calculated from the data presented so far. The index to ΔR is denoting the (magneto)resistive state of the device. ΔR is the total resistance change due to the effect denoted by the index.

	R_H	R_L	ΔR_{RS}	RS
R_{AP}	375.9 Ω	362.5 Ω	13.4 Ω	3.7 %
R_P	189.6 Ω	178.9 Ω	10.7 Ω	6.0 %
ΔR_{TMR}	186.3 Ω	183.6 Ω		
TMR	98.3 %	102.6 %		

How the presented system differs from a pure memristor

As pointed out previously, a possible explanation for the RS of MTJs is a displacement of oxygen vacancies located at the bottom Co-Fe-B/MgO interface. We performed measurements on MTJs with an MgO barrier prepared by post-oxidation[42] of an Mg layer to study this model in more detail. The bottom Co-Fe-B electrode is not exposed to oxygen using this preparation method and no oxygen vacancies at the bottom interface are expected.[43] The corresponding measurement is shown in figure 13. Two features are noted. First, no $R(\phi)$-hysteresis can be detected indicating the absence of resistive switching, as expected. Second, a V-shaped curve is observed with the resistance lowered by (only) 0.62 % in the middle of the flux-axis. At this flux the applied voltage reaches its maximum for both polarities. Since the tunneling elements (and the top and bottom conduction lines) are heated due to the high current density the local temperature may not relax during the 200 ms read-out delay. The slight resistance variation (one order of magnitude smaller than RS) can be explained by Joule heating in combination with temperature-dependent tunneling. A similar influence of remnant heat was already visible for the sample with a barrier sputtered directly from an MgO target (vacancies expected). These thermoresistive parts are indicated by blue lines on the left side in figure 14.

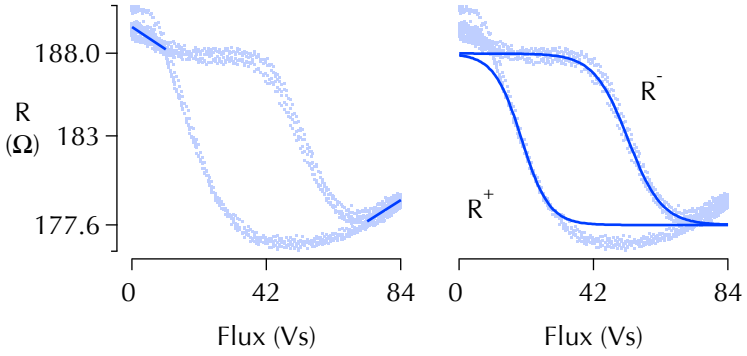

Now, we stress the question how the presented system differs from a pure memristor. Despite the superposition with thermally induced resistance changes, the hysteresis of $R(\phi)$ means that a pure memristor can be defined at best 'branch-wise':

$$R^{\pm}(\phi) = R_{\mathrm{H}} - \frac{\Delta R_{\mathrm{RS}}}{1 + \exp\left((\phi_{\mathrm{S}}^{\pm} - \phi)/\delta^{\pm}\right)}, \qquad (7)$$

[42] The MTJs discussed so far were fabricated by sputter deposition from an MgO target. Here, an Mg target was used resulting in a metallic Mg layer that has to be post-oxidized. The samples are provided by Singulus Inc.

[43] H. Meyerheim et al., Phys. Rev. B **65**, 144433 (2002)

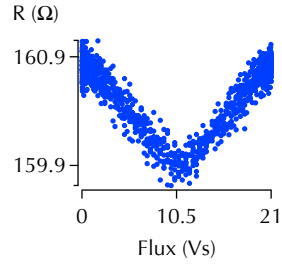

Figure 13: The absence of hysteresis for an MTJ prepared by post-oxidation of MgO. The small (0.62 %) resistive effect is due to Joule heating.

Figure 14: Thermal and 'pure' contributions to the $R(\phi)$-curve are indicated by blue lines. In the background, the experimental data (compare bottom left curve of fig. 12) is shown in light blue. (left) The hysteresis-free part, due to thermal effects. (right) The fitting-curves given by equation 7.

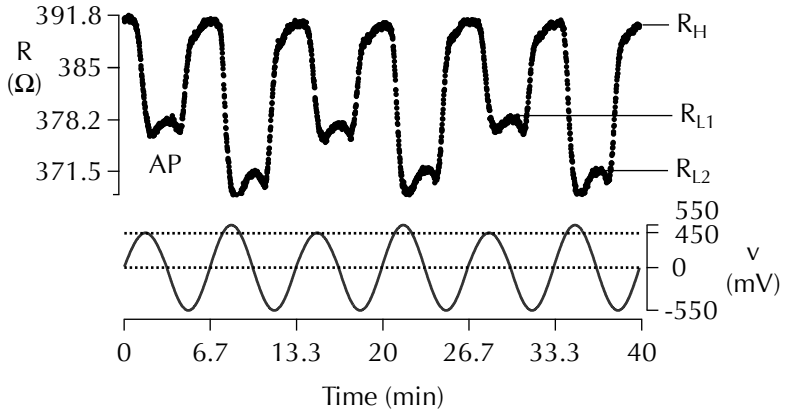

Figure 15: Influence of an asymmetric input on the R_L state. The positive amplitude of the stress voltage is periodically switched between 450 mV and 550 mV. This leads to a splitting of the low resistance state into R_{L1} and R_{L2} separated by 6.7 Ω.

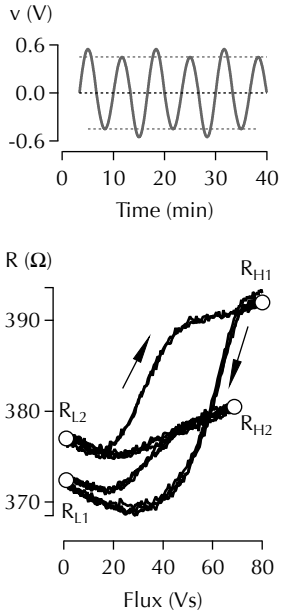

Figure 16: Example of a complex $R(\phi)$-curve. (top) Input signal with modulated amplitude. (bottom) The resulting curve. A splitting of the LRS into R_{L1} and R_{L2} as well as a splitting of the HRS into R_{H1} and R_{H2} is observed.

with $R^+(\phi)$ the resistance on the positive branch ($v > 0$), $\phi_S^+ = 19.5$ Vs the inflection point and $\delta^+ = 4.3$ Vs indicating the sharpness of the switching process. To fit the negative branch $R^-(\phi)$ we shift the inflection point to $\phi_S^- = 52.8$ Vs and use $\delta^- = 5.3$ Vs. Both fitting curves are shown on the right side in figure 14 by blue lines.

A simple $R(\phi)$-hysteresis as presented so far will only result from a sinusoidal voltage of constant amplitude. For example, if the positive amplitude is alternated between two values an additional R_L state is generated. As illustrated in figure 15, the LRS is split into two states; R_{L1} and R_{L2}. The HRS remains stable since the negative amplitude is constant. In general, multiple resistance states—both, high and low—can be created by according amplitude variation.

Due to the asymmetry in the input voltage—every second positive half-wave is higher than the other half-waves—a presentation of the data by an $R(\phi)$-curve is inappropriate. The curve would 'swim' in the direction of positive flux since the extra flux from the symmetry-breaking half-wave ($v_{max} = +550$ mV in fig. 15) would not be compensated by a corresponding negative half-wave. To avoid this effect, the applied voltage has to be composed of full waves with alternating amplitude. A $R(\phi)$-curve that exemplify a symmetric input signal is pictured in figure 16.

Resistive switching

The concept of a memristor is not connected to any particular realization of a device. Yet, a great body of literature is dedicated to memristors based on resistive switching. In the first section of this chapter, we give an overview of different mechanisms proposed as the origin of various voltage-actuated switching phenomena summarized under the collective term *resistive switching*. In the second section, the characteristic features of memristive MTJs are presented in a phenomenological manner. In the last section particular models are developed in the context of previously presented experimental evidence.

General models

We cannot consider resistive switching without introducing the basic principles of electrochemistry. As the name suggests, electrochemistry deals with the relationship between electricity and chemical reactions. In many respects, batteries are the prime example for electrochemical devices; the movement of ions and the change in their oxidation state within the battery is used to release electrical energy over time. However, since ions do not only carry charge but also mass, we can look at ion transport as a method to move material in a controlled manner. An atom that becomes oxidized at one side of an electrolyte can be moved by means of electric field. On receiving an electron at the other side of the electrolyte, the displaced ion is reduced and becomes neutral again. In this situation, the net change in the system is the redistribution of mass—material is removed from one location and deposited at another using energy from an external power source.

The world of electronics has benefited from such deposition for many decades. Electroplating, in which metal ions in a liquid solution are reduced to create an uniform metal film, is widely used. Typically, the dimensions involved are quite large. Electrode spac-

ing can be in the order of millimeters. The term nano-ionics[44] is applied when electrochemical effects occur in materials and devices with electrodes that are closely spaced. In the size regime of few nanometer, the functionality of ionic systems is quite different from the macro-scale versions but in an useful manner. For example, internal electric fields and ion mobilities are relatively high in nanoionic structures and this, combined with the short length scales, result in very fast response times. In addition, nano-ionics can take advantage of the fact that a variety of solid materials are excellent electrolytes, especially at the nanoscale.

[44] J. Maier, Nature Mater. **4**, 805 (2005)

THE LION'S SHARE of research on resistive switching has been performed on (early) transition metal oxide thin films in particular on TiO_2, $SrTiO_3$ and $Pr_{0.7}Ca_{0.3}MnO_3$.[45] The exact mechanism behind the resistive switching across various oxide-electrode interfaces remains elusive despite intense investigations. A variety of models have been proposed and shall be briefly discussed in the following sections.

[45] R. Waser et al., Nature Mater. **6**, 833 (2007)

A general consensus has emerged on the relevance of defects within the dielectric. A number of experiments point to a preeminent role played by oxygen vacancies.[46] Moreover, it is an important feature of transition metal oxides that their resistivity is dramatically affected by the precise oxygen stoichiometry. One may thus expect that oxygen vacancy concentration may be the significant parameter controlling the *local* resistivity of a given material. The second important feature is the role played by the interfaces, namely, the regions of the dielectric that are in physical proximity to the metallic electrodes. There is growing evidence that these are the regions where the resistive switching takes place. Finally, for a huge class of systems, a *formation step* was found to be needed before stable switching occurred. Several experiments revealed that in this cases the conduction in the LRS is dominated by one-dimensional paths that are associated with enhanced conduction channels. These paths are created upon an initial application of a strong electric field that brings the dielectric close to its breakdown point (formation).

[46] K. Szot et al., Nature Mater. **5**, 312 (2006); and S. Tsui et al., Appl. Phys. Lett. **85**, 317 (2004)

Since the subject is quite complex it will be broken up under various headings. We arrange the main models in three groups depending on how the resistance change is induced.

Thermally induced

In this class, the switching is dominated by the fuse-antifuse mechanism. The switching direction does not depend on the polarity of the voltage (unipolar switching). The system is not ready for operation until a forming step related to a soft dielectric breakdown is carried out. A control unit is required to limit the current to a compliance value during the forming as well as during normal operation.

We begin with the description of the forming step. Typically, the dielectric breakdown is induced by a thermal runaway. By applying an electric field, the residual conductivity σ of the insulating material leads to local generation of Joule heat. Due to the exponential temperature dependence

$$\sigma \sim \exp\left(-\frac{W_\mathrm{A}}{k_\mathrm{B}T}\right) \tag{8}$$

the increased temperature T leads to increased conductivity, with W_A the activation energy. This results in higher currents, further temperature increase, and so forth. First, the localized thermal runaway causes a transient LRS which does not result in permanent change in the resistance. If the sample is cooled down at this stage, the system will return to the initial resistance. If the stimulation continues, however, the transient LRS leads to a local redox reaction. Starting at a given (local) oxygen activity at room temperature for any of the higher-valent oxides, a temperature rise of some hundred Kelvin will always lead to a stable oxide with a lower valence or to the corresponding metal (Ellingham diagram).[47] The permanent LRS is established because of oxygen drift out of the high temperature region. The current compliance is needed to stop the thermal runaway at the stage of a soft dielectric breakdown.

Once a weak conductive filament with a controlled resistance is formed the actual switching can be performed. During the RESET transition the current compliance is held inactive, so that the filament is thermally disrupted. This process is similar to the melting of a wire of a household fuse if the current exceeds a safe level. On the nanoscale, however, the connection can be re-established by the antifuse mechanism, in which the redox reaction in the filament and its vicinity comes into play again. For the SET process a limitation of current is needed again.

A recent study on $Pt/TiO_2/Pt$ sandwiches confirmed the existence of highly conductive nonstoichiometric Ti_nO_{2n-1} filaments

[47] The driving force which favors lower valence states at higher temperatures is generic to all stable oxides because of the negative free energy of formation. See, e.g., H. Schmalzried and A. Navrotsky, *Festkörperthermodnamik*, Verlag Chemie, Weinheim 2004

RESET
Switch from LRS to HRS

SET
Switch from HRS to LRS

TEM
Transmission electron microscopy

in the LRS. Extensive high-resolution TEM analysis revealed that the filaments in TiO_2 are composed mostly of Ti_4O_7 and Ti_5O_9. This phases, so-called Magnéli phases, are known to be metallic conductors at room temperature. RESET operation observed in situ by TEM confirmed the dissolution of the Magéli phase to stoichiometric phases by local thermal annealing.[48]

[48] D.-H. Kwon et al., Nature Nanotech. **5**, 148 (2010)

Induced by ion migration

In this class of models the drift of ions in an ion-conducting layer is considered. The switching is bipolar and needs to be initiated by a formation process. In the case of cation migration, metal cations are oxidized from an electrochemically active material and dissolved into the ionic conductor (see fig. 17). They migrate towards the cathode made of inert materials and are reduced there. The reduced metal atoms form a metal filament (since the electric field is enhanced here, the atoms are deposited at the tip of the forming filament). When the filament reaches the anode a shortcut is created and the switch is turned on. The SET process involves the anodic dissolution of electrochemically active metal M according to the reaction

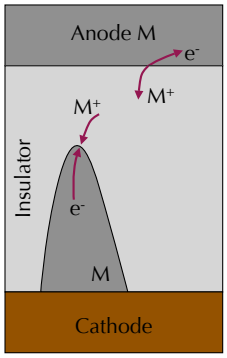

Figure 17: Illustration of the cation migration according to reactions 9 and 10. A possible system could consist of an oxidizable Ag electrode, an insulating layer of Ag-Ge-Se transparent for Ag^+ ions, and a Pt inert electrode.

$$M \rightarrow M^{z+} + ze^- , \tag{9}$$

where M^{z+} represents the metal cations in the solid electrolyte, the migration of the M^{z+} cations across the electrolyte under the action of electric field, and reduction (electrocrystallization) of M on the surface of the inert electrode according to

$$M^{z+} + ze^- \rightarrow M . \tag{10}$$

On changing the polarity of the bias voltage the situation is reversed and the metal ions are dissolved at the edges of the filament, eventually melting down the connection. In the initial phase of RESET there is an electronic current through the metallic bridge and, in parallel, an electrochemical current[49] which dissolves the metal filament.

[49] Also called Faradaic current.

Random read/write cycle times of below 50 nm were demonstrated for state-of-the-art cation-migration-based $Ag/GeSe_x/W$ resistive switching cells integrated into 90-nm CMOS technology.[50]

CMOS
Complementary metal-oxide-semiconductor

[50] S. Dietrich et al., IEEE J. Solid-State Circ. **42**, 839 (2007)

IN THE PROBABLY MORE IMPORTANT CASE the redox process is induced by anion migration. In many transition metal oxides, oxygen related defects, such as oxygen vacancies, are more mobile

than the cations. In this case, a concentration gradient builds up when the electrode interfaces are blocking the ionic partial current.[51] At low voltages the balance of drift and diffusion currents leads to a linear concentration gradient. For larger voltages ($\approx 1\,\mathrm{V}$) the linear transport theory cannot be applied anymore and huge gradients in the defect concentration lead to a significant increase of the oxygen concentration near the cathode.[52]

Typically, the anode is partially transparent to the ionic current and an electrochemical oxidation at the anode may occur. This would lead to the of molecular oxygen and the injection of oxygen vacancies into the oxide. In some cases, the evolution of oxygen is strong enough to cause the formation of entrapped O_2 bubbles.[53] According to the Kröger-Vink notation one writes

$$O_O \rightarrow V_O^{\bullet\bullet} + 2e' + \frac{1}{2}O(\mathrm{gas})\,, \tag{11}$$

where $V_O^{\bullet\bullet}$ denotes oxygen vacancies with a double positive charge with respect to the regular lattice and O_O represents an oxygen ion on a regular site. The vacancies are immediately drawn towards the cathode by the electric field. Because oxygen vacancies are donors, the region in which they accumulate becomes highly *n*-conducting (see fig. 18). Due to the increased conductivity the electric field decreases significantly in this region, leading to a decrease in the oxygen vacancy motion. As a result, the oxygen vacancies accumulate in the so-called virtual cathode. In this case, the foremost filament of the virtual cathode propagates toward the anode. When it approaches and almost touches the anode, the resistance of the MIM system drops and the electroformation is completed. This process introduces the required asymmetry to the initially symmetric MIM system. In many cases, this process advances along extended defects in the lattice as fast migration paths.[54]

After the electroforming, the anodic interface will be the active interface, i.e., the contact at which the switching takes place. Once the foremost virtual cathode filament comes into close vicinity of the anode, the current rises significantly, possibly due to onset of tunneling. Using a local conduction AFM tip as the active electrode connected to the outcome of a filament, the change in doping level by vacancy redistribution can be demonstrated.[55]The application of positive and negative bias leads to repulsion and attraction of O^{2-} ions, respectively. In this process, the barrier becomes narrower (vacancies approach the tip) or wider (vacancies are repelled from the tip) leading to a metal/insulator transition.

[51] The electrons propagate through the entire device whereas the movement of ions is restricted to the electrolyte.

[52] T. Baiatu et al., J. Am. Ceram. Soc. **73**, 1663 (1990)

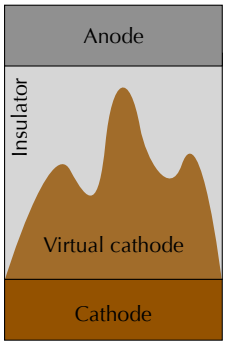

Figure 18: Resistive switching by anion migration. Mobile oxygen vacancies accumulate close to the cathode. The doped region of the insulator becomes conductive and turns into the virtual cathode.

[53] J. J. Yang et al., Nanotech. **20**, 215201 (2009)

[54] K. Szot et al., Nature Mater. **5**, 312 (2006)

AFM
Atomic force microscope

[55] K. Szot et al., Nature Mater. **5**, 312 (2006)

Electrically induced

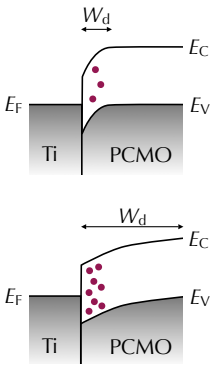

Figure 19: Band diagram of the Ti/PCMO interface. The depletion layer width W_d is modulated by the presence of the oxygen vacancies. Reproduced from Sawa et al., Mat. Today, **11**, 28 (2008)

STO
$SrTiO_3$

SRO
$SrRuO_3$

PCMO
$Pr_{0.7}Ca_{0.3}MnO_3$

Since the memory cell has a capacitor-like structure composed of insulating or semiconducting oxides sandwiched between metal electrodes, a Schottky barrier seems to be the most probable origin of the *contact* resistance. The voltage driven accumulation or depletion of oxygen vacancies within the oxide in front of the active electrode leads to a modification of the Schottky type energy barrier and the corresponding resistive switching (see fig. 19). No formation process is needed and the switching is bipolar. The entire area of the electrode is active in contrast to the previously discussed filamentary models. This picture is supported by results for various active electrode materials with different work functions. The contact resistance of active-electrode material M and an *n*-type oxide, e.g., STO, increases with a growing work function of M. While a cell with a low work function electrode such as Ti shows ohmic *i-v* curves, an electrode made from Au or SRO shows a rectifying *i-v* characteristic. Strikingly, the hysteretic behavior indicative of RS was observed only for the samples with rectifying *i-v* curves. Similar type of RS is also observed in cells made from *p*-type oxides such as PCMO. In *p*-type conducting PCMO cells, the contact resistance M/PCMO increases as the working function of M *decreases*. Again resistive switching was observed only for those M leading to a rectification behavior.[56] Furthermore, these experiments provide insight into the directionality of the switching. The forward bias voltage has different polarity for *n*-type and *p*-type samples. In both cases, however, the SET occurred when forward bias was applied and RESET occurred at reverse bias.

[56] A. Sawa et al., Appl. Phys. Lett. **85**, 4073 (2004)

To understand the role of oxygen vacancies, oxidative treatment of memory cells has been performed. *n*-type cells are transformed into HRS as the reduction of oxygen vacancies leads to a reduction of donors. Consistently, *p*-type cells were transformed to LRS. Here the decrease of oxygen vacancies concentration leads to a decrease of the barrier for hole transport.[57]

[57] A. Sawa, Mater. Today **11**, 28 (2008)

ANOTHER MODEL for bipolar non-filamentary resistive switching can be described as trapping and detrapping of injected electrons in preexisting nano domains. Strong electric fields can inject charge carriers into the conduction band of the insulator (Fowler-Nordheim tunneling). This charge accumulate in inhomogeneous regions of the system, called domains. The model assumes the existence of a non-percolating structure of metallic domains that might correspond to defects, grains, phase separated regions and

so on.[58] Carriers tunnel under the action of an external field. The probability of charge transfer depends on parameters such as the tunneling rates, the number of states in the domain, and their occupation. When the level of occupation attains a given threshold, a doping driven metal-insulator transition is taken into consideration. The carrier transfer probability is reduced due to the decrease of states at the Fermi level when a (Mott) gap opens up in the domain's density of states. As one tunes the domains from one phase to another, the conductance (due to variation in number of states at the Fermi energy) is expected to be different in each phase.[59]

[58] M. Rozenberg et al., Phys. Rev. Lett. **92**, 178302 (2004); M. Rozenberg et al., Appl. Phys. Lett. **88**, 033510 (2006); and M. Quintero et al., Phys. Rev. Lett. **98**, 116601 (2007)

[59] M. Rozenberg et al., Thin Solid Films **486**, 24 (2005)

The phenomenology of resistive MTJs

At the beginning of this section, the experimental details are outlined. Then, measurements performed on elements in the pristine state[60] are discussed for the case of constant positive bias, followed by a short discussion of pristine measurements at negative polarity. Thereafter, we return to voltage sweeps of alternating polarity and discuss the role of the electric field as the driving force for memristive functionality. Finally, a brief discussion of the relaxation measurements will be presented.

[60] We define the pristine elements as elements never treated by a bias higher than 20 mV.

Experimental methods

All measurements are performed using a constant voltage source at room temperature. By applying voltage pulses of one second duration and up to 800 mV the samples are stressed by a current density of $1\text{–}10 \times 10^6\,\mathrm{A/cm^2}$. The bottom electrode is grounded at all times so that the electron flow is from the bottom to the top electrode when a positive bias is applied. A magnetic field of ± 400 Oe provides a stable parallel/anti-parallel orientation of the magnetic layers during the measurements. All resistance values presented in this chapter are measured at a read-out voltage of 20 mV and with a read-out delay of 200 ms after each stress pulse. This removes nonlinear contributions resulting from voltage-dependent tunnel resistance (cf. fig. 11 and the discussion on page 25).

The TMR stacks (see margin table) are sputter deposited in a TIMARIS II tool by Singulus Inc. The films are deposited on Si/SiO_2 substrates by Ar bombardment[61] on a MgO target at room temperature and annealed for 1.5 h at 360°C prior to patterning. The diffusion of B, a glass forming material, out of the

Thickness (nm)	Composition (%)
7	Ru
30	Cu
10	Ta
3	$Co_{66}Fe_{22}B_{12}$
1.3	MgO
2	$Co_{66}Fe_{22}B_{12}$
0.75	Ru
2	$Co_{70}Fe_{30}$
20	$Pt_{37}Mn_{63}$
5	Ta
90	Cu-N
3	Ta

[61] The film sequence is nominally the same for all samples discussed in this chapter. Different conductivity is due to different Ar pressures during the sputter process.

electrodes during annealing enables the crystallization of the electrodes which improves the TMR ratio due to the enhancement of coherent tunneling.[62] Elliptical TMR elements with major axes of typically $150 \times 350\,\mathrm{nm}$ are prepared by electron beam lithography in combination with ion beam etching.

[62] W. Butler et al., Phys. Rev. B **63**, 054416 (2001); and J. Mathon et al., Phys. Rev. B **63**, 220403 (2001)

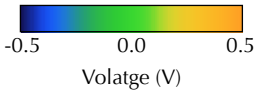

Figure 20: The standard color scale used for $R(t)$-curves throughout the thesis.

In the following, the explanatory presentation of experimental data in the first chapter shall be extended to a systematic overview of the memristive operation of MTJs. The switching of memristive MTJs is bipolar—no formation step is required. To indicate the polarity of the stress voltage a standard color scale as shown in figure 20 is used.

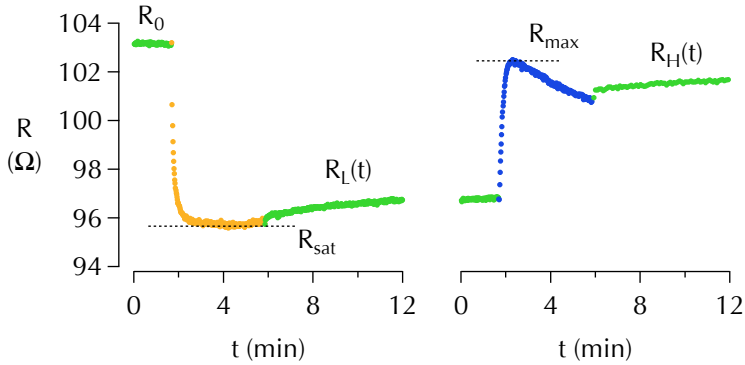

Figure 21: Archetypical curves showing resistive switching of MTJs. For the color scale see fig. 20. The curves on the left and right side are measured at a constant stress-voltage of $+400\,\mathrm{mV}$ and $-400\,\mathrm{mV}$, respectively. Positive current is defined as the electron flow from the bottom to the top electrode.

Archetypical curves are pictured in figure 21. The $R(t)$-curve starts with a premeasurement which gives the resistivity of the pristine state R_0 and also provides a measure of the resistance stability before the actual stressing (green data). If positive stress voltage is applied (orange curve), a fast resistance decrease is observed followed by a saturation at R_{sat}. According to the previous definition, R_{sat} turns to R_{L} as the bias is switched off (end of the orange curve). The relaxation of the LRS is observed by the post-measurement of R_{L} (shown in green). The same procedure for negative stress reveals a nonmonotonic $R(t)$-curve (blue). A fast resistance increase is followed by a slow resistance decrease. We introduce R_{max} as the highest resistance during negative stressing (maximum of the blue curve). Finally, the relaxation of the HRS is shown in green.

Constant positive stress

This subsection deals with measurements on pristine elements. In a somewhat cautious approach each element is measured just once. The simplest case of a constant stress voltage is used. By measurements on numerous elements a statistical picture—independent of singular imperfections during sputter deposition or lithography—is expected. Additionally, the focus on pristine elements is due to the fact that reproducible measurements are challenging for resistors with memory. For example, just because the system is driven back to R_0 does not mean that the internal state of the device is reestablished.

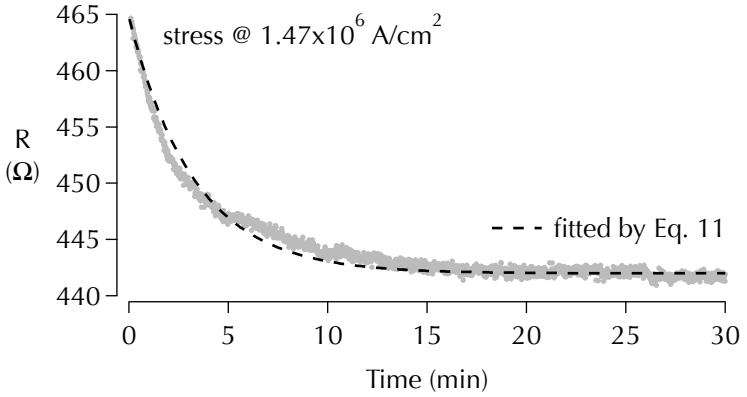

Figure 22 shows an $R(t)$-curve upon stressing with a positive voltage of 300 mV. The area of the elliptical element is 0.043 µm^2 and the area-resistance product[63] is $RA = 9.8\,\Omega\mu m^2$. The area (of the MgO layer) is acquired from scanning electron micrographs of the TMR element with an accuracy of $\pm 5\,\%$. As the device is stressed by $j = 1.5 \times 10^6\,A/cm^2$ one observes a decay of the resistance with time. The initial resistance of $R_0 = 465\,\Omega$ is reduced reaching a saturation resistance of $R_{sat} = 442\,\Omega$ within 30 min. Numerically, the measured time dependence of the resistance can be fitted with moderate quality by an exponential function

$$R(t) = R_{sat} + \Delta R \cdot \exp\left(-t/\tau\right) , \qquad (12)$$

with $\Delta R = R_0 - R_{sat} > 0$. This would represent a process characterized by a decay time of $\tau = 3.15$ min and leads to the dashed line in figure 23. Evidence that the barrier itself does not degrade during stressing is given by figure 24. It shows the magnetic minor loops before (black) and after (gray) stressing. The gray curve is shifted along the H-axis to avoid overlay. The pristine TMR ratio of 104 % is stable after stressing, even slightly increased to 108 %.

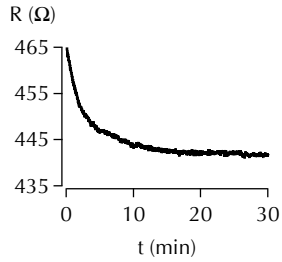

Figure 22: Resistance decrease due to stressing with +300 mV.

Figure 23: Fits to the data shown in figure 22 using equation 12 as shown by the dashed line.

[63] The RA-product is constant for different areas A of the ellipse. It is usually given for the P sate.

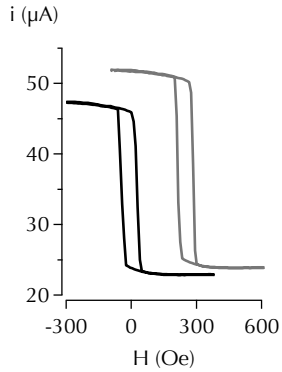

Figure 24: Proof of stable barrier quality. Both magnetic minor loops, before (black) and after (gray) stressing, show satisfactory TMR ratios.

We repeat measurements as presented in figure 22 for different stress voltages, always taking a pristine element. Figure 25 shows the results of measurements on two different sets of samples. The elements of the first set have an area-resistance of $RA = 9.8\,\Omega\mu m^2$ —they were stressed in the AP state (black bullets). The other set is characterized by RA of $4.4\,\Omega\mu m^2$ and was stressed in the P state (blue circles) as well as in the AP state (black circles). For each $R(t)$-curve we use fit parameters obtained by equation 12 to calculate the RS ratio

$$RS = \Delta R / R_{sat}\,. \tag{13}$$

It is most instructive to display RS as a function of the current density j. We define j as the current per area flowing at constant voltage V when the resistance is R_0. For the first set a maximum value of 13 % can be reached at a current density of $j = 4.5 \times 10^6\,A/cm^2$. The example presented in figure 23 is labeled by a red cross. For the lower resistive elements the RS in the AP state is reduced by a factor of approximately 0.45. By contrast, the change in the magnetic orientation of the electrodes (compare black and blue circles) produces no significant difference in the RS ratio.

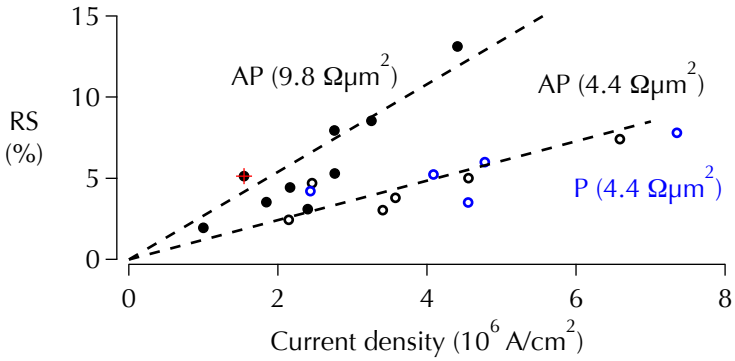

Figure 25: Evaluation of the RS ratio for two sets of samples. The fitting results using eq. 12 and eq. 13 are summarized. The RS ratio is higher for the higher resistive set of samples. For the lower resistive set the magnetization state has no impact on the RS ratio.

The second parameter in equation 12 is the decay time τ. The dependence of τ on the RA product is shown in figure 26 for different stressing voltages. The τ-values are presented both, as numbers in seconds and color coded. The data is quite noisy, nevertheless, a general tendency can be identified. For increasing voltage a decrease in τ is observed. At the same time, for a given voltage, τ decreases with reduced RA-value. The fastest switching of $\tau = 0.2\,s$ was measured at RA of $7.6\,\Omega\mu m^2$ and at a bias of 500 mV. This is too slow for applications in standard digital elec-

tronics. On the other hand, the time resolution of the available setup is in the range of 100 ms. Measurements with increased time resolution might reveal a much faster switching.

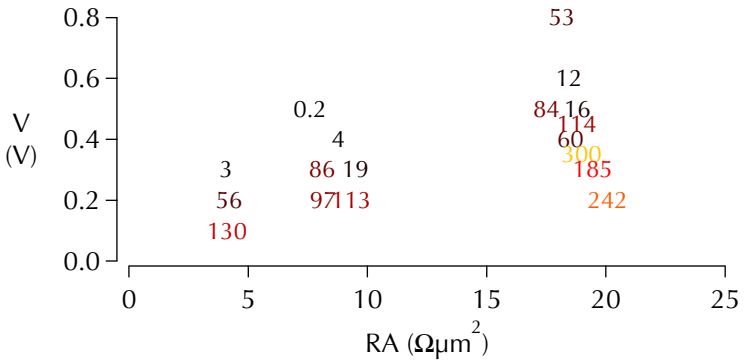

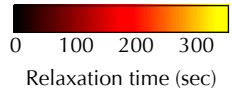

Figure 26: Evaluation of the decay time for two sets of samples. τ-values are obtained from the fitting by eq. 12 and indicated by both, the labels and the color scale (shown above). For increasing voltage a decrease in τ is observed. At the same time, for a given voltage, τ decreases with reduced RA-value.

Constant negative stress

The situation is different for negative stress. Although we can use equation 12 to fit the curves stressed by negative bias if we add a second exponential term

$$R(t) = R_{\text{sat}} - \Delta R_1 \exp(-t/\tau_1) + \Delta R_2 \exp(-t/\tau_2)\,, \qquad (14)$$

an evaluation as for positive stress is not possible. The form of the curve does not seem to be determined by the stress voltage, at least not in the pristine state. Elements carefully fabricated to be as similar as possible behave quite differently under negative stress. The typical nonmonotonic curve progression can always be observed, however, the balance between the increasing and decreasing part is not reproducible.

All curves shown in figure 27 are measured at a constant bias of -560 mV. The top curve exhibits the fastest and the highest resistance increase. The middle curve is flatter, the resistance increase is slower and the difference between R_0 and R_{max} is smaller. The bottom curve is even flatter. The saturation resistance of the top curve is reached after approximately 3 min at a slightly higher level than R_0. For the middle curve no saturation was observed within the time period covered by the measurement. The saturation resistance would be *below* R_0. This means that the final result of this stressing would be a reduced resistance (as it is always for positive bias). For the lowest curve the saturation resistance is

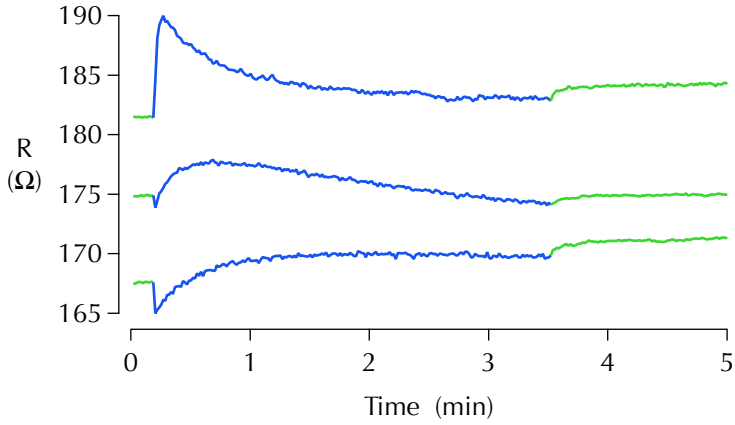

Figure 27: Non reproducible behavior of pristine elements stressed by a constant negative bias.

so close to R_{max} that the curve is almost monotonic. Besides the initial resistance increase and subsequent decrease, an additional feature can be observed. Immediately after applying the stress voltage, a negative resistance jump is observed. This jump seems to be correlated with the flatness of the curve.

The fact that a higher reproducibility is obtained for positive stress, points to the presence of some kind of formation process (at the positive bias). Once the positive stress was performed, a reproducible switching for both polarities is observed as described in the first chapter.

The jumps observed immediately after the stress voltage is applied could be due to frustrated ions present only in the pristine state. They cold be removed from these sites on a much shorter time scale as for the drift-related motion. This would lead to a third exponential term in equation 14 with a negative ΔR and a very small τ. Looking back to figure 23 all processes with negative ΔR at negative bias might be hidden in the monotonically decreasing curve if their sign is reversed with reversed stress polarity—three exponential decreases would lie on top of each other:

$$R(t) = R_{sat} + \Delta R_1 \exp(-\frac{t}{\tau_1}) \pm \Delta R_2 \exp(-\frac{t}{\tau_2}) + \Delta R_3 \exp(-\frac{t}{\tau_3}) .$$

In fact, with an additional term a better fit to the data of figure 23 can be obtained (solid line in fig. 28). In this case, however, the fit parameters are strongly correlated and cannot be used for a quantitative analysis.

The existence of R_{max} means that the elements can be 'overstressed.' To obtain the highest possible RS ratio the negative bias has to be released when R_{max} is reached. The RS ratio is reduced if the stress voltage is applied for too long or if it is too high.

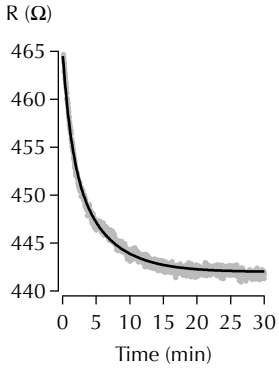

Figure 28: (cf. fig. 23) Resistance decrease fitted by $R_{sat} + \Delta R_1 \exp(-t/\tau_1) + \Delta R_2 \exp(-t/\tau_2)$.

This phenomenon is addressed in the next subsection where the response to alternating stress is discussed.

Resistive loops

In this subsection we return to sinusoidal bipolar input voltage of the form $v(t) = v_{\max} \sin(\omega t)$. The evolution of $R(t)$-, $R(v)$-, and $R(\phi)$-curves shall be discussed. The according measurements are presented in figure 29.

The memristive data is presented as resistive loops as introduced on page 26. On the left side of figure 29 the evolution of a $R(v)$-curve for increasing $v_{\max}$ is shown. The sweep direction

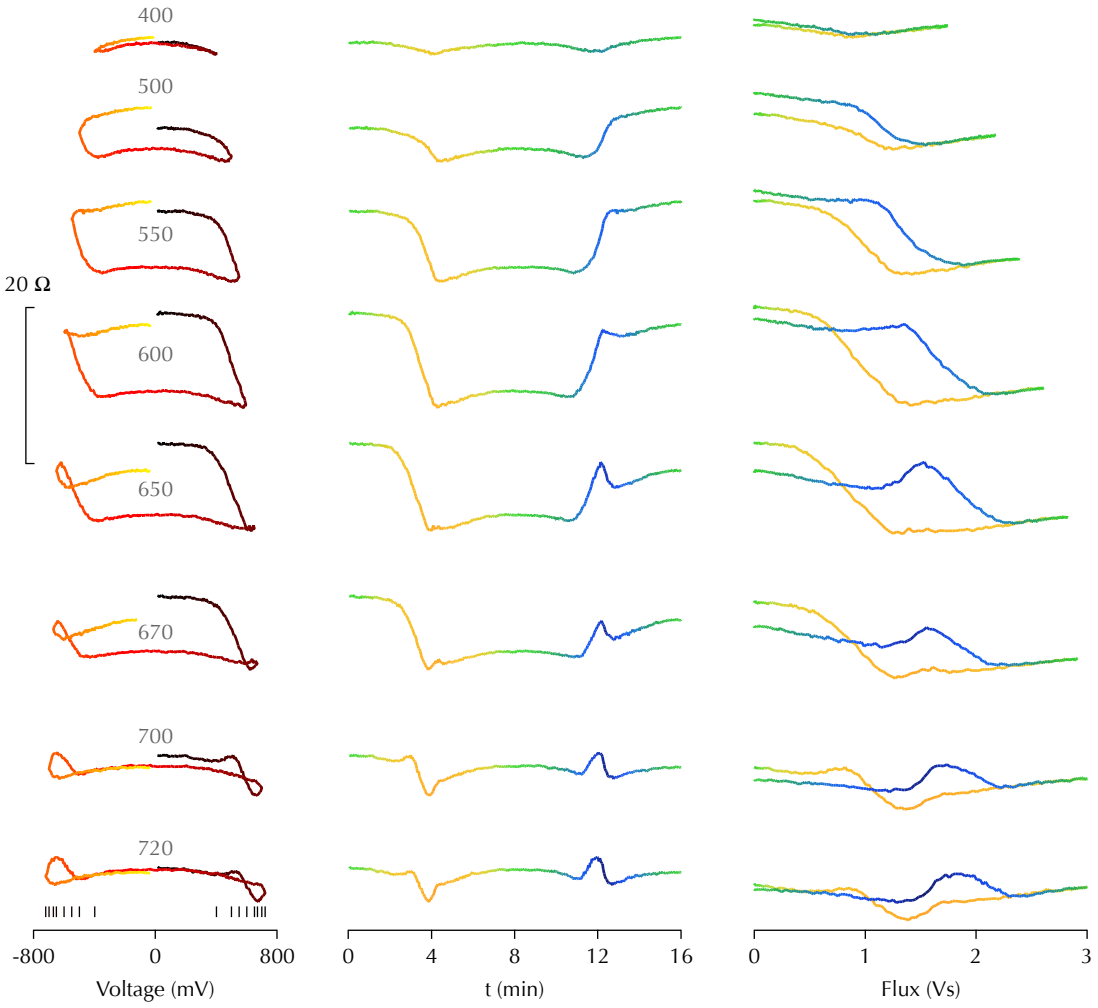

Figure 29: The evolution of a resistance curve for increasing $v_{\max}$. The curves are offset for clarity. The according $v_{\max}$-value is given by a label for each row. For each $v_{\max}$ a single loop is measured.

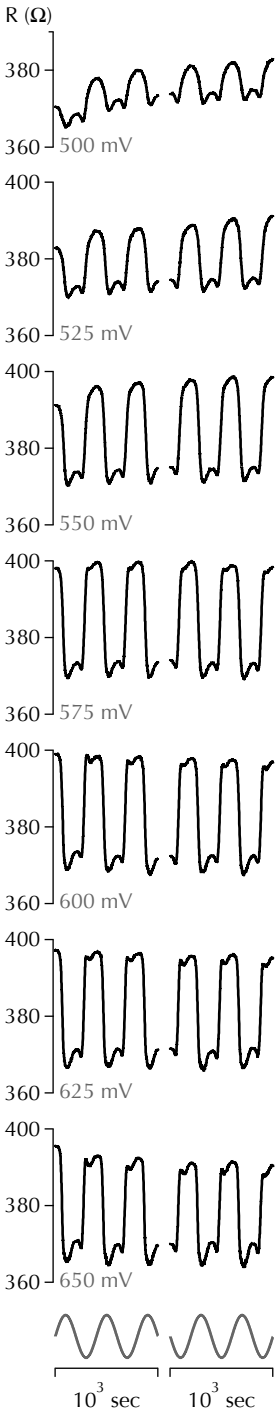

Figure 30: Evolution of a resistance curve for increasing v_{max}. Five loops (10 switchings) are measured for each v_{max}.

is indicated by the color; the measurements begin with black and end with yellow. v_{max} is given by the label (in volt) and by additional ticks close to the abscissa. For the lowest v_{max} of 400 mV no RS can be observed. If v_{max} is increased to 500 mV the loop opens up. The shape familiar from figure 12 is reached at 550 mV. The nonmonotonic behavior of $R(v)$ for negative bias comes into play at 600 mV and becomes obvious at 650 mV. Here an additional (minor) loop opens up for negative bias. Strikingly, a second minor loop opens up at the positive side if v_{max} is further increased. Finally, at $v_{max} = 720$ mV, the major loop collapses completely ($R_H = R_L$) and only the minor loops exist.

The same data is presented unfurled as $R(t)$ in the middle row of figure 29. The trace color indicates the applied voltage. Looking at the data shown in blue (negative bias) the nonmonotonic nature of $R(t)$ is manifested by the peak emerging at 600 mV. While this peak becomes more and more distinct an additional negative peak appears in the region presented in orange (positive bias) for 700 mV.

The $R(\phi)$-curve for the lowest v_{max} is similar to the curve presented in figure 13. Only the thermoresistive effect is present. For increasing v_{max} the curve becomes more and more hysteretic. The curves are not connected to form a continuous loop because, for a particular v_{max}, only a single loop is measured—for the next loop v_{max} is already higher. The gap disappears if multiple loops are measured at a constant v_{max} (cf. fig. 12). This kind of nonrepetitive effects naturally appear in memristive systems as will be discussed below.

The impact of the electric field

Memristive MTJs allow to investigate fundamental properties of memristors. Due to the spin-dependent transport it is possible to push different currents through the device at the same bias. All barrier properties are the same in the P and AP state. This allows to study the role of electric field as the driving force for memristive functionality.

To measure the impact of the electric field on the RS ratio the device is switched between HRS and LRS by a certain input voltage. If the RS is mainly due to the electric field present within the barrier, there should be no difference whether the bias is applied to a sample in the P or AP state.

There are two parameters we want to vary during the write process (magnetic state and voltage) and one during read-out (mag-

netic state). This gives two possibilities: First, stay in a magnetic configuration and increase $v_{\max}$ stepwise in some range. A following sweep of $v_{\max}$ in the opposite magnetic configuration would complete the measurement. In the second scenario one would first stress the sample in both magnetic configurations and subsequently increase $v_{\max}$ by one step. For both kinds of measurement one has to keep the memristive nature of the device in mind. Any previous measurement may still be in the 'memory' of the device.

Figure 30 shows how the problem is treated for the case where the sample is kept in a constant magnetic configuration and the input voltage is swept. In order to stabilize the system for a certain input voltage the system is switched 10 times at constant $v_{\max}$. The values of $v_{\max}$ are given as grey labels attached to each $R(t)$-curve; an typical $v(t)$-signal is shown at the bottom of figure 30. After 5 switch procedures the measurement is interrupted to measure a magnetic loop (indicated by the small gap in fig. 30). The system is in the LRS at this point since the previous half-wave was positive. Again, the sample is switched 5 times—the system is in the HRS now—and a second magnetic loop is obtained. This procedure is repeated 7 times for $v_{\max}$ values between 500 mV and 650 mV. Initially, the progression in figure 30 reveals an increasing amplitude of the $R(t)$-signal. At $v_{max} = 575$ mV a kink appears close to each maximum of the curve—it results from the nonmonotonic switching at negative bias. From now on, the kink becomes more and more pronounced and the amplitude of the $R(t)$-curve decreases.

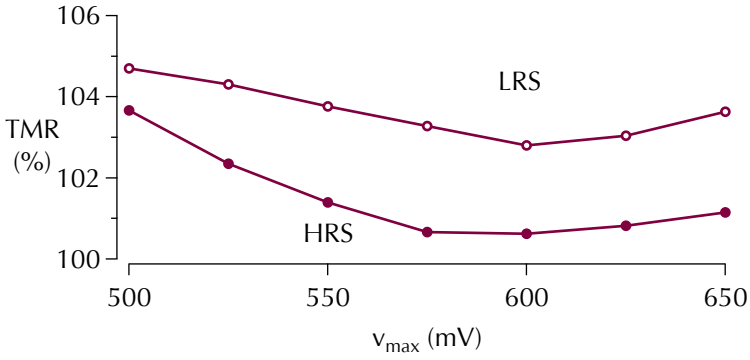

Figure 31: Proof of stable barrier quality throughout the 70 switching operations presented in fig. 30. The evolution of the TMR ratio for the LRS and the HRS shows only a weak dependence on $v_{\max}$.

The data collected from magnetic loops taken every 1000 sec (or 16 2/3 min) can be evaluated as follows. For each $v_{\max}$ we get two loops—one in LRS an one in HRS. From each loop the according TMR ratio is obtained as shown in figure 31. There is only a weak dependence of the TMR ratio on $v_{\max}$. The TMR at

LRS is reduced from 104.7 % to 103.8 % and rises again. At HRS a somewhat deeper minimum is observed whit the TMR reduced by 3 percentage points. A stable TMR ratio is a proof of stable barrier quality throughout the experiment (70 switch operations).

On the other hand, one could exploit this variability for the preparation of arrays of TMR elements with exactly the same TMR ratio. This can never be achieved just by a careful preparation process. A small mismatch, however, can be fixed by memristive means. Each element's TMR ratio can be tuned in the region enclosed by the curves in figure 31. Such a procedure could be advantageous, for example, in the preparation of magnetic logic devices.[64]

[64] G. Reiss et al., Appl. Phys. Lett. **88**, 043505 (2006)

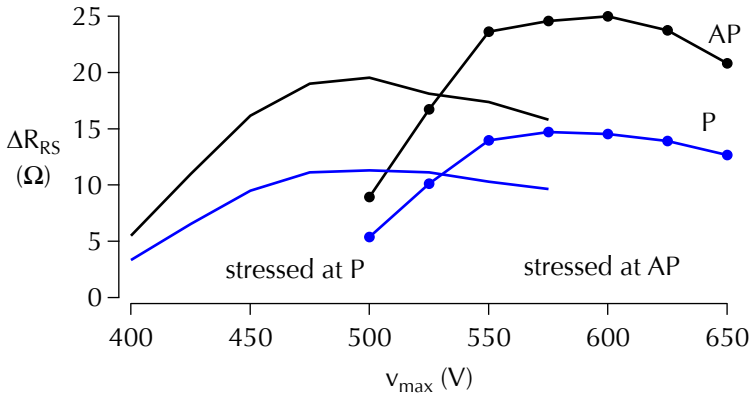

Figure 32: The impact of the electric field on the RS ratio. Stressing in the AP state is compared to stressing in the P state. The results from two similar TMR elements are evaluated.

The RS ratio can be calculated from the shift between two subsequent magnetic loops. The according results are shown in figure 32 by blue (P) and black (AP) bullets. The ΔR_{RS} in the P state is up to 70 % higher than in the AP state. The maximum is reached at 575 mV for the P state (14.7 Ω) and at 600 mV for the AP state (25 Ω).

The question is now, what is the evolution of the RS ratio as a function of v_{max} if the sample is stressed in the P state. Since the element used so far may suffered from the prolonged stressing we take a fresh element and repeat the procedure in the P state. The according data is presented in figure 32 by lines without bullets. Here, a similar curve progression is observed as for the element stressed in the AP state. The difference is a shift to lower voltages and lower RS values. An uncertainty remains because the data is obtained from different elements in this scenario.

To ACQUIRE DATA on a single element the second scenario is adopted. Again, the resistance is switched in succession by si-

nusoidal half-waves with the amplitude v_{max}. In figure 33 the HRS is presented by bullets and the LRS by circles for both magnetic states—AP shown in black and P shown in blue. According to v_{max} the graph is divided in three parts: 500 mV, 550 mV, and 600 mV. Each part is subdivided corresponding to the magnetic configuration established *during stressing*—this is indicated by the gray background. Whenever the data is presented on gray background the bias was applied in the AP state, otherwise in the P state.

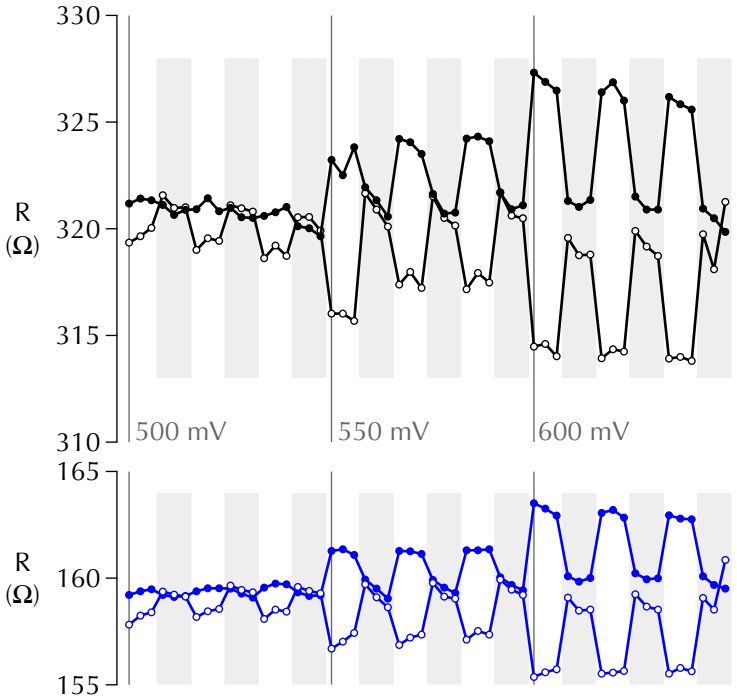

Figure 33: The impact of the electric field on the RS ratio. Stressing in the AP state is and in the P state is performed on the same TMR element. HRS is presented by bullets, LRS is presented by circles. The resistance of the AP state is shown in black, the resistance of the P state is shown in blue. The magnetic configuration *during* the stressing is alternated as indicted by the gray background. The graph is divided into three parts according to the value of v_{max} as indicated by the labels.

The RS ratio in figure 33 is represented by the vertical distance between values displayed by bullets and circles. One can observe a higher ΔR_{RS} during stressing in P state for all three voltages. Actually, a clear ΔR_{RS} for stressing in the AP state appears not before a v_{max} of 600 mV is applied.

FOR BOTH SCENARIOS, RS clearly depends on the magnetic state at which the voltage is applied. In figure 32 the curves stressed at P are shifted by 100 mV to lower v_{max} with respect to the curves stressed at AP. The most likely reason for this shift is the temperature dependence of the ion mobility—the superimposed action of current (Joule heating) and voltage (electric field within the bar-

rier) determines the RS ratio. Consider an one-dimensional model in which a vacancy migrating in a crystal lattice does so by a series of jumps from one position to the next over a potential barrier. It can be shown that the probability per unit time for a vacancy to make the transition to a neighboring equilibrium position is given by

$$w = \nu_0 \exp(-\Delta g/kT)\,, \tag{15}$$

where ν_0 is a frequency which is interpreted as the vibration frequency of the ions surrounding the vacancy, and Δg is the Gibbs free energy of activation.[65] We assume the case of an anion vacancy with the effective charge $+q$ jumping over a distance a from one equilibrium position to another. The effect of an applied electric field E is to add a term qEa to the potential energy. A jump in the direction of the field takes place with increased probability

$$w' = \nu_0 \exp(-(\Delta g - qEa)/kT)\,. \tag{16}$$

The mean drift velocity is therefore given by both, the electric field E and the local temperature T.

The simultaneous effect of heat and electric field is hindering the creation of a simple picture of RS ratio. However, we want to summarize the results obtained so far. First, we compare figure 34 with figure 35. The data presented by black bullets is obtained from stacks with equal RA product. In the former graph we mark the highest RS of 6.8 % at 600 mV by dotted lines. In the latter graph this voltage corresponds to a current density of $3 \times 10^6 \mathrm{A/cm^2}$ and results in a ΔR_{RS} of 8.1 %, again indicated by dotted lines. This agreement is quite surprising if one has in mind the different measurement procedures. While the data presented in figure 34 gives the difference between HRS and LRS, figure 35 gives the difference between R_0 and R_{sat}. Additionally, in the first case a sinusoidal half-wave with an amplitude of 600 mV and 3.3 min duration is applied. In the second case a constant bias of 600 mV is applied for 30 min.

The importance of the measurement procedure can be further emphasized. From the less resistive data in figure 33 (compare blue and black circles) one can conclude that the change in magnetic configuration has no impact on the RS ratio (cf. page 38). By contrast, the effect of Joule heating is particularly prominent in figure 33. Here, the separation of HRS and LRS (bullets and circles) is clearly dependent on the magnetic configuration during stressing. Whereas LRS and HRS are separated at all times when stressed in the P state, an incipient splitting can be observed at 550 mV and

[65] J. J. O'Dwyer, *The theory of electrical conduction and breakdown in solid dielectrics*, Clarendon press, Oxford (1973)

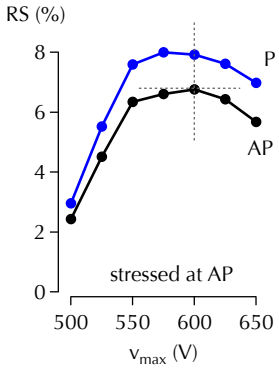

Figure 34: (cf. fig. 32)
The RS ratio obtained by stressing with a fixed magnetic configuration.

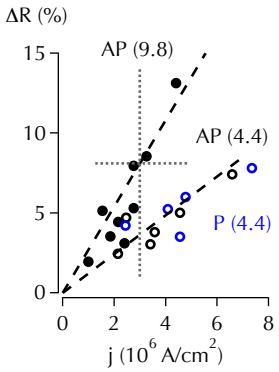

Figure 35: (cf. fig. 25)
Relative resistance decrease obtained by constant stress applied to pristine TMR elements.

becomes measurable not before 600 mV when stressed in the AP state.

Relaxation

From the perspective of potential applications, the stability of resistive switches is one of the main issues. In addition, the nature of relaxation of the switched states should also shed some light on the nature of the process itself.

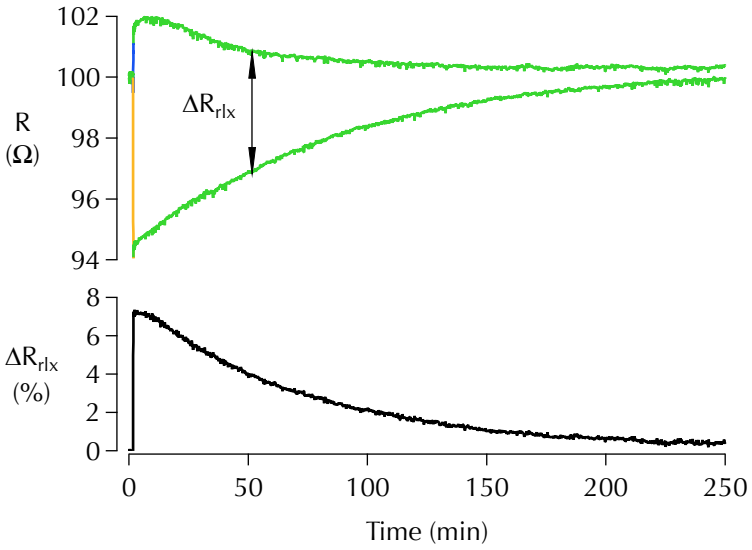

Figure 36: Long-term relaxation of the HRS and the LRS. (top) The curves are measured from two different TMR elements. Both have a resistance of about 100 Ω at t = 0 min. At t = 1.7 min a constant voltage of +450 mV is applied to one element and a voltage of −450 mV to the other (note the color of the trace). The evolution of the induced LRS and HRS is shown in green. The separation of the LRS and the HRS is indicated by the arrows. (bottom) The relative separation of the HRS and the LRS.

In this subsection the stability of R_H and R_L are discussed. A typical measurement is shown in figure 36 on a long timescale and in figure 37 on a shorter timescale. Two subsequent measurements of the same TMR element are plotted. The premeasurement shows a stable resistance close to 100 Ω for both cases. After approximately 1.7 min the samples are stressed by a constant voltage of 450 mV for 10 sec. As expected, the negative bias leads to resistance increase and vice versa. After stressing, R_H and R_L are monitored; both stay fairly constant on the time scale of few minutes. Unfortunately, a strong relaxation process is revealed on a longer time scale ($\sim$ 4 h). The retention time of the information written by the stressing is given by the bottom graph in figure 36. The value ΔR_{rlx} gives the difference between R_L and R_H. Approximately after one hour ΔR_{rlx} is reduced from 8 % to 4 %. After 4 hours ΔR_{rlx} is almost vanished. The memristor 'forgets' its information.

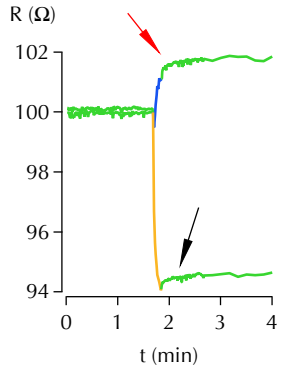

Figure 37: Short-term relaxation of the HRS and the LRS. The small resistance increase after the stress voltage is released (indicated by arrows) is due to the local Joule heat conducted away from the TMR element.

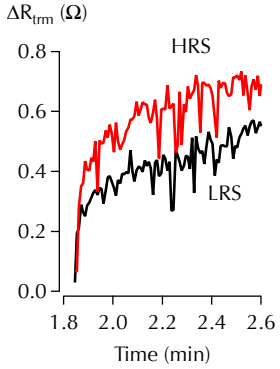

Figure 38: The curve sections indicated by arrows in fig. 37. The resistance immediately after the release of stress voltage is set to zero.

Whenever relaxation measurements are performed a sharp but small resistance increase is observed immediately after the release of stress voltage (cf. fig. 21 and fig. 27). To get a closer look on this features indicated by arrows, the time scale in figure 38 is further reduced. If we define the moment when the stress was released as t' the early stage of the relaxation process can be expressed by $\Delta R_{\mathrm{trm}}(t) = R(t) - R(t')$. Figure 38 shows ΔR_{trm} for both, the HRS and the LRS.

During the discussion of $R(\phi)$-curves on page 27 it was argued that a thermoresistive effect is active when bias approaches zero. This hypothesis is supported by the data presented in figure 38. The sharp resistance increase (never a decrease!) is of the same shape for the LRS and the HRS. This is what one expects if the tunneling current decays while the locally heated sample is approaching thermal equilibrium.

Models for the resistive switching of MTJs

To explain bipolar resistive switching an asymmetry within the system is required. There must be a 'top' and a 'bottom' so that the current direction can be defined unambiguously. For MTJs, this symmetry break is induced by the sputter process. The bottom interface of the MIM system is fabricated by sputter deposition of MgO on top of Co-Fe-B. During this step of preparation, oxygen is released from the MgO target to the sputter chamber and can react with the metals of the bottom electrode. The top interface, on the other hand, is fabricated by deposition of Co-Fe-B on top of an MgO layer. Here, the oxygen is embedded within the MgO lattice and will not react as easily with the metals of the top electrode (cf. page 27).

In the simplest case, just one of the interfaces is responsible for resistive switching. We proceed with the discussion of two models, pointing to different interfaces as being active. Regardless of interface activity, a proper model needs to cover the three main aspects: (i) bipolar resistive switching without forming; (ii) nonmonotonic $R(t)$-curves, never observed at positive bias in the pristine state; and (iii) slow relaxation when the stress voltage is released.

A SIMPLE MODEL for resistive switching in tunnel systems was proposed by Meyer et al.[66] Based on this model, it is assumed that the migration of oxygen ions from the electrode into the bar-

[66] R. Meyer et al., IEEE Symposium on Non-Volatile Memory Technology 2008 , 1 (2008)

rier leads to accumulation of charge. As a consequence, electrons tunneling across the MgO are repelled by the negative charge; the effective barrier height is increased. If we consider the stoichiometric case as equilibrium barrier geometry (top drawing in fig. 39), the barrier height is increased if the stoichiometry imbalance is due to additional O^{2-} ions (middle drawing in fig. 39). Resistance increase is observed when positive bias is applied to the top electrode. Consequently, we identify the top electrode as the source of O^{2-} ions and the top interface as the active one. For reversed bias polarity the oxygen ions are extracted from the barrier back to the top electrode; the barrier height is reduced.

The strong point of this model is a natural explanation of the relaxation process. It would be the manifestation of the oxygen diffusing back to stoichiometric sites. It is flawed, however, by the lack of explanation for the nonmonotonic $R(t)$-curve at negative bias.

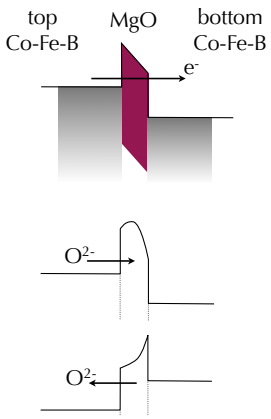

Figure 39: Resistive switching by charge accumulation within the barrier. The effective tunnel barrier is increased (for electrons) if negative charge is accumulated. The barrier is decreased when negatively charged ions diffuse out of the barrier.

[67] M. J. Rozenberg et al., Phys. Rev. B **81**, 115101 (2010)

A MODEL by Rozenberg et al.[67] is particularly interesting for the discussion of nonmonotonic $R(t)$-curves. We shall begin with a summary of the main idea. It is assumed that the electric transport is dominated by a single conductive path embedded within a more insulating host. The conductive path is represented by an one-dimensional resistive network of N links. The local resistivity ρ along this path is assumed to be controlled by the oxygen vacancy concentration δ. The simplest linear relation $\rho = A\delta$ is adopted. The key role played by the interfaces is incorporated by the designation of three regions: two *interfacial regions* and one *bulk region*. Each link i is characterized by a certain concentration of oxygen vacancies, which determines the resistivity of the link:

$$R(t) \propto \sum_{i=1}^{N} \rho_i(t) = \sum_{\alpha} \sum_{i \in \alpha} A_\alpha \rho_i(t)\,, \tag{17}$$

where α denotes one of the three regions. The local voltage is calculated according to

$$v_i(t) = \rho_i i(t)\,. \tag{18}$$

The vacancy transfers between two neighbor domains a and b are computed from

$$p_{ab} = \delta_a(1-\delta_b)\exp(-v_0 + \Delta v_a) \tag{19}$$

$$\Delta v_a(t) = v_b(t) - v_a(t) \tag{20}$$

and used to update the values $\rho_a(t)$ to a new set of concentrations $\rho_a(t+1)$. Here, p_{ab} gives the transfer probability from domain a

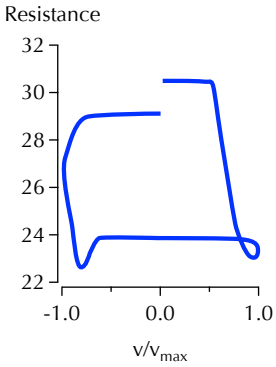

Figure 40: The occurrence of minor loops for calculated resistive loops. The asymmetric case $A_T = 1000$, $A_B = 25$ is shown. Reproduced from Rozenberg et al., Phys. Rev. B, **81**, 115101 (2010)

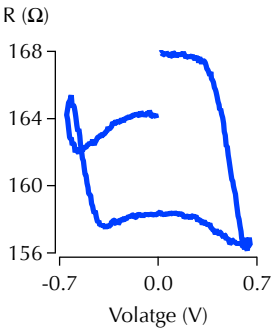

Figure 41: (cf. fig. 29) The occurrence of minor loops observed experimentally for memristive MTJs.

[68] H. Meyerheim et al., Phys. Rev. B **65**, 144433 (2002); X. Zhang et al., Phys. Rev. B **68**, 092402 (2003); and J. C. Read et al., Appl. Phys. Lett. **90**, 132503 (2007)

to domain b. The factor $\exp(\Delta v_a)$ models the enhancement of the diffusive process due to the local electric field at domain a. The dimensionless constant v_0 is related to the activation energy for vacancy diffusion. Additionally, the transfer probability is proportional to the concentration of vacancies present in the source domain and to the concentration of free vacancy sites at the target domain.

The calculations performed by Rozenberg et al. allow to track the positions of vacancies during applied voltage protocol. Under the action of repetitive voltage cycling, the initially uniform distribution of oxygen vacancy concentration, evolve toward a new stable distribution. Results particularly important for the present thesis are obtained when the factors controlling the resistivity of the interfacial regions are set to $A_{\text{top}} = 1000$ and $A_{\text{bottom}} = 25$ and the resistivity of the bulk region is set to unity. In this case (asymmetric interfaces), the curve presented in figure 40 is obtained. The data is in good qualitative agreement with our measurements (see fig. 41). The second result important for the present thesis is that a hysteresis loop with a stable shape is not established until few initial cycles (showing nonrepetitive effects) are performed.

To adopt the model of Rozenberg et al. for memristive MTJs we consider the simplified stack pictured in figure 42. It is generally believed that oxygen liberated from the MgO target in the early stage of sputtering is captured by the iron,[68] and we shall assume this to be true for the purpose of the discussion. The oxygen transferred from MgO to Fe leads to a *degeneration* of the interface to a FeO/Mg/MgO system. The connection to the model by Rozenberg et al. is given if we identify the oxides as the interfacial regions and the Mg layer as the bulk region. It should be stated here that for a 'layer' an extremely thin layer in the range of few monolayers or even a sub-monolayer might be a realistic picture.

At positive bias the drift-direction of negatively charged oxygen ions is from bottom to top. The experimentally observed resistance decrease in this case, can be explained by interface *regeneration*. The ions captured by Fe are retrieved to the Mg layer turning it back to MgO. This would increase the quality of the interface and lead to higher conductivity. Moreover, due to the strong impact of the barrier quality on the spin-dependent tunneling, one can expect the regeneration to be in favor of the AP state, as indeed observed (see fig. 32).

At negative bias, the drift direction is reversed supporting/ strengthening the tunnel interface damage. As a result the re-

sistance is raised. On a characteristic time scale, the reservoir of loosely bound oxygen ions will be depleted and the damage process will saturate. The drift of ions is not necessary stopped at this stage. Further migration of O^{2-} will bury the FeO layer deeper within Fe bulk if there is no support of oxygen from the above layers. In other words, the oxygen is removed from the interfacial Fe and dragged deeper into the bottom electrode. The resistance decrease observed at this stage is due to a gradually re-established Fe surface.

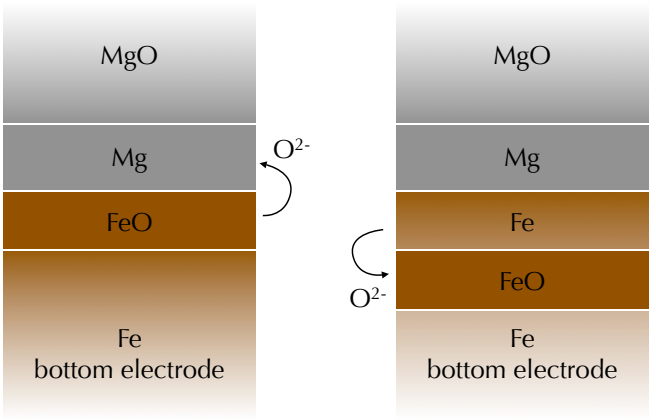

Figure 42: Resistive switching by interface degeneration/regeneration. Induced by the sputter process the ideal Fe/MgO bottom interface degenerates to a Fe/FeO/Mg/MgO. (left) By application of positive bias oxygen ions are moved from the FeO layer to the Mg layer; the ideal interfaces are re-established. (right) At negative bias the oxygen ions are moved in the opposite direction supporting the sputter-induced degeneration. Prolonged stressing at negative bias might burry the O-ions deeper into the Fe layer leading to an increased interface quality again.

Numerous publications point to the preeminent role of the interfaces (between electrodes and the barrier) for the TMR effect. For the simple Fe/MgO/Fe system several experimental[69] as well as theoretical[70] investigations have demonstrated systematic dependence of the spin polarization on the amount of oxygen atoms at the interface. For the pinned Co-Fe-B electrodes as used in this work, the situation is more complex. The presence of highly diffusive Mn in the antiferromagnetic layer is one important factor. Also the diffusion of B during the crystallization (annealing) of Co-Fe-B electrodes is still under debate. Some researches report an accumulation of B within Ta layers[71]. Others observe a B diffusion to the MgO layer[72]. Both cases might coexist with stronger manifestation depending on the annealing temperature. In the latter case again a degeneration of the bottom interface to a Co-Fe/Mg-B-O/MgO system allows to apply the degeneration/regeneration model.

[69] G. Miao et al., Phys. Rev. Lett. **100**, 246803 (2008); and M. Müller et al., Europhys. Lett. **80**, 17007 (2007)

[70] C. Heiliger et al., Phys. Rev. B **72**, 180406 (2005); and X. Zhang et al., Phys. Rev. B **68**, 092402 (2003)

[71] S. Karthik et al., J. Appl. Phys. **106**, 023920 (2009)

[72] J. C. Read et al., Appl. Phys. Lett. **90**, 132503 (2007); J. Cha et al., Appl. Phys. Lett. **91**, 062516 (2007); and J. Cha et al., Appl. Phys. Lett. **95**, 032506 (2009)

Artificial synapses & neurons

The human brain is always compared with the most advanced technology of the day. René Descartes was inspired by the fountains at Versailles to write about the brain in terms of hydraulics.[73] Later the brain was compared to telephone switchboards and, today, to the digital computer.[74] Nevertheless, the last analogy holds quite well if one defines computation as: selecting the next state and present output based on the current state and applied input.

Synapses and neurons are the diodes and transistors of the brain. In this chapter some of the fundamental characteristics of biological synapses and neurons as well as their interplay are introduced. On this basis, we will present remarkable similarities between synapses and memristive MTJs and discuss possible applications thereof.

[73] C. Koch, *Biophysics of computation*, Oxford university press (1999)

[74] Die Gefahr, dass der Computer so wird wie der Mensch, ist nicht so groß wie die Gefahr, dass der Mensch so wird wie der Computer.

Konrad Zuse (2005)

Neural networks

In electronics a potential difference is created between two terminals of a circuit causing the current to flow along the wires. In neurons the potential difference is build up across a 0.4 nm thick lipid membrane separating the inside from the outside of the cell[75]. If the cell is inactive, this potential is balanced at typically $-70\,\mathrm{mV}$, the *resting potential*. This potential is due to an electrochemical dynamical equilibrium of in-flow and out-flow of ions, most importantly Cl^-, Na^+ and K^+. The flow of ions is mediated by transmembrane proteins called ionic channels. Ions that enter or leave a neuron through an open channel do so passively. To maintain a constant resting potential an additional active transport mechanisms is necessary that use energy to move ions back across the membrane and against their electrochemical gradients. This transport mechanism is driven by the hydrolysis of ATP. The responsible enzyme carries three Na^+ ions out of the cell and two K^+ ions in for every molecule of ATP hydrolyzed.

[75] If not specified otherwise, this section is based on the textbooks: J. G. Nicholls et al., *From neuron to brain*, Sinauer Associates, Inc. (2001); and E. R. Kandel et al., *Neurowissenschaften*, Spektrum Akademischer Verlag (1996)

ATP
Adenosine triphosphate

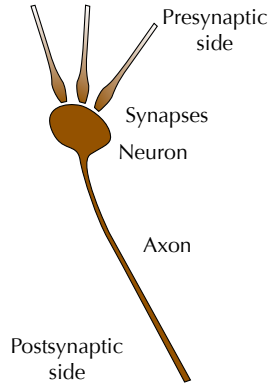

Figure 43: Schematic picture of a synaptic connection. The neuron receives signals from the presynaptic side, processes them, and send the resulting signal to postsynaptic neurons via the axon.

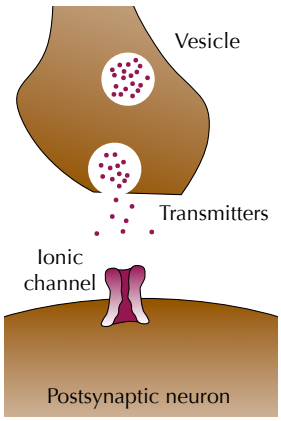

Figure 44: The synapse: the term relates rather to a location than to a piece of tissue. At synapses neurotransmitters are synthesized, stored in synaptic vesicles, and released by exocytosis. Transmitters diffuse across the synaptic cleft (20–40 nm), activate the ionic channels on the postsynaptic side, and are removed by diffusion or degradation.

The transparency of the ionic channels is not fixed. All electrical signals are created by a temporary, local disturbance of the in/out current rates. This disturbance, triggered possibly by a photon at the retina of an eye, propagates from neuron to neuron and may cause a muscle to be contracted. There are two main classes of ionic channels leading to two sorts of signals. First, chemical-activated channels responsible for the generation of *graded potentials*. Graded potentials are localized. Their amplitude depends on the strength of the stimulus and varies from less than one millivolt to 50 mV. Voltage-activated channels constitute the second major category and are responsible for the generation of *action potentials*. Unlike graded potentials, action potentials are fixed in duration (0.5–2 ms), polarity, and amplitude (typically 100 mV). They propagate rapidly over long distances along the *axons*.

Each neuron is connected to a huge number of other neurons via specialized connections, called *synapses*. The synapses are situated close to the membrane, but there is no direct connection. An electric signal propagating through the neural network that arrives at the synapse cannot propagate further directly. It is converted to a chemical signal by emission of neurotransmitters (see fig. 44). The neurotransmitters are released into the synaptic cleft and temporarily change the transparency of the postsynaptic membrane proteins. This gives rise to the disturbance of the resting potential—the charge within the neuron is increased or decreased with respect to the equilibrium state. In this way the chemical information is reconverted to an electrical signal. The efficacy of this process is referred to as the connectivity or the weight of the synaptic connection. Which response will occur, increase or decrease, is not mediated by different kinds of neurotransmitters. It is given, on the presynaptic side, by the efficacy of transmitter release and, at the postsynaptic side, by the number and characteristics of the membrane proteins. These parameters can change according to the activity of the synaptic connection which is known as synaptic plasticity.

The graded potential is performing a random walk according to the kind and strength of the synaptic connection. Due to quite long lifetimes, ranging from milliseconds to several minutes, and the localized nature of graded potentials, the neuron is capable of temporal summation of the incoming signals. The graded potential is an analog signal because a continuous range of values is used to represent information. If the potential reaches a certain threshold, however, the voltage activated channels are triggered

generating an action potential—a short, massive increase of membrane potential. The form of this signal, the so-called spike, is independent of the impulses that led to the overstepping of the threshold. It always consist of a depolarizing phase followed by a repolarizing phase of a fixed shape. It is an all-or-nothing impulse, thus digital in nature.

Spike-timing-dependent plasticity

Repetitive electrical activity can induce a persistent increase or decrease of synaptic efficacy, commonly referred to as LTP and LTD, respectively. This long lasting plasticity is believed to be the basis of learning and memory.

LTP
Long-term potentiation

LTD
Long-term depression

The process is illustrated in figure 45. An action potential generated on the presynaptic side at the time t_0 arrives at the synapse. The transmitters are released in the synaptic cleft, the graded potential pass beyond the threshold and a postsynaptic action potential (spike) is generated promptly at $t_1 \approx t_0$ (fig. 45a). This signal propagates along the axon in the forward direction but it is also transmitted in the reverse direction via all connected synapses (fig. 45b). Messenger-molecules are send back from the postsynaptic side back to the synapse. These messengers are able of increasing the rate of transmitter emission, but only if the emission mechanism is still excited, i.e., if there has been a recent neurotransmitter emission.

Synapses that show this coincidence requirement for its modification are called *Hebbian synapses* after Donald Hebb who proposed the concept of cell assembly as the basis of learning in the cortex. By cell assembly, Hebb imagined a circuit of intercon-

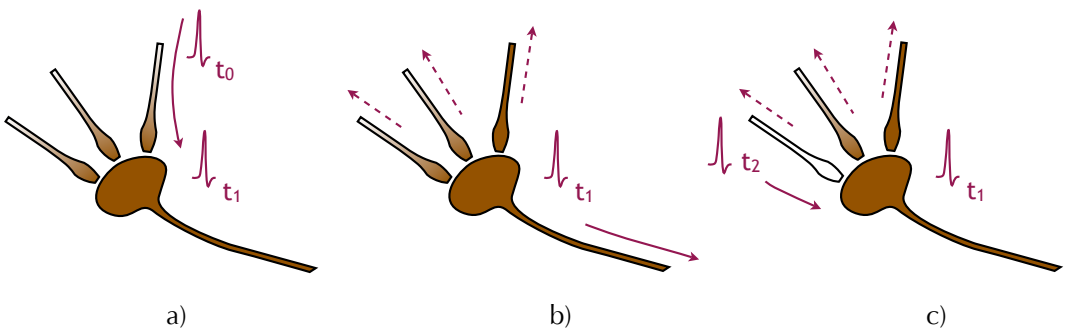

Figure 45: Spike-timing-dependent plasticity. An action potential generated at the presynaptic side arrives at the neuron at the time t_0. (a) When this stimulus causes a depolarizing response that exceeds the threshold, the all-or-nothing action potential (spike) is initiated at t_1. (b) This spike propagates along the axon in the forward direction but it is also acting on the synapses in the reversed direction. For $t_1 > t_0$ the responsible synaptic connection is strengthened. (c) For reversed timing $t_1 < t_2$ the connection is weakened.

nected neurons that is capable of responding to specific external input with a sequence of firing activity. This may ring within the circuit for hundreds of milliseconds and hence constitute a short-term 'memory trace.' Moreover, the activity may induce long-lasting cellular changes within the assembly, which in turn reinforce the specific connections and facilitate re-activation of the previously 'learned' activity pattern. Essentially, what Hebb was postulating is that correlated presynaptic and postsynaptic activity would increase synaptic strengthening. His idea became popularized by the famous mnemonic: 'cells that fire together, wire together.'

In the conventional concept of Hebbian synapses the property of coincidence (firing together) was examined with fairly low temporal resolution. In the past few years, a series of experiments, using techniques that allow for direct activation of temporally correlated presynaptic and postsynaptic action potentials with millisecond precision, have revealed a new picture.[76] These studies suggest that, instead of mere coincidence, the precise timing of presynaptic and postsynaptic action potentials plays a decisive role in determining the type of synaptic modification. We consider figure 45 with a fresh look on the spike timing to clarify the concept of the so-called STDP. The spike induced at the presynaptic side at t_0 triggers a postsynaptic spike at $t_1 > t_0$. This signal back-propagates via all synapses connected in reverse direction. According to the Hebbian rule this correlated activity leads to LTP, indicated by darker color of the according connection in figure 45b. Now we consider a spike created somewhere else in the network appearing at the presynaptic side at $t_2 > t_1$ (figure 45c). A strengthening of the according connection would still be consistent with the simple Hebbian rule if $t_2 \approx t_1$. In STDP, and this is the key point, the reversed timing leads to a weaker connection.

[76] H. Markram et al., Science **275**, 213 (1997); J. Magee et al., Science **275**, 209 (1997); and C. Bell et al., Nature **387**, 278 (1997)

STDP
Sike-timing-dependent plasticity

Figure 46 shows the asymmetric spike-timing window that appears to be typical for most synapses between pyramidal neurons.[77] In cultured hippocampal neurons, the critical spike-timing window where effective synaptic modification occurred was shown to be of about 50 ms.[78] If postsynaptic spiking occurred too early or too late relative to the presynaptic activity, the synapse was not modified. In addition to the conventional interpretation of the Hebbian rule, the asymmetry in the window highlights the significance of temporal order. This temporal asymmetry seems to reflect the causal dependence of the generation of an action

[77] B. Berninger et al., Bioessays **24**, 212 (2002)

[78] G. Bi et al., J. Neurosci. **18**, 10464 (1998)

potential in the postsynaptic cell on prior presynaptic firing. In this context, one can speak of a cellular 'causation detection device.' When a postsynaptic spike occurs after the presynaptic input (positive spike-timing values) it is very likely that this input has contributed to the generation of the spike (causal order). If the activity occurs in the anti-causal order, i.e., postsynaptic spiking precedes the presynaptic input, the synapse will be weakened as shown for negative spike-timing values in figure 46.

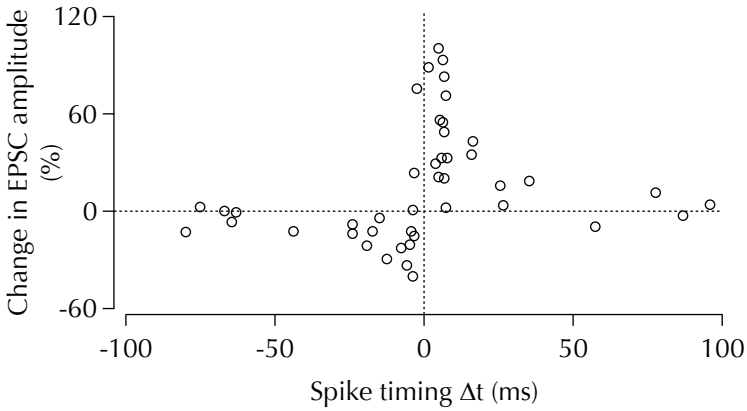

Figure 46: Critical window for the induction of LTP and LTD. The spike timing is defined to be positive for the case: first presynaptic then postsynaptic spike is sensed at the synapse (causal case). The LTP is observed for small (< 25 ms) positive Δt. For reversed spike timing LTD is observed. Reproduced from Bi et al., J. Neurosci., **15**, 10464 (1998)

Synaptic behavior of MTJs

Artificial neural networks are systems that permit computers to function in a manner analogous to that of the human brain. Instead of manipulation of 0s and 1s they create weighted connections (synapses) between switching elements (neurons). This allows for data to be read and stored in ways that resemble human learning and memory. Biologically inspired (neuromorphic) networks have opened up new possibilities to apply computation to areas that were previously thought to be the exclusive domain of human intelligence. Areas that show the greatest promise for neural networks, such as pattern classification tasks or speech and image recognition, are areas where conventional computers and data-processing systems have the greatest difficulties.

Artificial neural networks that are developed today are largely software-based. They are slow because during the learning phase a standard computer must serially calculate connection strengths. When the network gets larger, the computation time becomes enormous. Because software simulations are performed on conventional (sequential) computers they do not take advantage of the inherent parallelism of neural network architectures. To fully

exploit the benefits of artificial neural networks hardware solutions are needed. The problem with pure hardware implementation using CMOS technology as it exists today, are the variable resistors needed for weighted connections (synapses). Whereas the fabrication of artificial neurons is straightforward for digital technology, the analog nature of synapses makes the latter challenging. One solution is the switched capacitor circuit[79] shown in figure 47. It consists of two switches (MOS transistors) with a charge storage capacitor C_1 at the junction of the two switches. The switches are driven by pulses which do not overlap, ensuring that only one switch is on at the time. In operation, the first switch charges C_1 to the potential of terminal A and the second switch transfers a packet of charge from C_1 to terminal B. Because the charge transferred is proportional to the potential difference between A and B, the device works like a resistor whose value is inversely proportional to the frequency of the switching pulses ω.

[79] W. Maass and C. M. Bishop, *Pulsed neural networks*, Chapter 8, MIT press, Cambridge (1999)

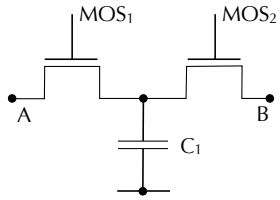

Figure 47: The switched capacitor circuit: an artificial synapse emulated by standard digital technology. The resistivity of this circuit is inversely proportional to the switching-frequency of the MOS transistors.

Besides the complexity of the switched capacitor circuit, the disadvantage of the device is that there is a need of additional circuity to evaluate the activity of the connection and to adjust and store the according ω values. In the following, we demonstrate that memristive MTJs intrinsically exhibit characteristics of both, synapses and neurons. Therefore, they represent the simplest thinkable implementation of neuromorphic hardware.

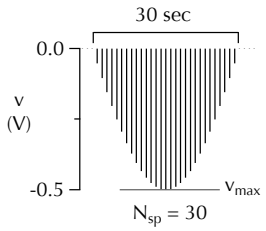

Figure 48: The standard spike train. It consists of a series of one second pulses, enveloped by a sinusoidal half-wave with the amplitude v_{max}. The pulses are separated by 200 ms intervals where the resistance of the memristive MTJ is monitored.

WE BEGIN THE PRESENTATION of experimental results with focus to the synaptic function of memristive MTJs. Basically, the synaptic behavior of MTJs was demonstrated in the previous chapters. The topic of this section is to introduce the experimental technique common in the field of neuroscience and apply it to memristive synapses. In this way a set of data shall be collected which can be used to elaborate the similarities between biological and artificial synapses.

To proof the synaptic functionality requested in neural networks the response of memristors to spikes has to be investigated. For biological neurons different classes of spiking patterns are used for stimulation. Two particularly efficient patterns are termed 'theta-burst stimulation' and 'primed-burst stimulation.'[80] We shall not go into details of these here, except to emphasize that one must resort to more sophisticated formalisms as presented in the second chapter to cover the impact of spiking *pattern* on resistive switching. Thus, in the remainder of this chapter, the voltage protocol used so far remains the same and spike trains as shown

[80] J. Larson et al., Brain Res. **368**, 347 (1986); and G. Rose et al., Neurosci. Lett. **69**, 244 (1986)

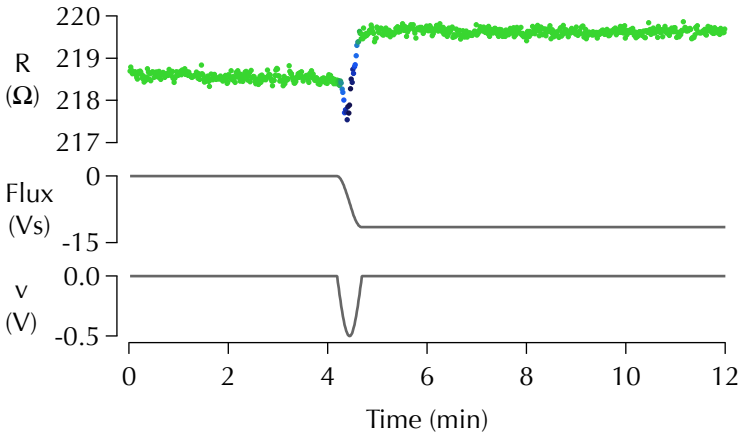

Figure 49: Memristive MTJ activated by a standard spike train of negative polarity. The position of the applied train is shown by the bottom trace. The resulting flux is given by the middle trace, the total flux-contend of the train is −15 Vs. The resistance of the memristive synapse is modulated by the train and remains stable when the activity is terminated.

in figure 48 are applied. They are characterized by only two parameters: the amplitude of the sine profile v_{max} and the number of spikes per train N_{sp}.

A typical measurement is shown in figure 49. The graph consists of three traces. The bottom trace plots the applied voltage. The middle trace displays the corresponding flux. The top trace shows that due to the voltage treatment, the resistance is driven from a lower stable level to a higher stable level. This is exactly how an artificial synapse should respond. The activity at the synaptic connection leads a stable modification thereof—the activity is remembered.

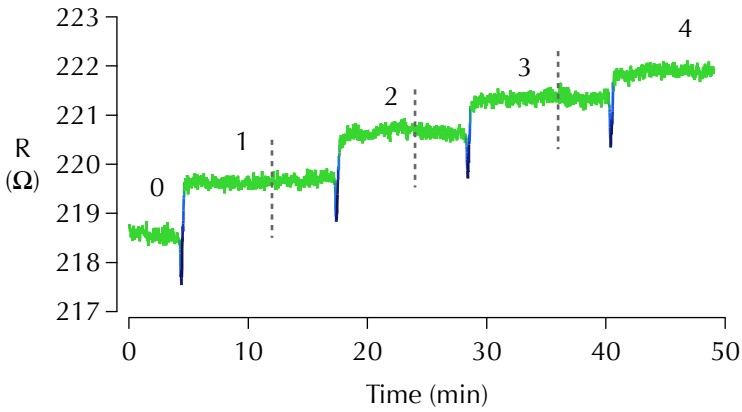

Figure 50: The effect of subsequent train application. The resistive states are numbered. The state zero is the result of the refreshing procedure shown in fig. 51. The other states are induced by standard spike trains.

Figure 50 shows the effect of repeated treatment (4 times) with a 30-spike train and $v_{max} = -500\,\text{mV}$. To control the barrier quality, every 12 minutes (dashed lines) the constant magnetic field is released to measure the magnetic minor loop. If the minor loop shows a TMR ratio close to 100 % the data measured so far is con-

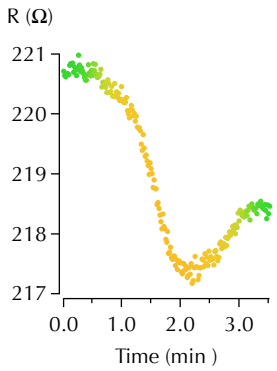

Figure 51: The refreshing procedure. It is identical to a train with the spike number $N_{sp} = 200$. It is applied to prepare a LRS as a starting point for repeated measurements on the same TMR element.

Figure 52: Analysis of subsequent train application for different N_{sp}. The green bars are the result the refreshing procedure. The levels shown in blue are induced by the (negative) trains and numbered as in fig. 50.

sidered as reliable. A stepwise resistance increase is observed. The resistance steps are getting smaller with every spike train. This is in agreement with previous measurements with constant voltage stress. Between spike trains a good stability of the resistive states 1–4 is observed.

Since there is a limited range in which the resistance can be varied, it is important to investigate how many states can be realized within this range. For long spike trains a few well separated states are expected. For shorter spike trains many states with poor separation will be crated. To repeat measurements for different N_{sp} on the same TMR element a refresh-procedure is needed. An obvious attempt is to saturate the memristor at its lowest resistance before a series of spike trains is applied. To do so a sine half-wave of 3.5 min and +500 mV is applied, as pictured in figure 51. This simple procedure sets an LRS which is, in the best case, independent of the previously performed spiking.

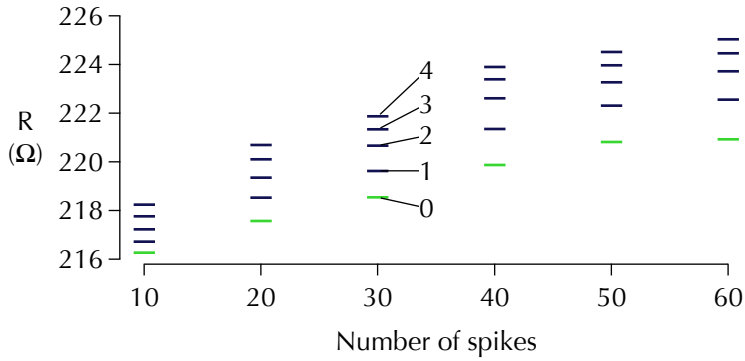

Figure 52 pictures the analysis of curves similar to that in figure 50, where each resistive state is represented by the median of the postmeasurement (green parts of the curve in fig. 50). The results of the refreshing procedure, i.e., the LRS's, are represented by green bars. Every subsequent resistive state is shown by a blue bar located above (cf. labels in fig. 50). For small N_{sp} equidistant resistive states are observed. For increasing N_{sp} the impact of the first spike train becomes dominating—with every subsequent spike train the step size declines. The growth of LRS with N_{sp} indicates that the reset procedure was not entirely successful.

The application of spike trains with opposite polarity leads to a stepwise decreased resistance, as expected. Again, we keep $v_{max} = +500\,\text{mV}$ at all times, apply four trains with the same

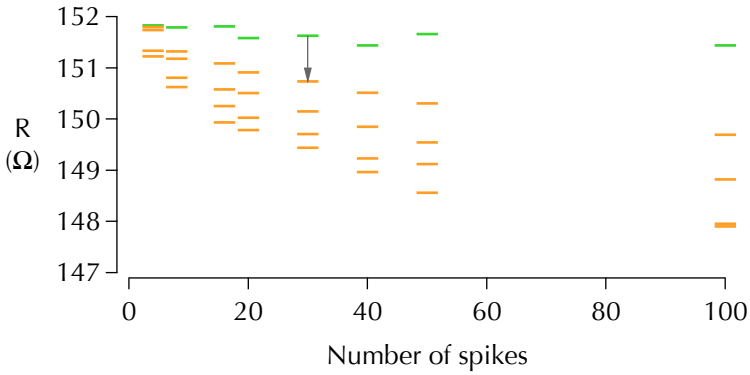

Figure 53: Analysis of subsequent train application for different N_{sp}. The green bars are the result the refreshing procedure. The levels shown in orange are induced by the (positive) trains. The arrow indicates the step shown in fig. 54.

N_{sp}, refresh, and repeat the treatment with increased N_{sp}. The refreshing of HRS is established by a prolonged stressing with positive bias to drive the resistance to the LRS followed by stressing at negative bias to prepare a HRS as a starting point for the next measurements. The results are presented in figure 53. The first step obtained by the refreshing procedure (HRS) is displayed in green. All HRS are localized between 151 Ω and 152 Ω indicating successful refreshing. The distribution of the resistance levels is similar to the case of negative spikes. One observes that the first train is the most effective in terms of resistance decrease, especially for higher N_{sp}. The step indicated by the arrow is displayed as an example in figure 54. Here a step of 0.9 Ω is induced by a train of 30 spikes.

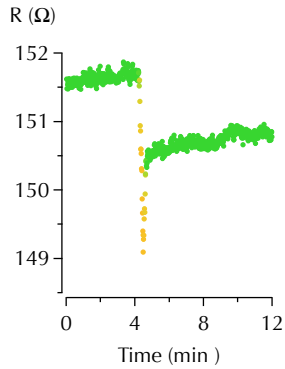

Figure 54: Memristive MTJ activated by a spike train of positive polarity.

For a complete picture of bipolar resistance change driven by spike trains we normalize the refreshed levels to zero. In this way the absolute change in resistance can be displayed as in figure 55. The resistance obtained by negative spikes is shown in blue; levels

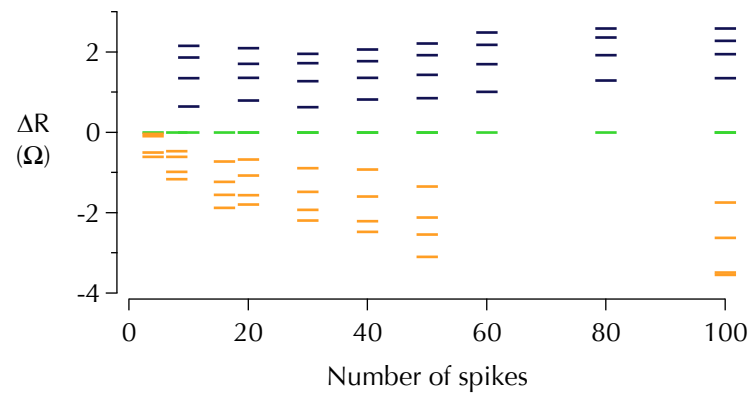

Figure 55: Synaptic activity of a memristive MTJ. The refreshed state is set to zero (green bars). The relative resistance increase is shown in blue and the relative resistance decrease in orange.

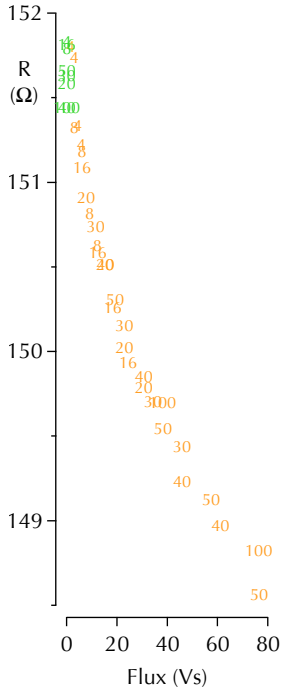

Figure 56: Flux as a well suited variable to describe resistance variation induced by spike trains.

shown in orange are due to positive spikes. All measurements are performed on the same TMR element. A clear asymmetry of both, the maximum resistance change and the dependence of ΔR on the number of spikes, can be observed. The maximum resistance increase is $+2.6\,\Omega$ whereas the maximum resistance decrease is $-3.5\,\Omega$. The increase of the spacing between the resistance levels with rising number of spikes per train is more pronounced for the positive spikes.

We take the resistance levels from figure 53 and calculate the flux of the spike train responsible for the resistance decrease. The resulting graph is shown in figure **??**. The flux of the first train is set to zero. The flux of the subsequent train is added to the previous one. We let the labels indicate N_{sp} so one can see that the same curve is obtained for few huge steps on the flux-axis and many small steps. That indicates that the flux is a 'good' variable to describe spike induced resistance variation.

In general, the experiments show that the repeated treatment with spike trains is capable of gradual resistance-changing of a memristive MTJ. The resistivity (or better the conductivity) is comparable to the strength of a synaptic connection. Due to bipolar resistance change LTP as well as LTD is emulated. The activity-driven modification is stored in a non-volatile fashion.

Memristive synapses

Since LTP has been found in all excitatory pathways in the brain, there is growing evidence that it underlies at least certain forms of memory.[81] It is expressed as a persistent EPSP potentiation recorded from individual cells or from populations of neurons. It can be induced in a number of ways, most conveniently by delivering a train of 50–100 stimuli at 100 Hz or more to the pathway of interest. One method to measure EPSP potentiation is to evaluate the slope of the rising phase of the evoked response[82] (see top of fig. 58 for examples of evoked responses). Bliss and Collingridge recorded LTP in vivo from the hippocampus of a rat and evaluated the slope of the rising EPSP (top graph of fig. 57). The data is normalized to give zero EPSP potentiation before stimulation. At $t = 1\,\text{h}$ a train (200 Hz, 200 ms) is delivered. Thereafter a stable EPSP potentiation of approximately 50 % is observed.

The most intuitive definition of the synaptic strength for an *artificial* synapse is the conductivity G. Thus we compare the results by Bliss and Collingridge with the conductivity of a mem-

[81] R. Morris et al., Phil. Trans. R. Soc. B **329**, 187 (1990); and V. Doyere et al., Hippocampus **2**, 39 (1992)

EPSP
Excitatory post-synaptic potential

[82] T. Bliss et al., Nature **361**, 31 (1993)

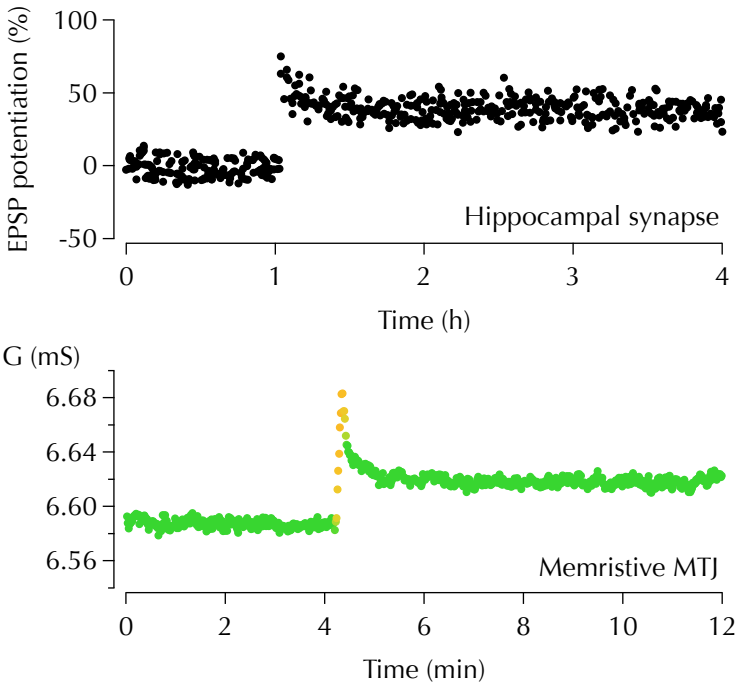

Figure 57: Comparison between LTP of a hippocampal synapse with the according conductivity step of a memristive MTJ. (top) EPSP recorded from a hippocampal synapse. Reproduced from Bilss et al., Nature, **361**, 31 (1993) (bottom) Typical change of conductivity of a memristive MTJ induced by a train with $N_{sp} = 16$ and $v_{max} = +500\,\text{mV}$. The conductivity represents the strength of the artificial synapse.

ristive MTJ stressed by a sine half-wave with $N_{sp} = 16$ and $v_{max} = +500\,\text{mV}$ (bottom graph in fig. 57). The memristive MTJ measurement covers a much shorter timescale (minutes) than the hippocampal experiment (hours). However, from figure 57 a striking qualitative similarity between biological and artificial synapses can be observed.

Also on a longer timescale an impressive accordance of the of LTP induced in biological synapses and the relaxation of memristive MTJs can be observed. Such a decay of LTP is shown in figure 58 (cf. page 47). The top part of the figure plots responses to test stimuli at the first day after conditioning (dashed line) and 31 days thereafter.[83] The arrows indicate the part of the curve where the slope is obtained from.

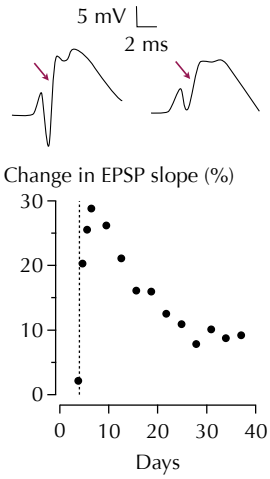

Figure 58: Decay of the LTP for biological synapses. Reproduced from Doyere et al., Hippocampus, **2**, 39 (1992)

The long-term *depression* observed in hippocampal measurements is equally well emulated by memristive MTJs. For a more natural definition of LTD we cite the work of Goda and Stevens.[84] They define the synaptic strength as the ratio of the mean peak synaptic currents. Example current traces are shown in figure 59. The measurement performed on hippocampal neurons grown in culture is shown in the top graph of figure 60. Before LTP the synaptic strength (peak current) is normalized to one. Between the dashed lines the LTD is induced by application of 900 pulses

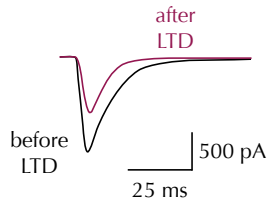

Figure 59: EPSP before and after induction LTD recorded from hippocampal synapses. Reproduced from Goda et al., Neuron, **16**, 103 (1996)

[83] V. Doyere et al., Hippocampus **2**, 39 (1992)

[84] Y. Goda et al., Neuron **16**, 103 (1996)

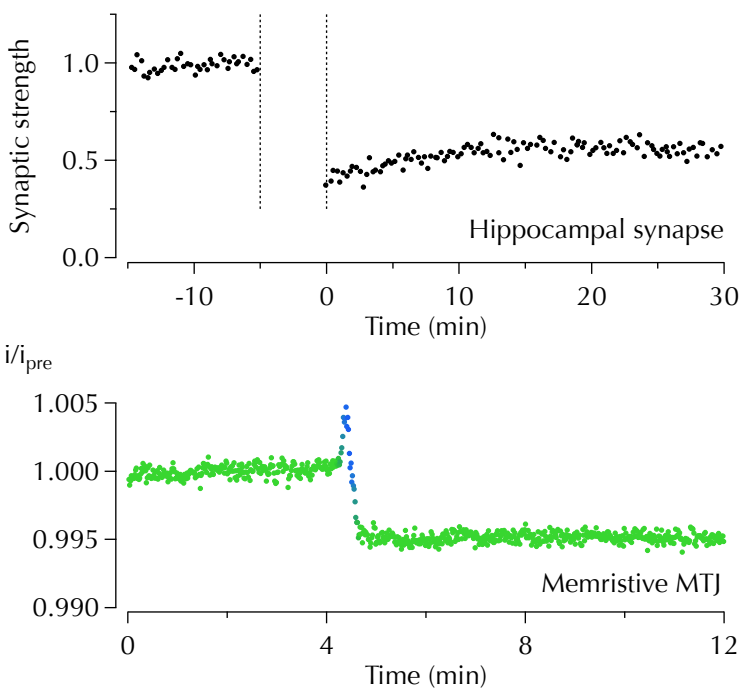

Figure 60: Comparison between LTD of a hippocampal synapse with the according current step of a memristive MTJ. (top) Synaptic strength recorded from a hippocampal synapse. Reproduced from Goda et al., Neuron, **16**, 103 (1996) (bottom) Typical change of conductivity of a memristive MTJ induced by a train with $N_{sp} = 30$ and $v_{max} = -500\,\mathrm{mV}$. The normalized current represents the strength of the artificial synapse.

at 5 Hz. This low frequency stimulation of the presynaptic cell coupled with depolarization of the postsynaptic cell resulted in prolonged and stable depression of the postsynaptic response. The mean postsynaptic strength after LTD induction is reduced to 44 %.

We replot the data from figure 49 as read-out current, i.e., current at 20 mV bias, versus time (bottom curve in fig. 60). This allows for the comparison of strength modulation wit the data of Goda and Stevens—in both cases the amplitude of a current pulse is presented. Clearly, the depression of the artificial synapse is much smaller compared to the hippocampal. From the qualitative agreement, however, one can certainly conclude that memristive MTJs are able to mimic LTD.

To summarize, memristive MTJs bear strong resemblance to biological synapses, though, on shorter timescales and with reduced modification rates.

Flux-dependent plasticity

After LTP and LTD was proofed to be a built-in feature of memristive MTJs, the next natural step would be to demonstrate STDP. To do so, we return to some concepts of the memristor discussed

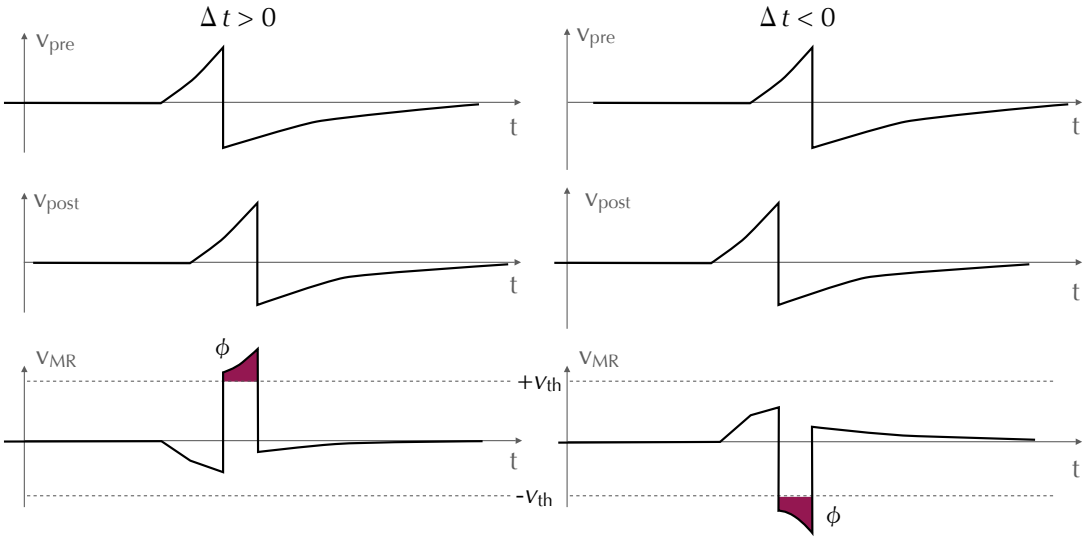

Figure 61: Flux-dependent plasticity induced by the voltage at the memristor $v_{MR} = v_{post} - v_{pre}$. The flux calculated from $v_{MR} > v_{th}$ can be defined as positive for $\Delta t > 0$ and negative for $\Delta t < 0$. This asymmetry is the basis of STDP of memristive MTJs. Reproduced from B. Linares-Barranco et al., Nature Precedings (2009)

in the first chapter and use the well-defined dependence of the resistance on the flux as discussed on page 62.

We follow the scheme proposed by Linares-Barranco et al.[85] The action potential (spike) is assumed to have the form presented in figure 61. It consists of an on-set side and an off-set side. Both might be described by exponential functions and characterized by parameters like amplitude and curvature. The exact shape of the spike is irrelevant at this point. The important features are (i) a not vanishing temporal extent of the pulse and (ii) an amplitude higher than the threshold voltage for memristor activation v_{th}. The meaning of v_{th} is visualized in figure 62 where the hysteresis of the $R(\phi)$-curve opens only within a critical window defined by the ϕ_{th} values.

[85] B. Linares-Barranco and T. Serrano-Gotarredona, Nature Precedings (2009)

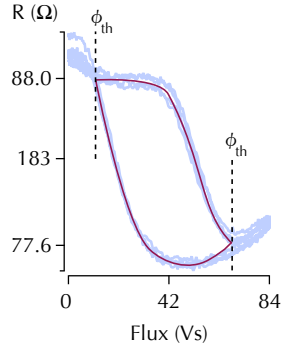

Figure 62: (cf. fig. 14) Typical resistance hysteresis. The hysteresis is open within a critical flux-window as indicated by the reddish lines.

The temporal extend of the pulses is important because we want to use the temporal overlap of both pulses. If v_{pre} is applied to one terminal of the memristor and v_{post} to the other terminal then the net voltage at the synaptic MTJ will be $v_{MR} = v_{post} - v_{pre}$. If furthermore, the spike timing Δt is small enough—this is the Hebbian rule for synaptic plasticity—the two overlapping spikes will create a signal as shown on the bottom of figure 61. The preeminent role of v_{th} is visualized by the reddish area. This area enclosed by v_{th} and v_{MR} can be identified with the over-threshold flux ϕ_{th}.

The timing sensibility is introduced by the reversed sign of the over-threshold part of v_{MR} for reversed temporal order of presynaptic and postsynaptic spike. This is visualized on the right side

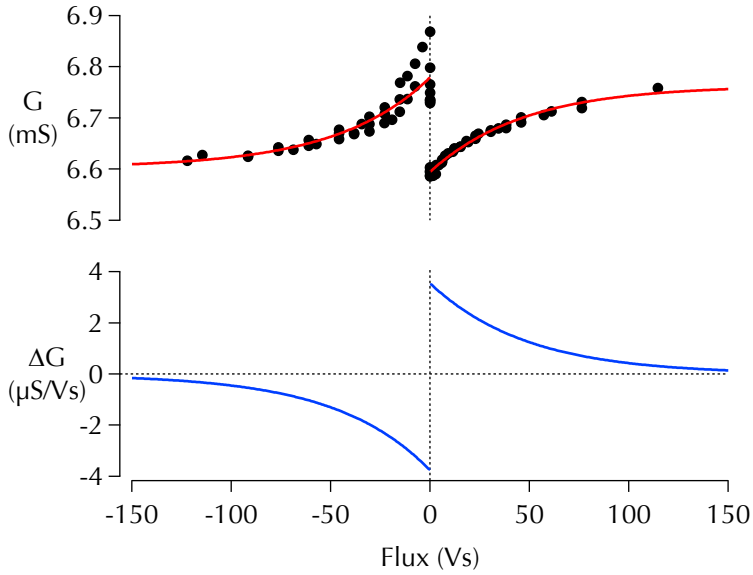

Figure 63: Flux-dependent plasticity of memristive MTJs. (top) The asymmetric conductivity of a memristive MTJ. Positive flux is associated with causal spike-timing, negative flux with anti-causal spike-timing. The asymmetry typical for STDP is evaluated by the fitting curves. (bottom) The derivative of the fitting curves in the top graph is calculated to provide a measure of the change in synaptic strength.

of figure 61 ($\Delta t < 0$). Now the reddish area is at the negative side of v_{MR} and can be associated with negative flux, i.e., the flux due to negative bias.

At the top graph of figure 63 the $G(\phi)$ dependence of memristive MTJs is pictured. A clear resistance decrease with rising positive flux is pictured as discussed in detail on page 62. The noise for the negative flux is higher due to the lower stability of the refresh process. We fit both branches by exponential curves and obtain

$$G(\phi) = \left[148\,\mathrm{mS} + 3.77\,\mathrm{mS} \cdot \exp\left(-\frac{\phi}{46.3\,\mathrm{Vs}}\right)\right]^{-1} \tag{21}$$

for positive bias and

$$G(\phi) = 6.6 \times 10^{-3}\,\mathrm{mS} + 0.177 \times 10^{-3}\,\mathrm{mS} \cdot \exp\left(\frac{\phi}{47\,\mathrm{Vs}}\right). \tag{22}$$

for negative bias. The equivalent to the change in EPSP is defined as $\Delta G = +\mathrm{d}G/\mathrm{d}\phi$ for positive flux and as $\Delta G = -\mathrm{d}G/\mathrm{d}\phi$ for negative flux. The according curves are plotted in figure 63.

We fit the data of Bi et al. (fig. 64) by the same functions as used in figure 63. From the similarity of these curves the STDP of memristive MTJs is demonstrated. In other words, memristive MTJs can be used as nanoscopic causation detection devices.

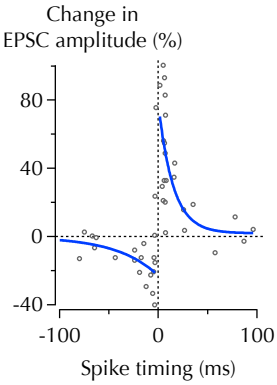

Figure 64: (cf. fig. 46) Critical window for the induction of LTP and LTD in hippocampal neurons (data by Bi et al., J. Neurosci., **15**, 10464 (1998)). The data is fitted by functions of the same type as equation 21 and equation 22.

The characteristics of memristive MTJs arise from the combination of a resistive MIM system with the TMR effect. The first one is driven by the voltage via electric field and the second one by the current via spin torque transfer. Or in the language of the memristor theory: $R = R(\vec{w}, t)$, where $w_1(v)$ describes the voltage driven distribution of vacancies within the barrier and $w_2(j, H) \in \{\text{P}, \text{AP}\}$ gives the magnetic configuration which in general can be set by the current density j, by an external magnetic field H, or a combination of both.

In this section, we turn the attention from synapses to neurons and from barrier properties to the magnetic properties of MTJs and give a new sight on a phenomenon known as back-hopping.[86] Back-hopping is related with a new field of magnetism known as STT switching of magnetization. In STT switching the angular momentum carried by a spin polarized current is transferred to a free magnetic layer. For sufficiently high currents, this will cause a change of the magnetization direction of the free layer.

[86] T. Min et al., J. Appl. Phys. **105**, 07D126 (2009)

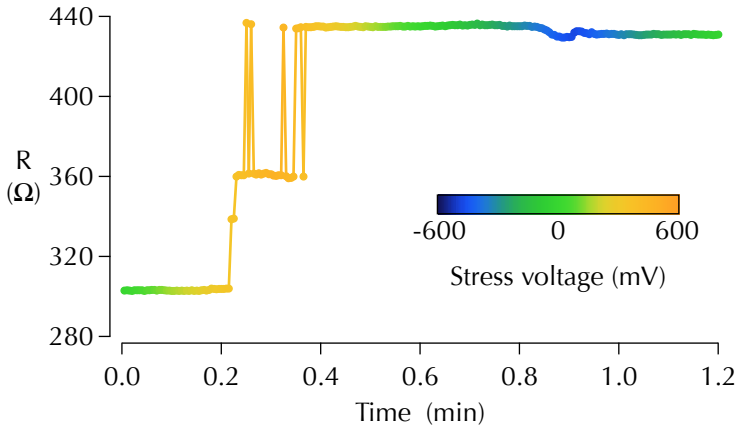

Figure 65: Unipolar back-hopping of a TMR element. The curve is measured at zero magnetic field and at a temperature of 130 K. The spin-torque switching is activated at a stress voltage of +420 mV. For negative stress voltage no spin-torque switching is observed.

Here we present STT measurements[87] obtained from samples with post-oxidized Mg barriers (cf. page page 27). Figure 65 shows a measurement at $T = 130\,\text{K}$, zero magnetic field, and maximum bias of 600 mV. At high positive current density the resistance is switched in an intermediate state (at $t \approx 0.2\,\text{min}$) of around 360 Ω. For this first switching a voltage of +420 mV is applied which results in a current density of $j = 1.8 \times 10^6\,\text{A/cm}^2$. The occurrence of an intermediate state can be explained by the presence of a magnetic domain within the free magnetic layer. The intermediate state, however, is unstable. The magnetization of the

[87] The back-hopping data is provided by M. Schäfers.

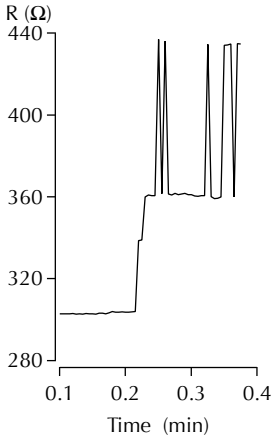

Figure 66: (cf. fig. 65) The back-hopping of a TMR element presented on a shorter time scale.

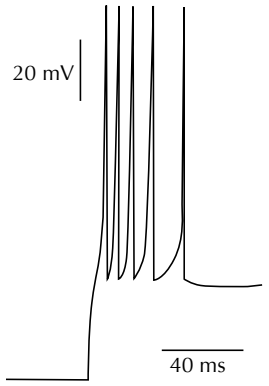

Figure 67: Example for the spiking pattern of a biological neuron. Reproduced from Izhikevich et al., IEEE Trans. Neural Networks, **14**, 1569 (2003)

free layer is switched randomly between the intermediate state and the anti-parallel state—this is due to back-hopping. When the positive bias is released, the sample remains in the AP magnetic state of about 440 Ω. For the negative bias no switching or back-hopping is observed. Just a small bump, possibly associated with resistive effects, occurs close to $t = 0.9$ min. Here the bias reaches its highest negative value of -600 mV (note the color scale).

If the curve is re-plotted on a smaller time scale a remarkable similarity to the spiking of biological neurons comes into view (compare fig. 66 with fig. 67). This leads to the idea that memristive MTJs might not only emulate synapses but also the spiking neuron. At this point nothing but the bare conception can be put forward. Modest literature on back-hopping is available since it is regarded as a parasitic effect, diminishing the quality of STT hysteresis curves.[88]

Integration into CMOS technology

With the rise of neuro-informatics, pattern recognition became the leading exemplar of a task that is particularly difficult to implement on digital computers on the one hand and straightforward for the human brain on the other hand. Humans can effortlessly recognize a person whose appearance has changed by a new hairdo, a beard, or aging. Humans associate things that were not connected before on the circumstances that form the setting for an event, statement, or idea. Humans can guess. Computers do not.

Another frequently discussed weakness of modern digital computers is the so-called von Neumann bottleneck. The von Neumann architecture is a design model for a digital computer that uses a CPU and a single separate storage structure (memory) to hold both instructions and data. The separation between the CPU and memory leads to the von Neumann bottleneck, the limited throughput (data transfer rate) between the CPU and memory. In most modern computers, the throughput is much smaller than the rate at which the CPU can work. This seriously limits the effective processing speed when the CPU is required to perform minimal processing on large amounts of data. The CPU is continuously forced to wait for needed data to be transferred to or from memory. Since CPU speed and memory size have increased much faster than the throughput between them, the bottleneck has become more of a problem with every newer generation of the CPU.

[88] S.-C. Oh et al., Nature Phys. **5**, 898 (2009); J. Z. Sun et al., J. Appl. Phys. **105**, 07D109 (2009); and T. Min et al., IEEE Trans. Magn. **46**, 2322 (2010)

CPU
Central processing unit

The problem can also be somewhat sidestepped by using parallel computing (this approach is commonly employed by supercomputers). Parallel computing is a form of computation in which many calculations are carried out simultaneously, operating on the principle that large problems can often be divided into smaller ones, which are then solved concurrently (in parallel). Parallelism has been employed for many years, mainly in high-performance computing, but interest in it has grown lately due to the physical constraints preventing frequency scaling. As power consumption (and consequently heat generation) by computers has become a concern in recent years, parallel computing has become the dominant paradigm in computer architecture, mainly in the form of multicore processors.

Crossbar architectures allow for a local fusion of logic and memory thus represent an interesting alternative to the conventional von-Neumann-based architecture. Nano-crossbar arrays consist of a set of parallel bottom electrodes and perpendicular top electrodes with a thin layer of active switching material in between. Each crosspoint represents a memory cell where binary information is stored as HRS/AP state or as LRS/P state.

When we consider the industrial possibilities of mass production of networks based on memristive MTJs, the situation is similar to the state we had at the prototype level. Commercial MRAMs are already available on the market.[89] Also memristors are on the way to be implemented for large arrays, mostly by the Hewlett-Packard researches[90] but also by others.[91] Thus, basically two existing technologies have to be brought together.

MRAM
Magnetic random access memory

[89] J. Akerman, Science **308**, 508 (2005)

[90] J. Borghetti et al., Nature **464**, 873 (2010); J. J. Yang et al., Adv. Mater. **21**, 3754 (2009); and G. Snider, IEEE Symposium on Nanoscale Architectures 2008 , 85 (2008)

[91] S. H. Jo et al., Nano Lett. **10**, 1297 (2010); E. Linn et al., Nature Mater. **9**, 403 (2010); and S. H. Jo et al., Nano Lett. **9**, 870 (2009)

Summary

When an electric field is applied to a magnetic tunnel junction, two different transport phenomena occur. First, the spin-dependent transport of the electrons tunneling from the cathode to the anode across a thin insulating layer. In this case, spin-up and spin-down electrons interact differently with the anode which is the basis of spintronics.

The second transport phenomenon takes place within the insulator. Here, induced by the sputter process, charged defects are present. This defects are accelerated in the presence of an electric field and propagate through the insulating layer. This diffusive movement is associated with a change of the barrier properties and thus induce a resistance change.

In the present thesis, this simultaneous magnetoresistive and resistive switching of magnetic tunnel junctions was discussed. We successfully applied the framework of a 2nd order memristive system and described memristive MTJs by the interplay of two state variables: the voltage driven w_1 giving the distribution of defects within the barrier, and the current driven w_2 describing the magnetic configuration of the electrodes. Based on systematic measurements, a specific model of the resistive switching of memristive magnetic tunnel junctions has been developed. Finally, a comprehensive study on the analogy of memristive magnetic tunnel junctions and biological neural systems was performed.

It was demonstrated that the continuous, bipolar resistance change described by $w_1(v)$ can be used to mimic the synaptic connection between neurons. Particularly, the activity-dependent conductivity potentiation/depression as well as the timing-dependent plasticity were observed. These features are believed to be the origin of memory and learning in human brains.

Further, it has been proposed to exploit the bipolar resistance change described by $w_2(j)$ to create artificial neurons. Here, the

magnetization switching driven by spin transfer torque in combination with back-hopping was used to generate current spikes. These spikes show remarkable similarities with the signals generated by excited neurons. The unipolar nature of this process ensures that there is a well-defined forward direction for information propagation as it is the case for biological neural networks.

The memristive magnetic tunnel junction as a complete synapse-neuron-system is envisioned to become the basis of future artificial neural networks. The study of such networks could provide important insights in the functionality of biological networks. It could also lead the way to new forms of computing. Intelligent circuits specialized, for example, for pattern recognition may support todays systems. The flexibility of the former would be combined with the speed of the latter. Alternatively, if an artificial neural network is trained to perform a specific task, perhaps taking months to train, the final result could be etched onto a piece of silicon and mass-produced.

Bibliography

A

J. Åkerman, 'Toward a universal memory,' Science **73**, 1663 (2005).

B

T. Baiatu, R. Waser, and K. Hardtl, 'DC electrical degradation of Perovskite-type titanates: III, A model of the mechanism,' J. Am. Ceram. Soc. **308**, 508 (1990).

C. Bell, V. Han, Y. Sugawara, and K. Grant, 'Synaptic plasticity in a cerebellum-like structure depends on temporal order,' Nature **387**, 278 (1997).

B. Berninger and G. Bi, 'Synaptic modification in neural circuits: a timely action,' Bioessays **24**, 212 (2002).

G. Bi and M. Poo, 'Synaptic modifications in cultured hippocampal neurons: Dependence on spike timing, synaptic strength, and postsynaptic cell type,' J. Neurosci. **18**, 10464 (1998).

T. Bliss and G. Collingridge, 'A synaptic model of memory: long-term potentiation in the hippocampus,' Nature **361**, 31 (1993).

J. Borghetti, G. S. Snider, P. J. Kuekes, J. J. Yang, D. R. Stewart, and R. S. Williams, '"Memristive" switches enable "stateful" logic operations via material implication,' Nature **464**, 873 (2010).

W. Brinkman, R. Dynes, and J. Rowell, 'Tunneling conductance of asymmetrical barriers,' J. Appl. Phys. **41**, 1915 (1970).

W. Butler, X. Zhang, T. Schulthess, and J. MacLaren, 'Spin-dependent tunneling conductance of Fe vertical bar MgO vertical bar Fe sandwiches,' Phys. Rev. B **63**, 054416 (2001).

C

J. Cha, J. Read, R. Buhrman, and D. Muller, 'Spatially resolved electron energy-loss spectroscopy of electron-beam grown and sputtered CoFeB/MgO/CoFeB magnetic tunnel junctions,' Appl. Phys. Lett. **91**, 062516 (2007).

J. Cha, J. Read, W. E. Jr, and P. Huang, 'Atomic-scale spectroscopic imaging of CoFeB/Mg-B-O/CoFeB magnetic tunnel junctions,' Appl. Phys. Lett. **95**, 032506 (2009).

C. Chappert, A. Fert, and F. N. V. Dau, 'The emergence of spin electronics in data storage,' Nature Mater. **6**, 813 (2007).

L. Chua, 'Memristor - The missing circuit element,' IEEE Trans. Circuit Theory **18**, 507 (1971).

L. Chua and S. Kang, 'Memristive devices and systems,' IEEE Proc. **64**, 209 (1976).

D

N. Das, S. Tsui, Y. Y. Xue, Y. Q. Wang, and C. W. Chu, 'Electric-field-induced submicrosecond resistive switching,' Phys. Rev. B **78**, 235418 (2008).

N. Das, S. Tsui, Y. Y. Xue, Y. Q. Wang, and C. W. Chu, 'Kinetics and relaxation of electroresistance in transition metal oxides: Model for resistive switching,' Phys. Rev. B **80**, 115411 (2009).

M. Di Ventra, Y. V. Pershin, and L. Chua, 'Circuit Elements With Memory: Memristors, Memcapacitors, and Meminductors,' IEEE Proc. **97**, 1717 (2009).

S. Dietrich, M. Angerbauer, M. Ivanov, D. Gogl, H. Hoenigschmid, M. Kund, C. Liaw, M. Markert, R. Symanczyk, L. Altimime, S. Bournat, and G. Mueller, 'A nonvolatile 2-Mbit CB-RAM memory core featuring advanced read and program control,' IEEE J. Solid-St. Circ. **42**, 839 (2007).

V. Doyere and S. Laroche, 'Linear relationship between the maintenance of hippocampal long-term potentiation and retention of an associative memory,' Hippocampus **2**, 39 (1992).

G

Y. Goda and C. Stevens, 'Long-term depression properties in a simple system,' Neuron **16**, 103 (1996).

H

D. Halley, H. Majjad, M. Bowen, N. Najjari, Y. Henry, C. Ulhaq-Bouillet, W. Weber, G. Bertoni, J. Verbeeck, and G. V. Tendeloo, 'Electrical switching in Fe/Cr/MgO/Fe magnetic tunnel junctions,' Appl. Phys. Lett. **92**, 212115 (2008).

C. Heiliger, P. Zahn, B. Yavorsky, and I. Mertig, 'Influence of the interface structure on the bias dependence of tunneling magnetoresistance,' Phys. Rev. B **72**, 180406 (2005).

H.-H. Huang, W.-C. Shih, and C.-H. Lai, 'Nonpolar resistive switching in the Pt/MgO/Pt nonvolatile memory device,' Appl. Phys. Lett. **96**, 193505 (2010).

I

E. Izhikevich, 'Simple model of spiking neurons,' IEEE Trans. Neural Networks **14**, 1569 (2003).

J

S. H. Jo, K.-H. Kim, and W. Lu, 'High-Density Crossbar Arrays Based on a Si Memristive System,' Nano Lett. **9**, 870 (2009).

S. H. Jo, T. Chang, I. Ebong, B. B. Bhadviya, P. Mazumder, and W. Lu, 'Nanoscale Memristor Device as Synapse in Neuromorphic Systems,' Nano Lett. **10**, 1297 (2010).

K

E. R. Kandel, J. H. Schwartz, and T. M. Jassell. *Neurowissenschaften.* Heidelberg: Spektrum Akademischer Verlag, 1996.

S. Karthik, Y. Takahashi, T. Ohkubo, and K. Hono, 'Transmission electron microscopy investigation of CoFeB/MgO/CoFeB pseudospin valves annealed at different temperatures,' J. Appl. Phys. **106**, 023920 (2009).

J. A. Katine and E. E. Fullerton, 'Device implications of spin-transfer torques,' J. Magn. Magn. Mater. **320**, 1217 (2008).

C. Koch. *Biophysics of computation: Information Processing in Single Neurons.* Oxford: Oxford University Press, 1999.

P. Krzysteczko, G. Reiss, and A. Thomas, 'Memristive switching of MgO based magnetic tunnel junctions,' Appl. Phys. Lett. **95**, 112508 (2009).

P. Krzysteczko, X. Kou, K. Rott, A. Thomas, and G. Reiss, 'Current induced resistance change of magnetic tunnel junctions with ultra-thin MgO tunnel barriers,' J. Magn. Magn. Mater. **321**, 144 (2009).

D.-H. Kwon, K. M. Kim, J. H. Jang, J. M. Jeon, M. H. Lee, G. H. Kim, X.-S. Li, G.-S. Park, B. Lee, S. Han, M. Kim, and C. S. Hwang, 'Atomic structure of conducting nanofilaments in TiO_2 resistive switching memory,' Nature Nanotech. **5**, 148 (2010).

L

J. Larson, D. Wong, and G. Lynch, 'Patterned stimulation at the theta frequency is optimal for the induction of hippocampal long-term potentiation,' Brain Res. **368**, 347 (1986).

E. Linn, R. Rosezin, C. Kuegeler, and R. Waser, 'Complementary resistive switches for passive nanocrossbar memories,' Nature Mater. **9**, 403 (2010).

Y. Liu, Z. Zhang, P. Freitas, and J. Martins, 'Current-induced magnetization switching in magnetic tunnel junctions,' Appl. Phys. Lett. **82**, 2871 (2003).

M

W. Maass and C. M. Bishop, *Pulsed Neural Networks.* Cambridge: The MIT Press, 1999

J. Magee and D. Johnston, 'A synaptically controlled, associative signal for Hebbian plasticity in hippocampal neurons,' Science **275**, 209 (1997).

J. Maier, 'Nanoionics: ion transport and electrochemical storage in confined systems,' Nature Mater. **4**, 805 (2005).

H. Markram, J. Lubke, M. Frotscher, and B. Sakmann, 'Regulation of synaptic efficacy by coincidence of postsynaptic APs and EPSPs,' Science **275**, 213 (1997).

J. Mathon and A. Umerski, 'Theory of tunneling magnetoresistance of an epitaxial Fe/MgO/Fe(001) junction,' Phys. Rev. B **63**, 220403 (2001).

G. I. Meijer, 'Materials science - Who wins the nonvolatile memory race?', Science **319**, 1625 (2008).

R. Meyer, L. Schloss, J. Brewer, R. Lambertson, W. Kinney, J. Sanchez, and D. Rinerson, 'Oxide dual-layer memory element for scalable non-volatile cross-point memory technology,' IEEE Non-Volatile Memory Technology Symposium, 2008.

H. Meyerheim, R. Popescu, N. Jedrecy, M. Vedpathak, M. Sauvage-Simkin, R. Pinchaux, B. Heinrich, and J. Kirschner, 'Surface x-ray diffraction analysis of the MgO/Fe(001) interface: Evidence for an FeO layer,' Phys. Rev. B **65**, 144433 (2002).

G. Miao, Y. Park, J. Moodera, M. Seibt, and G. Eilers, 'Disturbance of Tunneling Coherence by Oxygen Vacancy in Epitaxial Fe/MgO/Fe Magnetic Tunnel Junctions,' Phys. Rev. Lett. **100**, 246803 (2008).

T. Min, J. Z. Sun, R. Beach, D. Tang, and P. Wang, 'Back-hopping after spin torque transfer induced magnetization switching in magnetic tunneling junction cells,' J. Appl. Phys. **105**, 07D126 (2009).

T. Min et al., 'A Study of Write Margin of Spin Torque Transfer Magnetic Random Access Memory Technology,' IEEE Trans. Magn. **46**, 2322 (2010).

J. Moodera and G. Mathon, 'Spin polarized tunneling in ferromagnetic junctions,' J. Magn. Magn. Mater. **200**, 248 (1999).

R. Morris, S. Davis, and S. Butcher, 'Hippocampal synaptic plasticity and NMDA receptors: a role in information storage?' Phil. Trans. R. Soc. B **329**, 187 (1990).

M. Müller, F. Matthes, and C. Schneider, 'Spin polarization at ferromagnet-insulator interfaces: The important role of stoichiometry in MgO/Fe (001)', Europhys. Lett. **80**, 17007 (2007).

N. Najjari, D. Halley, M. Bowen, H. Majjad, Y. Henry, and B. Doudin, 'Electrical switching in Fe/V/MgO/Fe tunnel junctions,' Phys. Rev. B **81**, 174425 (2010).

N

Y. Nian, J. Strozier, N. Wu, X. Chen, and A. Ignatiev, 'Evidence for an oxygen diffusion model for the electric pulse induced resistance change effect in transition-metal oxides,' Phys. Rev. Lett. **98**, 146403 (2007).

J. G. Nicholls, A. R. Martin, B. G. Wallace, and P. A. Fuchs. *From Neuron to Brain.* Sunderland: Sinauer Associates, 2001.

O

J. J. O'Dwyer. *The theory of electrical conduction and breakdown in solid dielectrics.* Oxford: Clarendon Press, 1973.

S.-C. Oh, S.-Y. Park, A. Manchon, M. Chshiev, J.-H. Han, H.-W. Lee, J.-E. Lee, K.-T. Nam, Y. Jo, Y.-C. Kong, B. Dieny, and K.-J. Lee, 'Bias-voltage dependence of perpendicular spin-transfer torque in asymmetric MgO-based magnetic tunnel junctions,' Nature Phys. **5**, 898 (2009).

S. R. Ovshinsky, 'Reversible electrical switching phenomena in disordered structures,' Phys. Rev. Lett. **21**, 1450 (1968).

Q

M. Quintero, P. Levy, A. G. Leyva, and M. J. Rozenberg, 'Mechanism of electric-pulse-induced resistance switching in manganites,' Phys. Rev. Lett. **98**, 116601 (2007).

R

J. C. Read, P. G. Mather, and R. A. Buhrman, 'X-ray photoemission study of CoFeB/MgO thin film bilayers,' Appl. Phys. Lett. **90**, 132503 (2007).

G. Reiss and D. Meyners, 'Reliability of field programmable magnetic logic gate arrays,' Appl. Phys. Lett. **88**, 043505 (2006).

G. Rose and T. Dunwiddie, 'Introduction of hippocampal long-term potentiation using physiologically patterned stimulation,' Neurosci. Lett. **69**, 244 (1986).

M. Rozenberg, I. Inoue, and M. Sanchez, 'Nonvolatile memory with multilevel switching: A basic model,' Phys. Rev. Lett. **92**, 178302 (2004).

M. Rozenberg, I. Inoue, and M. Sanchez, 'A model for nonvolatile electronic memory devices with strongly correlated materials,' Thin Solid Films **486**, 24 (2005).

M. Rozenberg, I. Inoue, and M. Sanchez, 'Strong electron correlation effects in nonvolatile electronic memory devices,' Appl. Phys. Lett. **88**, 033510 (2006).

M. J. Rozenberg, M. J. Sánchez, R. Weht, C. Acha, F. Gomez-Marlasca, and P. Levy, 'Mechanism for bipolar resistive switching in transition-metal oxides,' Phys. Rev. B **81**, 115101 (2010).

S

A. Sawa, T. Fujii, M. Kawasaki, and Y. Tokura, 'Hysteretic current -voltage characteristics and resistance switching at a rectifying Ti/PrCaMnO interface,' Appl. Phys. Lett. **85**, 4073 (2004).

A. Sawa, 'Resistive switching in transition metal oxides,' Mater. Today **11**, 28 (2008).

H. Schmalzried and A. Navrotsky. *Festkörperthermodynamik.* Weinheim: Verlag Chemie, 2004.

J. Slonczewski, 'Current-driven excitation of magnetic multilayers,' J. Magn. Magn. Mater. **159**, L1 (1996).

G. Snider, 'Spike-timing-dependent learning in memristive nanodevices,' IEEE Symp. Nanoscale Architectures 85 (2008).

D. B. Strukov, G. S. Snider, D. R. Stewart, and R. S. Williams, 'The missing memristor found,' Nature **453**, 80 (2008).

D. B. Strukov and R. S. Williams, 'Exponential ionic drift: fast switching and low volatility of thin-film memristors,' Appl. Phys. A **94**, 515 (2009).

D. B. Strukov, J. L. Borghetti, and R. S. Williams, 'Coupled Ionic and Electronic Transport Model of Thin-Film Semiconductor Memristive Behavior,' Small **5**, 1058 (2009).

J. Z. Sun, M. C. Gaidis, G. Hu, E. J. O'Sullivan, S. L. Brown, J. J. Nowak, P. L. Trouilloud, and D. C. Worledge, 'High-bias backhopping in nanosecond time-domain spin-torque switches of MgO-based magnetic tunnel junctions,' J. Appl. Phys. **105**, 07D109 (2009).

K. Szot, W. Speier, G. Bihlmayer, and R. Waser, 'Switching the electrical resistance of individual dislocations in single-crystalline $SrTiO_3$', Nature Mater. **5**, 312 (2006).

T

J. M. Teixeira, J. Ventura, R. Fermento, J. P. Araujo, J. B. Sousa, P. Wisniowski, and P. P. Freitas, 'Electroforming, magnetic and resistive switching in MgO-based tunnel junctions,' J. Phys. D: Appl. Phys. **42**, 105407 (2009).

S. Tsui, A. Baikalov, J. Cmaidalka, Y. Sun, Y. Wang, Y. Yue, C. Chu, L. Chen, and A. Jacobson, 'Field-induced resistive switching in metal-oxide interfaces,' Appl. Phys. Lett. **85**, 317 (2004).

V

J. Ventura, J. Sousa, Y. Liu, Z. Zhang, and P. Freitas, 'Electromigration in thin tunnel junctions with ferromagnetic/nonmagnetic electrodes: Nanoconstrictions, local heating, and direct and wind forces,' Phys. Rev. B **72**, 094432 (2005).

J. Ventura, J. Araujo, J. Sousa, Y. Liu, Z. Zhang, and P. Freitas, 'Nanoscopic processes of current-induced switching in thin tunnel junctions,' IEEE Trans. Nanotech. **5**, 142 (2006).

W

X. Wang, Y. Chen, H. Xi, H. Li, and D. Dimitrov, 'Spintronic Memristor Through Spin-Torque-Induced Magnetization Motion,' IEEE Electron Device Lett. **30**, 294 (2009).

R. Waser and M. Aono, 'Nanoionics-based resistive switching memories,' Nature Mater. **6**, 833 (2007).

R. Waser, R. Dittmann, G. Staikov, and K. Szot, 'Redox-Based Resistive Switching Memories—Nanoionic Mechanisms, Prospects, and Challenges,' Adv. Mater. **21**, 2632 (2009).

B. Widrow, 'An adaptive ADALINE neuron using chemical memistors,' Stanford Electronics Laboratories Technical Report **1553**, 1 (1960).

M. Wuttig and N. Yamada, 'Phase-change materials for rewriteable data storage,' Nature Mater. **6**, 824 (2007).

Y

J. J. Yang, J. Borghetti, D. Murphy, D. R. Stewart, and R. S. Williams, 'A Family of Electronically Reconfiguiable Nanodevices,' Adv. Mater. **21**, 3754 (2009).

J. J. Yang, F. Miao, M. D. Pickett, D. A. A. Ohlberg, D. R. Stewart, C. N. Lau, and R. S. Williams, 'The mechanism of electroforming of metal oxide memristive switches,' Nanotechnology **20**, 215201 (2009).

C. Yoshida, M. Kurasawa, Y. M. Lee, M. Aoki, and Y. Sugiyama, 'Unipolar resistive switching in CoFeB/MgO/CoFeB magnetic tunnel junction,' Appl. Phys. Lett. **92**, 113508 (2008).

S. Yuasa and D. D. Djayaprawira, 'Giant tunnel magnetoresistance in magnetic tunnel junctions with a crystalline MgO(001) barrier,' J. Phys. D: Appl. Phys. **40**, R337 (2007).

Z

X. Zhang, W. Butler, and A. Bandyopadhyay, 'Effects of the iron-oxide layer in Fe-FeO-MgO-Fe tunneling junctions,' Phys. Rev. B **68**, 092402 (2003)

Total number of citations: 89

Journal of Magnetism and Magnetic Materials 321 (2009) 144–147

Contents lists available at ScienceDirect

Journal of Magnetism and Magnetic Materials

journal homepage: www.elsevier.com/locate/jmmm

Current induced resistance change of magnetic tunnel junctions with ultra-thin MgO tunnel barriers

Patryk Krzysteczko [a,*], Xinli Kou [b], Karsten Rott [a], Andy Thomas [a], Günter Reiss [a]

[a] Thin Films and Physics of Nanostructures, Bielefeld University, 33615 Bielefeld, Germany
[b] School of Physical Science and Technology, Lanzhou University, Lanzhou, China

ARTICLE INFO

Article history:
Received 27 July 2008
Available online 22 August 2008

PACS:
68.35.Dv
72.25.−b
73.40.Gk

Keywords:
Diffusion
Electromigration
Tunneling
Current induced switching
Memristive behavior

ABSTRACT

Ultra-thin magnetic tunnel junctions with low resistive MgO tunnel barriers are prepared to examine their stability under large current stress. The devices show magnetoresistance ratios of up to 110% and an area resistance product of down to 4.4 Ω μm^2. If a large current is applied, a reversible resistance change is observed, which can be attributed to two different processes during stressing and one relaxation process afterwards. Here, we analyze the time dependence of the resistance and use a simple model to explain the observed behavior. The explanation is further supported by numerical fits to the data in order to quantify the timescales of the involved phenomena.

1. Introduction

The switching of a ferromagnet's magnetization by injection of a spin polarized current (spin transfer torque, STT, switching) is an important new phenomenon in magnetism [1,2]. It enables applications such as spin torque nano-oscillators (STNO), magnetic random access memory (MRAM), programmable magnetic logic and sensors [3] using the tunneling magnetoresistance (TMR) effect [4–6]. The conventional switching scheme of field pulses generated by current lines requires large currents and is not scalable, which led to alternatives such as heat assisted [7] or the already mentioned STT switching [8]. In state-of-the-art MgO based magnetic tunnel junctions (MTJs), STT requires current densities of about 1×10^6 A/cm^2 [9]. This leads to a bias voltage of about 100 mV, if the area-resistance products *RA* are in the order of 10 Ω μm^2.

Individual STNOs are strongly limited in their output power. This deficiency has to be overcome in order to exploit the benefits of current-tunable narrow-linewidth microwave generation for future application. Although an array of coupled oscillators may offer a path to higher power output [10], the individual STNOs are envisioned to be MTJ-based and operating close to the degradation current limit [3,11]. Note that STNOs are operated at direct currents in contrast to pulsed currents in the case of MRAMs.

A constant trend to reach lower area resistance products forced the fabrication of MTJs with barriers as thin as 10 Å. Further reduction of the tunnel barrier thickness is becoming more and more challenging. Recently, reversible resistance changes and an atypical temperature dependence of the resistance were observed in thin AlO_x MTJs when reaching current densities of 10^4–10^6 A/cm^2 [12]. These resistance changes do not depend on the relative orientation of the magnetic layers [12] and are attributed to electromigration in nano-constrictions of the insulating barrier [13,14]. Two opposite relaxation processes were found suggesting two independent mechanisms acting simultaneously inside the MTJs [13].

Here, we study the effect of current stressing on ultra-thin MgO barriers. In these devices, resistance changes take place at a current density of about 10^6 A/cm^2. This shows that further reduction of the STT switching currents is crucial in order to achieve reliable operation of STT–MTJ based devices. We distinguish two effects during the current stress and one relaxation process. Furthermore, numerical fits to the experimental data are presented.

2. Results

The TMR systems with low resistive MgO barriers is sputter deposited in a Singulus TIMARIS II tool. The film sequence is Ta

* Corresponding author. Tel./fax: +49 5211065427.
E-mail address: patryk@physik.uni-bielefeld.de (P. Krzysteczko).

0304-8853/$ - see front matter © 2008 Elsevier B.V. All rights reserved.
doi:10.1016/j.jmmm.2008.08.088

3/Cu–N 90/Ta 5/Pt–Mn 20/Co–Fe 2/Ru 0.75/Co–Fe–B 2/MgO 1.3/Co–Fe–B 3/Ta 10/Cu 30/Ru 7 (all values in nm). The composition of the compounds is: $Pt_{37}Mn_{63}$, $Co_{70}Fe_{30}$, and $Co_{66}Fe_{22}B_{12}$. Elliptical TMR elements with sizes in the range of 0.018–0.095 μm^2 are prepared by e-beam lithography in combination with ion beam etching. By applying different Ar pressures during MgO deposition two sample sets with an area-resistance product of 4.4 $\Omega\,\mu m^2$ (set 1) and 9.7 $\Omega\,\mu m^2$ (set 2) are produced.

All measurements are performed using a constant voltage source at room temperature. By applying a voltage in the range of 200–800 mV the samples are stressed by a current density of $1-10\times10^6$ A/cm^2. A magnetic field of ±400 Oe provides a stable parallel/anti-parallel orientation of the magnetic layers during the measurements. The resistance is monitored at a read-out voltage of 20 mV with a rate of 1 Hz in order to overcome non-linear $I(V)$-contributions and thermal drifts related with heating processes (heating rates due to current load have typical time constants well below 1 ns [15]). Each measurement is performed on an individual element which was not stressed before. This is necessary since the properties of the barrier may change irreversibly by the stressing.

Fig. 1 shows the MTJ resistance upon stressing with positive voltage polarity (electrons flow from the bottom to the top electrode). The area-resistance product is $RA = 9.7\,\Omega\,\mu m^2$. The inset shows the magnetic minor loops before (black) and after (gray) stressing exhibiting TMR ratios of the junction of 104% and 108% at 20 mV, respectively. This increase in TMR gives evidence, that the barrier itself does not degrade during current stressing. As the device is stressed by $j = +1.5\times10^6$ A/cm^2 one can see a decay of the resistance with time, although the films had been annealed for 1.5 h at 360 °C prior to patterning. The initial resistance of $R_{ini} = 465\,\Omega$ is reduced reaching a saturation resistance of $R_{sat} = 442\,\Omega$ within 30 min. Numerically, the measured time dependence of the resistance can be fitted with moderate quality by an exponential function:

$$R(t) = R_{sat} + \Delta R \cdot \exp(-t/\tau) \quad (1)$$

with $\Delta R = R_{ini} - R_{sat} > 0$. This would represent a process characterized by a decay time of $\tau = 3.15$ min and leads to the dashed line in Fig. 1 as will be further discussed below.

Stressing the MTJs with currents of the negative polarity leads to a substantially different response shown in Fig. 2. First, the resistance rapidly increases from $R_{ini} = 82.5\,\Omega$ to $R_{max} = 84.5\,\Omega$, followed by a slow decay. No saturation of the resistance can be seen within the measured time range.

Thus, at least two processes are involved: a fast, polarity dependent resistance change followed by a slow resistance decrease for both polarities:

$$R(t) = R_{sat} + \Delta R_1 \exp(-t/\tau_1) + \Delta R_2 \exp(-t/\tau_2) \quad (2)$$

with $\Delta R_1 > 0$ (<0) for positive (negative) polarity and $\Delta R_2 > 0$ for both polarities. These two exponential decays of different sign give a very good fit to the data of Fig. 2 (solid line) with $\tau_1 = 2.8 \pm 0.2$ min and $\tau_2 = 15.1 \pm 2.7$ min. Looking back to Fig. 1 the fast process might be hidden in the decrease because the sign depends on the polarity of the applied voltage: two exponential decreases would lie on top of each other. In fact with Eq. (2) a better fit to the data of Fig. 1 can be obtained (solid line). In this case, however, the fit parameters τ_1 and τ_2 are strongly correlated and cannot be used for a quantitative analysis.

The dependence of the time constant τ (Fig. 1, dashed line) on the RA product of the junctions is shown in Fig. 3 for different positive stressing voltages. For increasing voltage a decrease in τ is

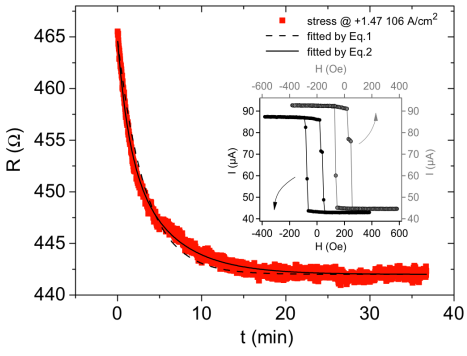

Fig. 1. Resistance as a function of time for the positive current polarity. A fast resistance decrease can be observed during the first 5 min. The data are fitted using Eqs. (1) and (2) as shown by the dashed and solid lines, respectively. The inset shows the minor loop of the investigated MTJ before (black) and after (gray) stressing.

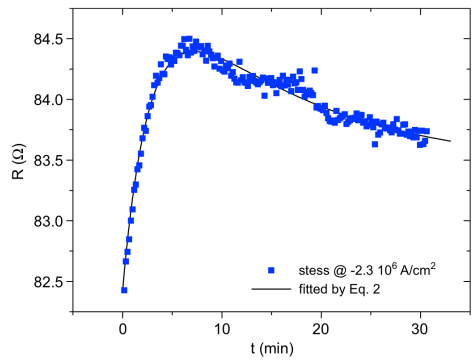

Fig. 2. Resistance as a function of time for the negative polarity. A fast increase in the resistance is followed by a slow decrease. The data are fitted by Eq. (2) as shown by the solid line.

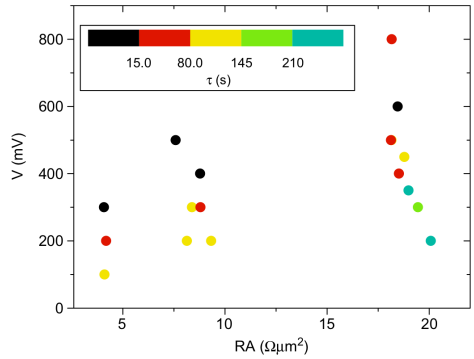

Fig. 3. Decay time τ presented by a color scale as a function of voltage and area-resistance. A decrease with increasing voltage is observed. Increasing the area-resistance at a given voltage leads to a larger τ.

observed. At the same time, for a given voltage, τ increases with increasing RA product.

Fig. 4 shows the current induced resistance variation ΔR as a function of the current density. A decrease in the resistance can be seen reaching 13% at a current density of $j = 4.5 \times 10^6$ A/cm^2 for sample set 2. For sample set 1 ΔR is reduced by a factor of approximately 0.45 due to the lower RA. This can be seen from Fig. 4 where the black line shows a linear fit to the data of sample 2 and the green line is generated by changing the slope of the black line by the RA ratio which is 8.9–19.8 $\Omega\,\mu$m^2 for the antiparallel state. In contrast to this, the magnetic orientation of the electrodes (compare green and orange squares) produces no significant differences. This leads to the conclusion that the current density and not the electric field is the main parameter that determines ΔR.

If we investigate the relaxation of the resistance, i.e. the resistance change after the current stress is released, one can reveal a third process involved. The red curve in Fig. 5 is equivalent to the plot shown in Fig. 1, the blue curve is equivalent to the plot in Fig. 2. The green curve in Fig. 5 illustrates the relaxation process: If no large voltage/current is applied (20 mV), the resistance slowly reaches the initial level R_0. This can also be fitted with an exponential function with typical relaxation times of 100 min.

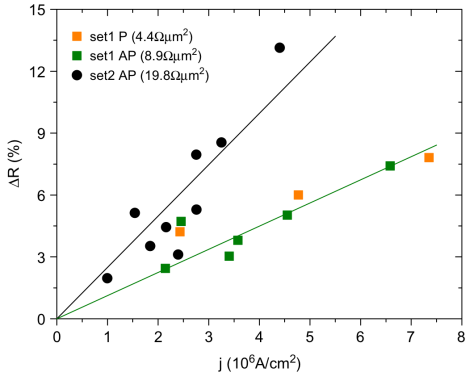

Fig. 4. Resistance change as a function of current density. The black line represents a linear fit to the results obtained from sample set 2. The slope of the green line is calculated from the difference in RA between set 1 and 2. Parallel and antiparallel alignment of the magnetic electrodes is indicated by P and AP, respectively.

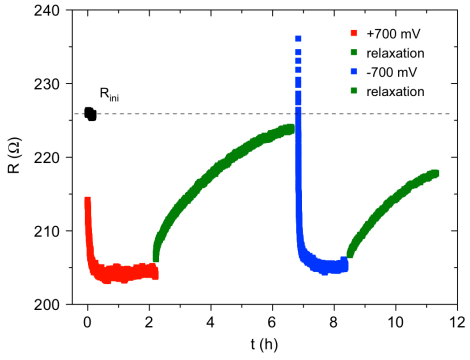

Fig. 5. (Color online) Resistance behavior under stressing with positive polarity (red), during the relaxation (green), stressing with negative polarity (blue), and relaxation (green). The resistance R_{ini} as obtained prior to the stressing is indicated by the dashed line.

3. Discussion

For the interpretation of the data, one has to consider that the resistance of a (magnetic) tunnel junction is governed by the barrier thickness d and the barrier height Φ. This relationship can be described by Brinkman's equation [16]. For barrier height (0.5–3.5 eV) and thickness (1–1.5 nm) that correspond to our junctions, the Brinkman equation can be reduced to

$$R(d, \Phi) = c_1 \cdot \exp(c_2 d \Phi^{1/2}), \tag{3}$$

where c_1 and c_2 are constants. Thus, the resistance changes as given by Eq. (1) could be explained by a variation of d as well as Φ.

If we assume that the effective barrier thickness changes by a certain fraction with a nominal thickness of Δd, Brinkmans's equation leads to $\Delta d \approx 0.1$ Å, if the resistance change is about 5%. For a change of Φ, a resistance change of 5% leads to $\Delta\Phi \approx 10$ meV. Thus, very small changes in the barrier characteristics can lead to the observed resistance changes. Provided small changes of d or Φ results in a linear approximation of Eq. (3) and the experimental findings (Eq. (1)) lead to an exponential function for either $d(t) \propto (1 + \exp(-t/\tau))$ or $\Phi(t) \propto (1 + \exp(-t/\tau))$ as well.

Since the layer stack is symmetric (CoFeB/MgO/CoFeB), the same resistance change for positive and negative biases is expected. The symmetry break is induced by the sequence of preparation. The lower ferromagnet is more likely to be contaminated with oxygen [17], because the MgO is deposited on top of the ferromagnet by RF-sputtering from an MgO target. This oxygen on top of the ferromagnet can act as an additional barrier [18] and also lead to oxygen deficiencies in the lower part of the tunnel barrier. Also the effective barrier height Φ is modified by the presence of oxygen vacancies [19,20].

Therefore, a possible explanation for the observed behavior is a small displacement of these oxygen vacancies/defect atoms driven (fast) in the direction of the electron flow increasing or decreasing the effective thickness of this layer (electromigration) [14] and (slow) by thermal activation. These processes are reversible since the atoms can slowly fall back into their initial positions of lower energy once the current is switched off.

4. Summary

In summary, we investigate magnetic tunnel junctions with MgO barriers with magnetoresistance ratios of up to 110% and area-resistances of around 10 $\Omega\,\mu$m^2. The low resistance of these devices allow us to drive large currents through the structures, which is necessary for use in spin transfer torque memory or logic cells. We observe three reversible resistance changes of the junctions: One fast, polarity dependent term that could be associated with electromigration. One slower, polarity independent term active during current stress, that is suggested to be of thermal origin. Finally, a very slow relaxation takes place when the current stress is released, which also can be explained by thermally activated diffusion.

Acknowledgments

The authors gratefully acknowledge Singulus Technologies for providing the samples. P.K. is supported by the Deutsche

Forschungsgemeinschaft (DFG) through Schwerpunktprojekt 1133. X.K. is supported by the DFG within Grant no. RE 1052/16-1.

References

[1] J. Slonczewski, J. Magn. Magn. Mater. 159 (1996) L1.
[2] L. Berger, Phys. Rev. B 54 (1996) 9353.
[3] J. Katine, E.E. Fullerton, J. Magn. Magn. Mater. 320 (2008) 1217.
[4] J.S. Moodera, L.R. Kinder, T.M. Wong, R. Meservey, Phys. Rev. Lett. 74 (1995) 3273.
[5] T. Miyazaki, N. Tezuka, J. Magn. Magn. Mater. 139 (1995) 231.
[6] W.H. Butler, X.-G. Zhang, T.C. Schulthess, J.M. MacLaren, Phys. Rev. B 63 (2001) 054416.
[7] I.L. Prejbeanu, M. Kerekes, R.C. Sousa, H. Sibuet, O. Redon, B. Dieny, J.P. Nozières, J. Phys. Condens. Matter 19 (2007) 165218.
[8] J.A. Katine, F.J. Albert, R.A. Buhrman, E.B. Myers, D.C. Ralph, Phys. Rev. Lett. 84 (2000) 3149.
[9] J.Z. Sun, IBM J. Res. Dev. 50 (2006) 81.
[10] S. Kaka, M.R. Pufall, W.H. Rippard, T.J. Silva, S.E. Russek, J.A. Katine, Nature 437 (2005) 389.
[11] A.V. Nazarov, K. Nikolaev, Z. Gao, H. Cho, D. Song, J. Appl. Phys. 103 (2008) 07A503.
[12] J. Ventura, J.B. Sousa, Y. Liu, Z. Zhang, P.P. Freitas, Phys. Rev. B 72 (2005) 094432.
[13] J. Ventura, J. Araujo, F. Carpinteiro, J. Sousa, Y. Liu, Z. Zhang, P. Freitas, J. Magn. Magn. Mater. 290–291 (2005) 1067.
[14] J. Ventura, J.P. Araújo, J.B. Sousa, Y. Liu, Z. Zhang, P. Freitas, IEEE Trans. Nanotech. 5 (2006) 142.
[15] J. Ventura, A. Pereira, J. Araujo, J. Sousa, Z. Zhang, Y. Liu, P. Freitas, J. Phys. D Appl. Phys. 50 (2007) 5819.
[16] W.F. Brinkman, R.C. Dynes, J.M. Rowell, J. Appl. Phys. 41 (1970) 1915.
[17] J.C. Read, P.G. Mather, R.A. Buhrman, Appl. Phys. Lett. 90 (2007) 132503.
[18] X.-G. Zhang, W.H. Butler, A. Bandyopadhyay, Phys. Rev. B 68 (2003) 092402.
[19] A. Gibson, R. Haydock, J.P. LaFemina, Phys. Rev. B 50 (1994) 2582.
[20] P.G. Mather, J.C. Read, R.A. Buhrman, Phys. Rev. B 73 (2006) 205412.

Memristive switching of MgO based magnetic tunnel junctions

Patryk Krzysteczko,[a] Günter Reiss, and Andy Thomas
Thin Films and Physics of Nanostructures, Bielefeld University, 33615 Bielefeld, Germany

(Received 9 July 2009; accepted 19 August 2009; published online 17 September 2009)

Here we demonstrate that both, tunnel magnetoresistance (TMR) and resistive switching (RS), can be observed simultaneously in nanoscale magnetic tunnel junctions. The devices show bipolar RS of 6% and TMR ratios of about 100%. For each magnetic state, multiple resistive states are created depending on the bias history, which provides a method for multibit data storage and logic. The electronic transport measurements are discussed in the framework of a memristive system. Differently prepared MgO barriers are compared to gain insight into the switching mechanism. © *2009 American Institute of Physics*. [doi:10.1063/1.3224193]

The search for nonvolatile memory concepts has a massive impact on the development of nanoscopic systems with adjustable electrical properties. Capacitorlike structures composed of insulating materials sandwiched between metallic electrodes are envisioned to overcome the limitations associated with conventional charge storage devices and may open the road to neuromorphic computing. Together with phase-change memories[1,2] two concepts attracted extensive interest:[3] resistive and magnetoresistive random access memories (RAM). In resistive RAM, electrochemical processes within the insulating layer enable the access to multiple resistive states.[4–7] For magnetic RAM, ferromagnetic electrodes are used to switch the resistance by changing the alignment of the electrodes from parallel (P) to antiparallel (AP) and vice versa.[8–10]

The concurrent modulation of two material parameters can be treated by the memristor theory formulated by Leon Chua in 1971.[11] The interest in this concept was renewed in 2008 due to experimental progress by Strukov *et al.*[12] where a memristor was realized as a Pt/TiO/Pt sandwich. The memristor "remembers" the history of the applied voltage v and current i since its resistivity depends on the time integrals of v and i. A voltage controlled memristor can be described by $v(t)=R[\Phi(t)]i(t)$, where $\Phi(t)=\int_0^t v(t')dt'$ is referred to as flux and R is the (memory) resistance.[13,14] In the more general concept of an nth order memristive system,[15] this equation turns to

$$v(t) = R(\boldsymbol{w}, v, t)i(t), \tag{1}$$

$$\dot{\boldsymbol{w}} = f(\boldsymbol{w}, v, t), \tag{2}$$

where $\boldsymbol{w}$ is a set of n state variables describing the device.[13–15] Neither R nor f are explicit functions of v in the case of a "pure" memristor.

After substantial effort was invested in studies of resistive and magnetoresistive systems, the next step is a combination of both effects in one device.[16–18] These systems can be treated as second order memristive systems with w_1 the magnetic state of the electrodes and w_2 describing the state of the barrier. In this framework, we present studies on MgO based low resistive magnetic tunnel junctions (MTJs) with $Co_{66}Fe_{22}B_{12}$ electrodes. The samples are characterized by tunnel magnetoresistance (TMR) ratios of about 100% and exhibit an additional bipolar resistive switching (RS) of up to 6%. The TMR ratio is not reduced by the operation as resistive memory and the area resistance is low (6.8 $\Omega\ \mu m^2$). Therefore, the presented results are a step toward a combined magnetoresistive and resistive memory that could be switched by spin transfer torque.[19]

The TMR systems are sputter deposited in a Singulus TIMARIS II tool. The film sequence is (bottom) Ta 3 /Cu–N 90/Ta 5/$Pt_{37}Mn_{63}$ 20/$Co_{70}Fe_{30}$ 2/Ru 0.75/$Co_{66}Fe_{22}B_{12}$ 2/ MgO 1.3/ $Co_{66}Fe_{22}B_{12}$ 3/ Ta 10/ Cu 30/ Ru 7 (top); the thickness is given in nanometers. Elliptical TMR elements with sizes of $0.038 \pm 0.005\ \mu m^2$ are prepared by electron beam lithography in combination with ion beam etching. All measurements are performed using a constant voltage source at room temperature with the bottom electrode grounded. We apply voltage pulses of up to 650 mV for 1 s to stress the samples by a current density of typically $8 \times 10^6\ A/cm^2$. All resistance values presented in this paper are measured at a read-out voltage of 20 mV and with a read-out delay of 200 ms after each stress pulse. This removes nonlinear contributions resulting from voltage-dependent tunnel resistance.[20]

Figure 1 shows the current-voltage (i-v) curves for the P and AP orientation of the Co–Fe–B electrodes. The current value measured for increasing voltage is slightly lower than the current measured for decreasing voltage. This hysteresis of the i-v curve is observed in both magnetic states and is the

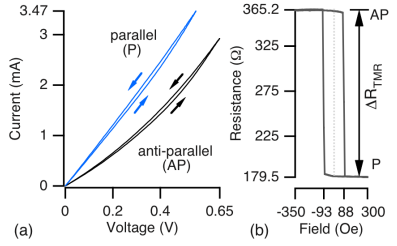

FIG. 1. (Color online) Simultaneous occurrence of resistive and magnetoresistive switching. (a) A slight splitting of the i-v curve can be observed for both magnetic states, which demonstrates the presence of RS. Since the curves are highly symmetric with respect to the origin, only the first quadrant is shown. (b) The magnetoresistive switching of the device characterized by a magnetic minor loop.

[a]Electronic mail: patryk@physik.uni-bielefeld.de.

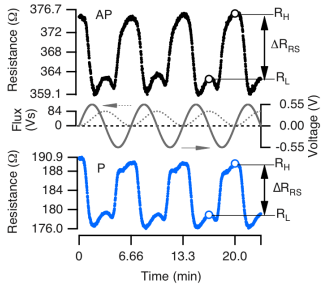

FIG. 2. (Color online) RS induced by a sinusoidal voltage. The resistance of both magnetic states (AP and P) is switched periodically between two resistive states (R_H and R_L). Labels are attached to the resistance curves (at $V=0$) to clarify the definition of R_H and R_L. The inducing voltage (solid) and the corresponding flux (dotted) are shown in the middle of the graph.

primary characteristic of memristive behavior. The variation of the MTJ's resistance, as induced when a sinusoidal voltage is applied, is shown in Fig. 2. The resistance of the AP state is periodically switched between a high resistance (R_H) and a low resistance (R_L) state. A similar RS is observed for the P state. The switching time depends on the magnetic state[21] and can be reduced to 1 s or below by increasing the voltage pulses. The high and low resistance states are defined by the resistance measured at zero voltage, as indicated by the circles in Figs. 2 and 3. Table I summarizes the results obtained from the data presented in Fig. 2. To indicate the reproducible nature of the switching process and discuss the memristive behavior in more detail it is useful to present the resistance data as loops. Figure 3(a) shows the resistance of the P state now as a function of the applied voltage. Starting at R_H the resistance remains stable (nonvolatile) until a critical voltage of about 0.37 V is reached. Here, the resistance drops reaching the lowest value for maximum bias voltage. A slight increase in the resistance can be observed when the applied voltage is released. A similar switching process appears in opposite direction after the polarity of the applied

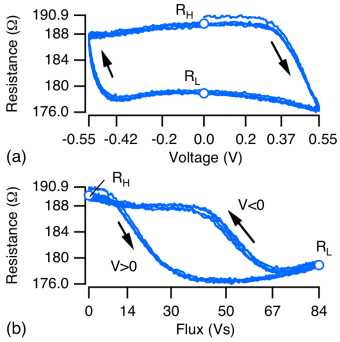

FIG. 3. (Color online) Two complementary methods to display the resistance of the P state as a loop (2.5 loops are plotted on top of each other). (a) The bipolar RS between two stable resistance states becomes clear when plotted vs voltage. (b) The hysteretic nature of RS is shown with clarity when plotted vs flux.

TABLE I. Resistive (RS) and magnetoresistive (TMR) effects calculated from the data in Fig. 2. The index to R is denoting the (magneto)resistive state of the device. ΔR is the total resistance change due to the effect denoted by the index.

	R_H	R_L	ΔR_{RS}	RS
R_{AP}	375.9 Ω	362.5 Ω	13.4 Ω	3.7%
R_P	189.6 Ω	178.9 Ω	10.7 Ω	6.0%
ΔR_{TMR}	186.3 Ω	183.6 Ω		
TMR	98.3%	102.6%		

voltage is changed and, again, when a critical voltage for the switching is reached (−0.42 V). Figure 3(b) shows the hysteretic nature of the resistance as a function of flux Φ. We omit the magnetic flux interpretation of Φ and define its value at a time t after n voltage pulses as $\Phi(t)=\Sigma_{i=0}^{n} v_i t_i$, with v_i and t_i the voltage and duration of the ith pulse, respectively. The flux "applied" to the sample increases when a positive voltage is applied and decreases for negative polarity. For increasing flux the resistance decreases slightly till a flux of about 14 V s is reached and the RS begins. The minimum resistance is reached at about 42 V s before the resistance increases slowly reaching R_L at 84 V s. The backswitching begins at 67 V s leading to a pronounced resistive hysteresis.

As pointed out previously,[21] a possible explanation for the RS of MTJs is a displacement of oxygen vacancies located at the bottom Co–Fe–B/MgO interface. We perform measurements on MTJs with a MgO barrier prepared by postoxidation of a Mg layer to study this model in more detail.[22] The bottom Co–Fe–B electrode is not exposed to oxygen for this preparation method and no oxygen vacancies at the bottom interface are expected.[23] The corresponding measurement is shown in Fig. 4(a). Two features are noted. First, no $R(\Phi)$ hysteresis can be observed indicating the absence of RS, as expected. Second, a V-shaped curve is observed with the resistance lowered by 0.62% in the middle of the flux axis. At this flux the applied voltage reaches its maximum for both polarities. Since the tunneling elements (and the top and bottom conduction lines) are heated due to the high current density the local temperature may not relax during the 200 ms of read-out delay. Therefore, a possible explanation for the reduced resistance is an elevated temperature of the MTJ. A similar influence of remnant heat is visible for the sample showing a distinct RS behavior as denoted by the red lines in Fig. 4(b).

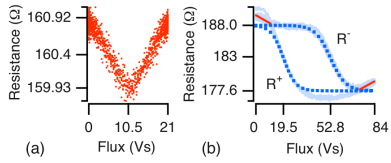

FIG. 4. (Color online) Thermal contribution to the $R(\Phi)$ curve. (a) Reference measurement on a MTJ showing no RS. The amplitude of the applied voltage was 350 mV, 2.5 periods are plotted on top of each other. (b) The fitting curves calculated by Eq. (3) are shown by dotted lines while the experimental data, the same as in Fig. 3(b), is given by the curve in the background. The deviation of the experimental data from the fitting-curve due to thermal contributions is depicted by red solid lines.

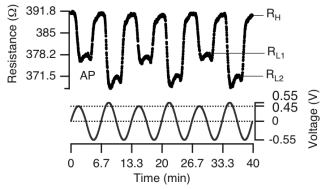

FIG. 5. Influence of an alternating voltage amplitude on the R_L state. The positive amplitude is periodically switched between 450 mV and 550 mV. This leads to a splitting of the low resistance state into R_{L1} and R_{L2} separated by 6.7 Ω.

Now, we stress the question how the presented system differs from a pure memristor. Since the precise microscopic RS mechanism remains elusive, we fit the data by a simple phenomenological function. The hysteresis of $R(\Phi)$ means that a pure memristor can be defined at best "branch-wise,"

$$R^{\pm}(\Phi) = R_H - \frac{\Delta R_{\mathrm{RS}}}{1 + \exp[(\Phi_S^{\pm} - \Phi)/\delta^{\pm}]}, \tag{3}$$

with $R^{+}(\Phi)$ the resistance on the positive branch $(V>0)$, $\Phi_S^{+}=19.5$ V s the inflection point and $\delta^{+}=4.3$ V s indicating the sharpness of the switching process. To fit the negative branch $R^{-}(\Phi)$ we shift the inflection point to $\Phi_S^{-}=52.8$ V s and use $\delta^{-}=5.3$ V s. Both fitting curves are shown in Fig. 4(b). However, a simple hysteresis as presented in Fig. 3 will only result from a sinusoidal voltage of constant amplitude. If the positive amplitude is alternated between two values, as illustrated in Fig. 5, an additional R_L state is generated. In general, multiple resistance states both high and low can be created by according amplitude variation.

In summary, simultaneous magnetoresistive and bipolar RS of MTJs is presented. The entire structure can be understood in the framework of a second order memristive system. Five resistance states are demonstrated for one MTJ proving that the combination of resistive and magnetoresistive switching of MTJs provides a method for multibit data-storage and logic.

The authors gratefully acknowledge Singulus Technologies AG for providing the samples.

[1]S. R. Ovshinsky, Phys. Rev. Lett. **21**, 1450 (1968).
[2]M. Wuttig and N. Yamada, Nature Mater. **6**, 824 (2007).
[3]G. I. Meijer, Science **319**, 1625 (2008).
[4]S. Q. Liu, N. J. Wu, and A. Ignatiev, Appl. Phys. Lett. **76**, 2749 (2000).
[5]A. Beck, J. G. Bednorz, C. Gerber, C. Rossel, and D. Widmer, Appl. Phys. Lett. **77**, 139 (2000).
[6]K. Szot, W. Speier, G. Bihlmayer, and R. Waser, Nature Mater. **5**, 312 (2006).
[7]R. Waser and M. Aono, Nature Mater. **6**, 833 (2007).
[8]J. S. Moodera, L. R. Kinder, T. M. Wong, and R. Meservey, Phys. Rev. Lett. **74**, 3273 (1995).
[9]W. H. Butler, X.-G. Zhang, T. C. Schulthess, and J. M. MacLaren, Phys. Rev. B **63**, 054416 (2001).
[10]C. Chappert, A. Fert, and F. N. van Dau, Nature Mater. **6**, 813 (2007).
[11]L. O. Chua, IEEE Trans. Circuit Theory **18**, 507 (1971).
[12]D. B. Strukov, G. S. Snider, D. R. Stewart, and R. S. Williams, Nature (London) **453**, 80 (2008).
[13]J. J. Yang, M. D. Pickett, X. Li, D. A. A. Ohlberg, D. R. Stewart, and R. S. Williams, Nat. Nanotechnol. **3**, 429 (2008).
[14]D. B. Strukov, J. L. Borghetti, and R. S. Williams, Small **5**, 1058 (2009).
[15]L. O. Chua and S. M. Kang, Proc. IEEE **64**, 209 (1976).
[16]D. Halley, H. Majjad, M. Bowen, N. Najjari, Y. Henry, C. Ulhaq-Bouillet, W. Weber, G. Bertoni, J. Verbeeck, and G. V. Tendeloo, Appl. Phys. Lett. **92**, 212115 (2008).
[17]C. Yoshida, M. Kurasawa, Y. M. Lee, M. Aoki, and Y. Sugiyama, Appl. Phys. Lett. **92**, 113508 (2008).
[18]J. M. Teixeira, J. Ventura, R. Fermento, J. P. Araujo, J. B. Sousa, P. Wisniowski, and P. P. Freitas, J. Phys. D: Appl. Phys. **42**, 105407 (2009); J. Ventura, J. M. Teixeira, J. P. Araujo, J. B. Sousa, P. Wisniowski, and P. P. Freitas, Phys. Rev. B **78**, 024403 (2008).
[19]X. Wang, Y. Chen, H. Xi, H. Li, and D. Dimitrov, IEEE Electron Device Lett. **30**, 294 (2009).
[20]W. F. Brinkman, R. C. Dynes, and J. M. Rowell, J. Appl. Phys. **41**, 1915 (1970).
[21]P. Krzysteczko, X. Kou, K. Rott, A. Thomas, and G. Reiss, J. Magn. Magn. Mater. **321**, 144 (2009).
[22](bottom) Ta 5/Cu–N 90/Ta 5/$Pt_{37}Mn_{63}$ 20/$Co_{70}Fe_{30}$ 2.2/Ru 0.8/$Co_{60}Fe_{20}B_{20}$ 2/MgO 0.8/nativ ox. 1 torr 1200 s/Mg 0.3/$Co_{60}Fe_{20}B_{20}$ 1.5/Ta 10/Cu 30/Ru 7 (top).
[23]H. L. Meyerheim, R. Popescu, N. Jedrecy, M. Vedpathak, M. Sauvage-Simkin, R. Pinchaux, B. Heinrich, and J. Kirschner, Phys. Rev. B **65**, 144433 (2002).